

Engineering Journal



American Institute of Steel Construction

Fourth Quarter 2017 Volume 54, No. 4

- 211 Buckling of Conventional and High-Strength Vanadium Steel Double-Angle Compression Members: Computational Parametric Study
Mark D. Webster, Ahmet Citipitioglu, Ronald L. Mayes, Mohamed M. Talaat and Frank W. Kan
- 243 Buckling of Conventional and High-Strength Vanadium Steel Double-Angle Compression Members: Computational Parametric Evaluation of Slenderness Modification Factors
Mohamed M. Talaat, Ronald L. Mayes, Mark D. Webster, Ahmet Citipitioglu and Frank W. Kan
- 263 The Chevron Effect and Analysis of Chevron Beams—A Paradigm Shift
Patrick J. Fortney and William A. Thornton
- 297 Steel Structures Research Update
Strongback Steel-Braced Frames for Improved Seismic Behavior in Buildings
Judy Liu

Engineering Journal

American Institute of Steel Construction

Dedicated to the development and improvement of structural steel design, fabrication and erection through the interchange of ideas, experiences and data.

Editorial Staff

Editor **Margaret A. Matthew, P.E.**
 Managing Editor **Keith A. Grubb, S.E., P.E.**
 Research Editor **Judy Liu, Ph.D.**

AISC Officers

Chair **David Zalesne**
 Vice Chair **Jack Klimp**
 Secretary/
 General Counsel **David B. Ratterman**
 President **Charles J. Carter, S.E., P.E., Ph.D.**
 Senior Vice President **Scott Melnick**
 Vice President **John Cross, P.E.**
 Vice President **Anne-Marie Eischen**
 Vice President **Lawrence F. Kruth, P.E.**
 Vice President **Tabitha S. Stine, S.E., P.E.**
 Vice President **Mark W. Trimble, P.E.**
 Vice President/
 NSBA Managing Director **Danielle D. Kleinhans, P.E., Ph.D.**

The articles contained herein are not intended to represent official attitudes, recommendations or policies of the Institute. The Institute is not responsible for any statements made or opinions expressed by contributors to this Journal. The opinions of the authors herein do not represent an official position of the Institute, and in every case the officially adopted publications of the Institute will control and supersede any suggestions or modifications contained in any articles herein.

The information presented herein is based on recognized engineering principles and is for general information only. While it is believed to be accurate, this information should not be used or relied upon for any specific application without competent professional examination and verification of its accuracy, suitability and applicability by a licensed engineer or architect. The publication of this information is not a representation or warranty on the part of the American Institute of Steel Construction, its officers, agents, employees or committee members, or any other person named herein, that this information is suitable for any general or particular use, or of freedom from infringement of any patent or patents. All representations or warranties, express or implied, other than as stated above, are specifically disclaimed. Anyone making use of the information presented in this publication assumes all liability arising from such use.

Engineering Journal (ISSN 0013-8029) is published quarterly. Subscriptions: Members: one subscription, \$40 per year, included in dues; Additional Member Subscriptions: \$40 per year. Non-Members U.S.: \$160 per year. Foreign (Canada and Mexico): Members \$80 per year. Non-Members \$160 per year. Published by the American Institute of Steel Construction at 130 E. Randolph Street, Suite 2000, Chicago, IL 60601.

Periodicals postage paid at Chicago, IL and additional mailing offices. **Postmaster:** Send address changes to *Engineering Journal* in care of the American Institute of Steel Construction, 130 E. Randolph Street, Suite 2000, Chicago, IL 60601.

© 2017 by the American Institute of Steel Construction. All rights reserved. No part of this publication may be reproduced without written permission. The AISC logo is a registered trademark of AISC.

UNITED STATES POSTAL SERVICE (All Periodicals Publications Except Requester Publications)

Statement of Ownership, Management, and Circulation

1. Publication Title: **Engineering Journal**

2. Issue Frequency: **Quarterly**

3. Annual Subscription Price: **\$160.00**

4. Complete Mailing Address of Known Office of Publication (Not printer): **130 E. Randolph St., Ste. 2000, Chicago, IL 60601**

5. Complete Mailing Address of Headquarters or General Business Office of Publisher (Not printer): **130 E. Randolph St., Ste. 2000, Chicago, IL 60601**

6. Full Names and Complete Mailing Addresses of Publisher, Editor, and Managing Editor (Do not leave blank):
 Publisher: **Margaret A. Matthew, 130 E. Randolph St., Ste. 2000, Chicago, IL 60601**
 Editor: **Keith A. Grubb, 130 E. Randolph St., Ste. 2000, Chicago, IL 60601**

7. Owner (Do not leave blank. If the publication is owned by a corporation, give the name and address of the corporation immediately followed by the names and addresses of all stockholders owning or holding 1 percent or more of the total amount of stock. If not owned by a corporation, give the names and addresses of the individual owners. If owned by a partnership or other unincorporated firm, give its name and address as well as those of each individual owner. If the publication is published by a partnership or other unincorporated firm, give its name and address.)
 Owner: **American Institute of Steel Construction, 130 E. Randolph St., Ste. 2000, Chicago, IL 60601**

8. Known Bondholders, Mortgagees, and Other Security Holders Owning or Holding 1 Percent or More of Total Amount of Bonds, Mortgages, or Other Securities. If none, check box: None

9. Tax Status (For completion by nonprofit organizations authorized to mail and sell postage stamps at nonprofit rates): Not for profit

10. Publication of Statement of Ownership: If the publication is a general publication, publication of this statement is required. Will be printed in the **October 2017** issue of the publication. Publication not required.

11. Signature and Title of Editor, Publisher, Business Manager, or Owner:  Date: **9/27/17**

12. The State of the completion of this form is required for all publications. I understand that anyone who furnishes false or misleading information on this form or who omits material or information requested on the form may be subject to criminal sanctions (including fines and imprisonment) and civil penalties (including civil penalties).

PS Form 3526, September 2007 (Page 1 of 2) Instructions Page 2/1 PSN 7530-01-000-0001 PRIVACY NOTICE: See our privacy policy on www.usps.com

13. Publication Title	14. Issue Date for Circulation Data Below	
Engineering Journal	July 1, 2017	
15. Extent and Nature of Circulation		
	Average No. Copies Each Issue During Preceding 12 Months	No. Copies of Single Issue Published Nearest to Filing Date
a. Total Number of Copies (Net press run)	1165	1,158
b. Paid Distribution Outside-County Paid Subscriptions (Based on PS Form 3541 (include paid distributor name, rate, address, expiration date, and postage paid))	1020	1,012
c. Paid Distribution In-County Paid Subscriptions (Based on PS Form 3541 (include paid distributor name, rate, address, expiration date, and postage paid))	0	0
d. Paid Distribution by Other Classes of Mail Through the USPS (e.g. First-Class Mail®)	0	0
e. Total Paid Distribution (Sum of 13b, 13c, and 13d)	1020	1,012
f. Free or Nominal Rate Outside-County Copies (Included on PS Form 3541)	0	0
g. Free or Nominal Rate In-County Copies (Included on PS Form 3541)	0	0
h. Free or Nominal Rate Copies (Included in Other Classes Through the USPS (e.g. First-Class Mail®))	0	0
i. Free or Nominal Rate Distribution Outside the Mail (Carriers or other means)	105	107
j. Total Free or Nominal Rate Distribution (Sum of 13f, 13g, 13h, and 13i)	105	107
k. Total Distribution (Sum of 13e and 13j)	1125	1,119
l. Copies not Distributed (Net Intentional to Publishers (Net Intentional))	41	39
m. Total (Sum of 13k and 13l)	1085	1158
n. Percent Paid (PS Form 3541, line 13b)	95%	90%

Submissions: Manuscripts are welcomed, but publication cannot be guaranteed. Authors do not receive remuneration. Guidelines for authors are printed on the inside back cover and available online at www.aisc.org/ej.

Subscriptions: subscriptions@aisc.org, 312.670.2400

Archives: Search at www.aisc.org/ej. Article downloads are free for current members and are available for a nominal fee for non-members.

Buckling of Conventional and High-Strength Vanadium Steel Double-Angle Compression Members: Computational Parametric Study

MARK D. WEBSTER, AHMET CITIPITIOGLU, RONALD L. MAYES,
MOHAMED M. TALAAT and FRANK W. KAN

ABSTRACT

High-strength, low-alloy vanadium (HSLA-V) steel offers higher strength and toughness than conventional steel. The resulting lighter weight and more slender structural components are more susceptible to buckling in compression. A series of conventional Grade 50 steel and HSLA-V (nominal Grade 80) steel angle compression components was tested at Lehigh University's ATLSS laboratory. This experimental database was used to develop and verify a modeling approach using the general-purpose finite element (FE) software ABAQUS to simulate the component buckling response.

This study extensively evaluates the 2010 American Institute of Steel Construction (AISC) and Steel Joist Institute (SJI) design equations for double-angle buckling, resulting in significant findings and recommendations for both specifications. The primary objective of this paper was to assess the validity of applying the buckling equations given in the SJI 2010 Design Specification for long-span and deep-long-span joists (SJI, 2010) to double-angle compression members manufactured using 80-ksi HSLA-V steel. Present SJI specifications are applicable only for steel with specified yield stress of 50 ksi or less. Another objective of this study was to compare the design equations for compression buckling in the SJI Design Specification and the AISC 2010 *Specification* (AISC, 2010) and to develop recommendations for enhancing the accuracy of buckling equations commonly used in current practice. To achieve these goals, an extensive database of analytical buckling simulations was created to compare the performance of the code buckling equations in determining the buckling strength for regular and HSLA-V steel compression members.

Potential solutions for resolving the observed lack of conservatism in the strong-axis buckling predictions were investigated. The use of the modified component slenderness ratio in the AISC provisions significantly improved the accuracy of the SJI buckling strength predictions for strong-axis buckling cases with Q -factor values less than 1.0.

Keywords: high-strength vanadium steel, compression, computational parametric study, modification factors, buckling analysis.

INTRODUCTION

A long-term research project sponsored by the Army Research Laboratory (ARL) under Cooperative Agreement DAAD 19-03-2-0036 and executed by the Advanced Technology Institute (ATI) was initiated in 2003 to assess the impact of high-strength, low-alloy microalloyed vanadium

(HSLA-V) steels on a wide variety of different applications. HSLA-V steels have specified yield strengths as high as 90 ksi and thus provide the opportunity both for weight reduction and enhanced sustainability.

This paper presents results from a computational correlation and parametric study the authors performed on double-angle compression components (SGH, 2011, 2012). A previous correlation study describes the successful use of nonlinear analytical modeling to closely match failure modes and strengths observed in 20 compression tests of double-angle members with a range of properties (SGH, 2011). Based on the success of the correlation study, the parametric study was performed to extend our findings beyond the range of parameters included in the experimental test program.

The primary objective of this parametric study is to assess the validity of applying the buckling equations given in the 2010 Steel Joist Institute (SJI) Design Specification for long-span and deep-long-span joists (SJI, 2010) to double-angle compression members manufactured using 80-ksi HSLA-V steel. Present SJI specifications are applicable only for

Mark D. Webster, Senior Structural Engineer, Simpson Gumpertz & Heger Inc., Waltham, MA. Email: MDWebster@sgh.com (corresponding)

Ahmet Citipitiglu, Director of Engineering and Design, TAV Construction, Istanbul, Turkey. Email: Ahmet.Citipitiglu@tav.aero

Ronald L. Mayes, Staff Consultant, Simpson Gumpertz & Heger Inc., San Francisco. Email: RLMayes@sgh.com

Mohamed M. Talaat, Adjunct Assistant Professor, Cairo University, Egypt and Senior Structural Engineer, Simpson Gumpertz & Heger Inc., Newport Beach, CA. Email: MTalaat@sgh.com

Frank W. Kan, Principal, Simpson Gumpertz & Heger Inc., Waltham, MA. Email: FWKan@sgh.com

steel with specified yield stress of 50 ksi or less. The 2010 SJI Specification is based on the 2010 AISC *Specification* (AISC, 2010) but omits flexural-torsional buckling and the application of the slenderness modification ratio for built-up members, both of which are included in the AISC *Specification*. Another objective of this study is, therefore, to assess whether these particular AISC provisions are applicable to the design of double-angle compression members in general.

SJI long-span joists typically have double-angle top and bottom chords and single- or double-angle web members. SJI classifies steel joists into several design categories, each with its own specification. The long-span LH and DLH series share the same specification. LH-series joists commonly range in span from 25 to 95 feet, while the DLH-series can reach lengths of more than 140 feet. These joists are used for both floor and roof applications and typically support steel deck with or without concrete topping.

This paper describes the establishment of an extensive database of analytical buckling simulations covering a wide range of section parameters to compare the performance of the code buckling equations in determining the buckling strength for regular and HSLA-V steel compression members.

DESIGN FOR BUCKLING

The estimation of the critical buckling load depends on the mode and type of buckling (i.e., elastic or inelastic). The critical buckling load is computed for several possible buckling modes depending on the compression member profile. The lowest critical load for the associated buckling mode is assumed to represent the governing buckling phenomenon. The 2010 SJI Specification mostly follows the 2010 AISC *Specification* but makes some important modifications, which we discuss in this section.

Flexural Buckling

The classical buckling equation defining elastic flexural buckling, also known as Euler buckling, is used to determine the critical stress after which instability in the compression member occurs, causing it to lose its strength. This relationship, given here, is valid for slender members:

$$F_{e,i} = \frac{\pi^2 E}{(KL/r)_i^2} \quad (1)$$

where F_e is the theoretical elastic buckling stress, E is the material's Young's modulus of elasticity, L is the length of the compression member, and r is the radius of gyration of the cross-section. Subscript i refers to the two buckling axes: strong and weak axis.

A particular focus in the development of buckling equations has been the transition curve between elastic buckling and full-section yielding, which accounts for the effects of

residual stresses and imperfections. Figure 1 illustrates a comparison from published literature (Salmon and Johnson, 1990) between experimental tests and critical load estimates using the AISC equations for flexural buckling of I-shape columns. The figure suggests that a larger spread of experimental results from the analytical prediction takes place at lower slenderness ratios, where inelastic buckling dominates.

The critical stress for flexural buckling given in both the SJI and AISC specifications is as follows:

$$F_{cr} = \begin{cases} \left(0.658 \frac{QF_y}{F_{e,i}}\right) QF_y & (KL/r)_i \leq 4.71 \sqrt{\frac{E}{QF_y}}, \frac{QF_y}{F_e} \leq 2.25 \\ 0.877 F_{e,i} & (KL/r)_i > 4.71 \sqrt{\frac{E}{QF_y}}, \frac{QF_y}{F_e} > 2.25 \end{cases} \quad (2)$$

where F_{cr} is the critical buckling stress, Q is the slenderness reduction factor for unstiffened elements, and $KL/r = 4.71 \sqrt{E/QF_y}$ is the demarcating slenderness ratio between elastic and inelastic buckling.

Equation 2 lists as equivalent alternatives a condition on the slenderness ratio KL/r and another condition on the critical elastic stress $QF_y/F_e = 2.25$. On closer examination, the equivalence of both limits only holds unconditionally for purely flexural buckling.

The flexural buckling equation is applied about both profile axes, and the lower critical buckling stress governs.

Modified Flexural Buckling for Built-Up Sections

The slenderness term may be modified if the buckling mode of a compression member built up from two or more shapes interconnected by bolted or welded elements is subject to relative displacement due to shear forces in the connectors between the individual shapes forming the member. For double angles with welded spacers, the AISC *Specification* modifies the slenderness ratio as follows:

$$\text{For } \frac{a}{r_i} \leq 40 \quad (KL/r)_{y,m} = (KL/r)_o \quad (3)$$

$$\text{For } \frac{a}{r_i} > 40 \quad (KL/r)_{y,m} = \sqrt{(KL/r)_o^2 + (K_i a/r_i)^2} \quad (4)$$

where $(KL/r)_{y,m}$ is the modified slenderness ratio of the built-up member, $(KL/r)_o$ is the slenderness ratio of the built-up member acting as a unit, $K_i = 0.50$ for back-to-back angles, a is the connector spacing along the length of the member, and r_i is the minimum radius of gyration of an individual component.

This modification addresses the ability of the built-up section to act compositely in the direction(s) where the radius of gyration of a single element is significantly less than the composite value (Aslani and Goel, 1991). In the case of double-angle compression members, this modification applies only to strong-axis buckling because there is no spacer influence in the weak-axis buckling case.

Flexural-Torsional Buckling

The critical flexural-torsional buckling stress, $F_{cr,ft}$, for singly symmetric compression members—for example, double angles—without slender elements is given in the 2010 AISC *Specification* as follows. This relationship is valid for members with both compact and noncompact sections.

$$F_{cr,ft} = \frac{F_{cr,y} + F_{cr,z}}{2H} \left(1 - \sqrt{1 - \frac{4HF_{cr,y}F_{cr,z}}{(F_{cr,y} + F_{cr,z})^2}} \right) \quad (5)$$

Slender leg elements are defined as those with width-to-thickness ratio, $b/t < 0.45\sqrt{E/F_y}$. For double angles, the relationship for this mixed-mode buckling in Equation 5 combines the strong axis flexural buckling stress, $F_{cr,y}$, given in Equation 2 and the pure torsional buckling stress, $F_{cr,z}$, given in Equation 6. The other terms used in Equation 5 are defined as follows:

$$F_{cr,z} = \frac{JG}{Ar_o^2} \quad (6)$$

$$H = 1 - \frac{x_o^2 + y_o^2}{r_o^2} \quad (7)$$

$$J = At^3/3 \quad (8)$$

where J is the torsional moment of inertia, A is the double-angle area, t is the angle leg thickness, G is the shear modulus of elasticity, r_o is the polar radius of gyration about the double-angle section's shear center, and x_o and y_o are the distances from the composite centroid to the angle shear center.

For double-angle members with slender elements, Equation 5 does not apply. Instead, Equation 2 is used where subscript i is ft , and the following modification:

$$F_{e,ft} = \frac{F_{e,y} + F_{e,z}}{2H} \left(1 - \sqrt{1 - \frac{4HF_{e,y}F_{e,z}}{(F_{e,y} + F_{e,z})^2}} \right) \quad (9)$$

with $F_{e,z} = F_{cr,z}$ according to Equation 6 and $F_{e,y}$ according to Equation 1.

Single-Angle Buckling

Flexural buckling about the angle minor principal axis, r_z , of the individual angles forming a double-angle compression

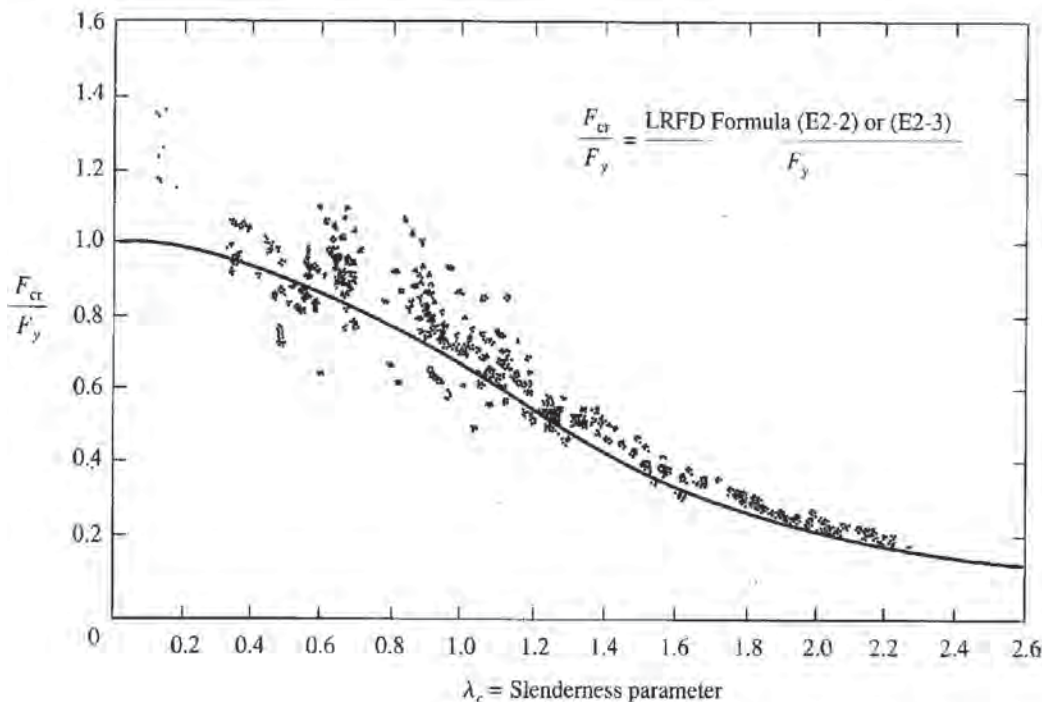


Fig. 1. Comparison of I-beam compression tests with AISC flexural buckling equations (Salmon and Johnson, 1990).

member is checked using Equation 2. Using a K factor of 1.0 implying pin-pin boundary conditions is conservative; a lower value is more realistic. This check must be performed when using both the AISC and SJI specifications.

Difference between AISC and SJI Specification Buckling Calculations

The 2010 SJI Specification considers only the flexural buckling modes of the individual angle components and the overall double-angle section, including the element slenderness reduction factor Q , which accounts for local buckling. The component slenderness modification for built-up sections and the flexural-torsional buckling mode that are a part of the AISC requirements are not considered in the SJI Specification. These additional checks in the AISC Specification result in more conservative design strengths, especially for double angles with low slenderness ratios (KL/r), which are common in the chord members of open web joists.

The difference among the various strong-axis buckling load strengths plotted against varying slenderness ratios for a given double-angle section geometry is shown in Figure 2. These curves are calculated for the member end conditions pinned about the strong axis and fixed about the weak axis and the two angles connected by a single spacer element. The following buckling modes are calculated:

- Sum of the buckling strength of the individual single angles between spacers, $P_{cr-flex z}$.
- Global double-angle flexural buckling about both weak and strong axis, $P_{cr-flex x}$ and $P_{cr-flex y}$.
- Flexural-torsional buckling, $P_{cr-flex tor}$.

- Flexural buckling with the modified member slenderness ratio which accounts for the influence of the connector between the angles per the AISC Specification, $P_{cr-flex y mod}$.

The solid red line represents the AISC lower-bound nominal strength envelope bounding all five buckling modes. Among these buckling strength curves, the dashed green line represents the strong-axis flexural buckling mode constituting the lower bound of modes considered by the SJI Specification.

PAST RESEARCH

While the behavior of single-angle compression members has been studied extensively (Kennedy and Murty, 1982; Chuenmei, 1984; Elgaaly et al., 1991; Elgaaly et al., 1992; Galambos, 1991; Popovic et al., 1999), there is less research in the literature related to double-angle compression members.

Kennedy and Murty (1972) performed compression tests of single-angle, double-angle, and tee members. The tests included six sets of three equal-leg double-angle tests with pinned ends and six sets of three double-angle tests with fixed ends. The Q factors for these tests, calculated using the current AISC Specification, ranged from 0.58 to 0.92, and the slenderness ratios from 22 to 90. The research found that for members with low slenderness ratios flexural-torsional buckling equations produced better results than the flexural buckling equations.

Kitipornchai and Lee (1986) performed compression tests of single-angle, double-angle, and tee pin-ended members. The tests included six sets of two equal-leg double-angle

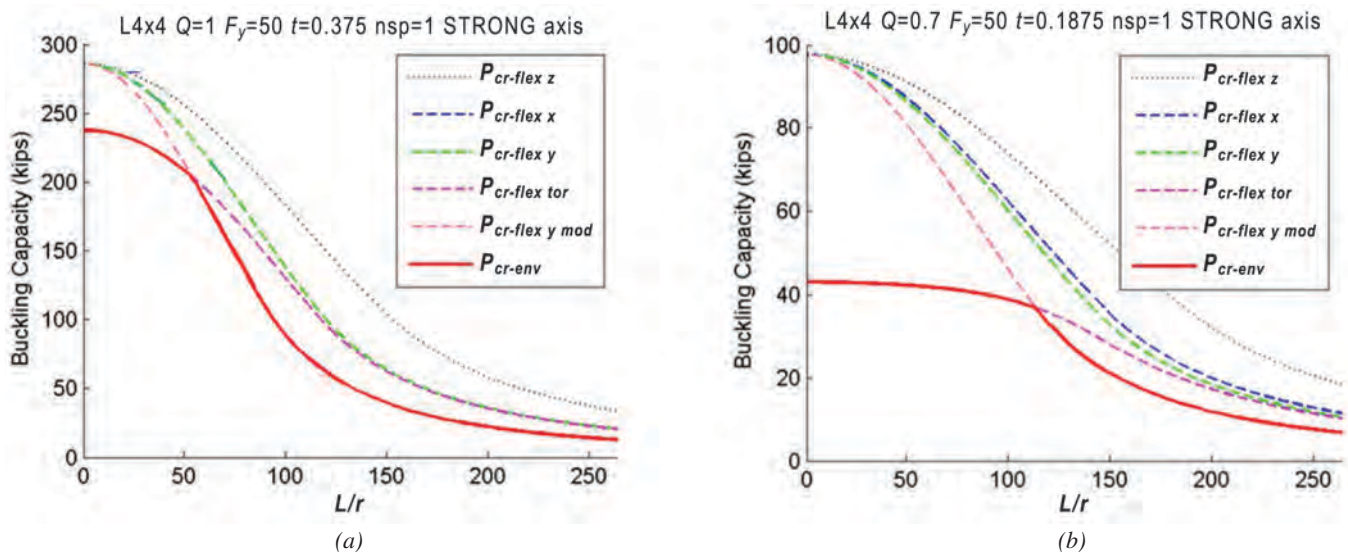


Fig. 2. Example AISC and SJI nominal buckling strength curves of different buckling modes for double-angle compression members: (a) 2L4x4x3/8 - $Q = 1$; (b) 2L4x4x3/16 - $Q = 0.7$.

Table 1. Variable Matrix of the Double-Angle Compression Member Parametric Study

Size	L/r (based on weak axis)	F _y , ksi	Thickness t, in.			Spacers	Imperfection Magnitude	End Conditions	Residual Stress, ksi	Total Cases
			Q = 1	Q = 0.85	Q = 0.7					
2L8×8	20, 40, 80, 160	50	3/4	1/2	—	1, 2 bars	L/500, L/1500	Weak, strong	0	192
		65	7/8	9/16	—					
		80	15/16	5/8	—					
2L6×6	20, 40, 60, 80, 100, 160	50	9/16	3/8	—	1, 2 bars	L/500, L/1500	Weak, strong	0	288
		65	11/16	7/16	—					
		80	3/4	1/2	—					
2L4×4	50, 70, 90, 130, 150, 240	50	3/8	1/4	3/16	1, 2 angles	L/500, L/1500	Weak, strong	0	432
		65	7/16	9/32	7/32					
		80	15/32	5/16	1/4					
2L2×2	50, 70, 90, 130, 150, 240	50	3/16	1/8	3/32	1, 2 angles	L/500, L/1500	Weak, strong	0, 11	864
		65	7/32	5/32	1/8					
		80	1/4	5/32	1/8					

tests. The Q factors varied from 0.71 to 0.87 and the slenderness ratios from 53 to 75. This research found good agreement with the 1978 AISC ASD *Specification* (AISC, 1978), which did not include equations for flexural-torsional buckling.

Galambos (1991) proposed simplifying the 1986 AISC equations and replacing the Q factor with effective leg widths to address local buckling. He reported good results using test data from previous studies.

PARAMETERS ASSESSED

This parametric study consisted of a large number of analytical buckling simulations of double-angle specimens with

50, 65, and 80 ksi nominal yield strengths. The angle sizes included were LL8×8, LL6×6, LL4×4, and LL2×2. Table 1 lists the geometric variables used for each of the nominal yield strengths and angle sizes. A total of 3552 cases were analyzed. These cases included multiple simulations for each member size using initial geometric imperfection shapes generated by linear super-position of elastic mode shapes generated with both fixed-fixed and pinned-pinned boundary conditions at each end. For each specimen, the lower buckling strength result was reported, resulting in a database of 1776 buckling strengths. Figure 3 shows the axis definitions.

For each yield strength and angle size combination, the leg thicknesses of the angles were selected to approximate

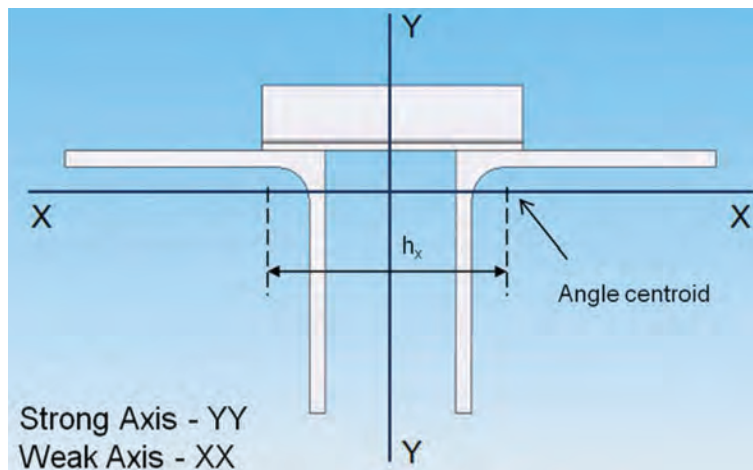


Fig. 3. Definition of local axes in double-angle member cross-sections.

the assigned element slenderness, Q , in the matrix. For the larger double-angle sizes, thicknesses were selected to produce Q factors of 1.0 and 0.85, while for the smaller angles, Q factors of 0.7, 0.85 and 1.0 were selected. Q factors for angles are defined per the AISC *Specification* (Figure 4).

The effect of spacer type and spacing between the double angles was evaluated. The large double-angle members (i.e., LL8×8 and LL6×6) were modeled assuming that bar spacers are used with a 1-in. gap between the angles. This corresponds to the typical use of these sizes as chord members within a girder assembly. The smaller double-angle members (i.e., LL4×4 and LL2×2) were modeled assuming that angle spacers are used with a larger gap of 2 in. between the angles. This corresponds to the typical use of these sizes as web members connected to the chord member legs in girders as shown in Figure 5. The spacers were located either at the midpoint between the ends of the double angles or at the third-points (one or two spacers, respectively). Bar spacers were welded 1-in.-diameter round bars located between the back-to-back angle legs. Angle spacers were angles welded to the outstanding legs of the double angles. Figure 5 shows a typical angle spacer.

The geometrical imperfections were modeled by using superimposed buckling modeshapes and scaling the maximum out-of-straightness to the target magnitude value (either $L/500$ or $L/1500$). This procedure is more completely described in a separate study by the authors (SGH, 2011). The imperfection magnitude of $L/1500$ is the basis of design code buckling equations. Cases with geometric imperfection magnitudes of $L/500$ were included to understand the effect of larger imperfections.

For each analysis model, two sets of boundary conditions were imposed. The first set corresponded to weak-axis flexural buckling, while the second set corresponded to strong-axis flexural buckling. For the first set, the rotations about the strong axis were restrained and rotation about the

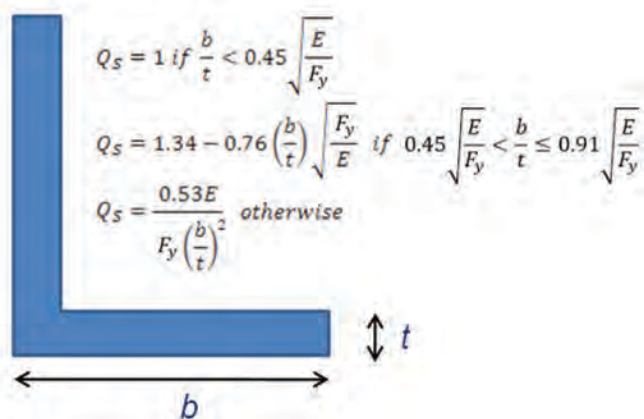


Fig. 4. Angle local element slenderness ratio.

weak axis was permitted at the top and bottom ends of the specimen. Opposite restraints were used for the second set, enforcing a strong-axis buckling condition. Torsional rotation was restrained at both ends in all cases. Figure 6 illustrates the weak- and strong-axis set-ups.

A previous study by the authors (SGH, 2011) found that the sensitivity of the simulated buckling strength to residual stresses is minor except in small cross-sections (LL1.75×1.75× $\frac{1}{8}$), where residual stresses decreased the buckling strength by up to 10%. In larger cross-sections (LL3×3× $\frac{3}{16}$ and LL3.5×3.5× $\frac{3}{8}$), the modeling of residual stresses affected the buckling load by less than 5%. For the present study, only the LL2×2 series specimens were analyzed with and without residual stresses, and the lower buckling strength was used.

MODELING APPROACH

Double-Angle Modeling Steps

The generation of the set of parametric models was automated using customized scripts and the mesh generation program Truegrid (XYZ Scientific Applications, n.d.). The buckling analyses of the double angles were carried out using the general-purpose, nonlinear, finite element (FE)

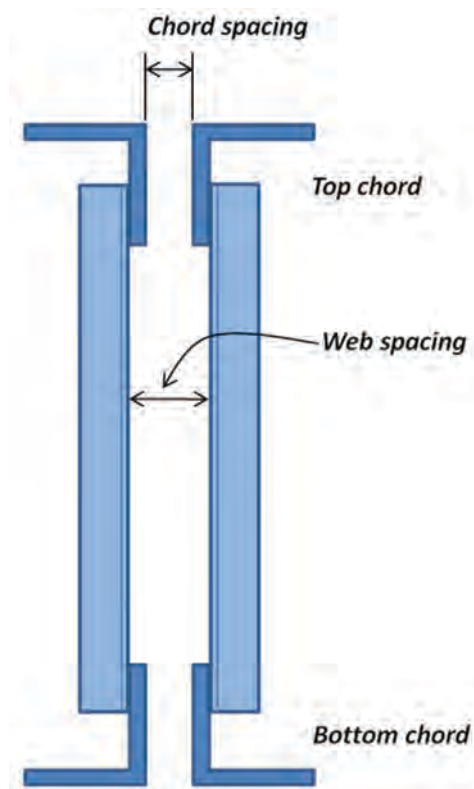


Fig. 5. Double-angle spacing definition for typical joist configuration.

software ABAQUS (2007). ABAQUS has extensive capabilities for modeling continuum mechanics, including contact, and for solving elastic buckling as well as unstable post-buckling problems. The nonlinear buckling analyses were solved using the Modified Riks algorithm, which is available in ABAQUS for loading regimes with geometrically unstable phases.

The modeling process included the following steps:

- Angles and angle spacers were modeled using four-node shell elements; eight-node continuum elements were used to model the bar spacers. A cross-section of a model is shown in Figure 7.
- To ensure conservative buckling strengths for the LL2×2 and LL4×4 double-angle members, L1×1×1/8 spacer angles were used, which are on the lighter side of standard industry practice. For the LL6×6 and LL8×8 members, 4-in.- and 5-in.-long bar spacers were used, respectively. The configurations of the spacers are shown in Figure 8.
- The material properties are shown in Figure 9.
- For LL2×2 angles, an alternate series of models were analyzed that included the effect of residual stresses. The residual stresses were imposed at the angle legs in the longitudinal direction prior to loading and allowed to equilibrate. The residual stress distribution profile across each angle leg cross-section is shown in Figure 10. A maximum residual stress magnitude of 10.8 ksi was imposed.

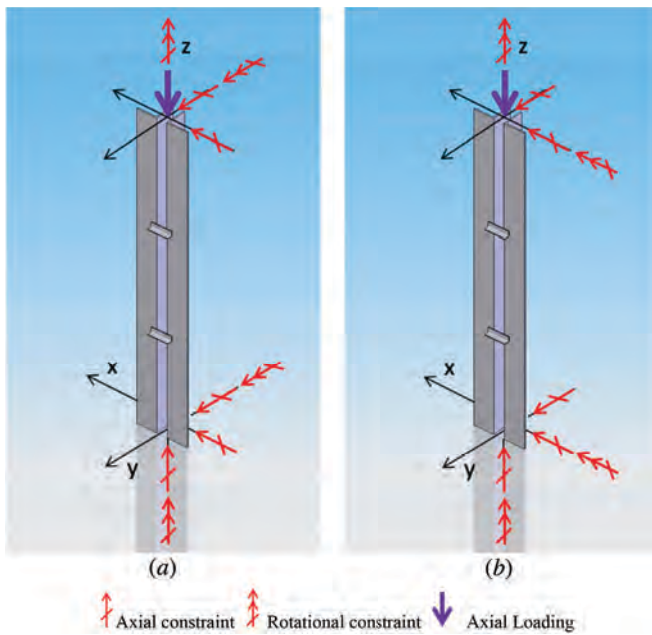


Fig. 6. Double-angle model boundary conditions for weak and strong axis buckling analyses: (a) weak-axis pinned; (b) strong-axis pinned.

- Buckling mode shapes of each specimen were determined using an elastic eigenvalue analysis for each perfect geometry model. The analyses yielded the critical loads and mode shapes for a large number of buckling modes. Initial geometric imperfections were introduced by combining a number of buckling mode shapes that fall within a given multiple of the fundamental elastic load.

ANALYSIS RESULTS

Table 2 summarizes the ratios of analysis results to the predictions of the SJI Specification for the different parameter study variables. Figures 11 through 14 show typical graphical comparisons of the analytical results to the SJI Specification. The weak-axis buckling strengths are well-predicted by the flexural buckling curve in the SJI Specification (Figures 11 and 13), while the SJI Specification overpredicts the strong-axis buckling strength (Figures 12 and 14).

Figure 15 summarizes these results for the LL4×4 analyses, sorted by Q factor and the number of spacers. For small slenderness ratios, the strong-axis results are closer to the SJI predictions, but the SJI Specification becomes increasingly nonconservative with increasing slenderness ratios.

Table 3 and Figure 16 illustrate a key finding: Across all investigated parameters, the SJI Specification predicts the buckling strength of high-strength vanadium steel (80 ksi) and conventional steel (50 ksi) equally well. The table indicates $(P_{fe}/P_{nSJI})_{Fy}/(P_{fe}/P_{nSJI})_{50}$, where:

$(P_{fe}/P_{nSJI})_{Fy}$ = ratio of the analytical buckling strength to the strength predicted by the SJI Specification for steel with a yield stress of F_y

$(P_{fe}/P_{nSJI})_{50}$ = ratio of the analytical buckling strength to the strength predicted by the SJI Specification for steel with a yield stress of 50 ksi

The graphs provide a similar metric using the ratios of analytical to predicted buckling stress for 80-ksi and 50-ksi steel. Values of unity indicate that the equations predict the buckling strength (or stress) equally well for both yield stresses.

There is no discernible bias in these current buckling equations when used with grades representative of HSLA-V material. The overall mean value of the ratio of the ratios from Table 3 is 1.00 and 1.01 for imperfection ratios of $L/1500$ and $L/500$, respectively. This result clearly demonstrates that the overall margin of safety for the higher yield strength HSLA-V steels is the same as 50-ksi steel when considering all of the variables included in this study.

The results for weak-axis buckling show that the SJI buckling equations are adequate and appropriately conservative for almost all cases included in this study. The results for strong-axis buckling, however, show that the SJI buckling equations are nonconservative for many cases, and the

Table 2. Global Comparison of Analysis versus SJI Specification Buckling Strength Ratio

Global Average of P_{fe}/P_{n_SJI}							
Axis	Variable	L/1500			L/500		
		50 ksi	65 ksi	80 ksi	50 ksi	65 ksi	80 ksi
	Q Factor						
Strong	0.7	0.855	0.890	0.868	0.782	0.808	0.787
	0.85	1.033	1.034	1.021	0.900	0.916	0.917
	1	1.019	1.011	1.004	0.928	0.930	0.929
Weak	0.7	1.045	1.104	1.095	0.945	1.016	1.021
	0.85	1.186	1.172	1.160	1.066	1.083	1.080
	1	1.136	1.126	1.116	1.062	1.060	1.055
	Number of Spacers						
Strong	1	0.973	0.973	0.958	0.872	0.878	0.873
	2	1.005	1.015	1.005	0.899	0.918	0.915
Weak	1	1.124	1.127	1.116	1.030	1.050	1.043
	2	1.148	1.151	1.142	1.047	1.069	1.072

Mean: Strong	0.989	0.994	0.982	0.886	0.898	0.894
Mean: Weak	1.136	1.139	1.129	1.038	1.060	1.058
Mean: Weak and strong	1.063	1.067	1.055	0.962	0.979	0.976
Grand total	1.061			0.972		

nonconservatism increases as the Q factor decreases from 1.0 to 0.7. This nonconservatism occurs regardless of material yield stress.

To address the nonconservatism in the SJI strong-axis buckling results, the following possible modifications to the SJI Specification were investigated:

- Full adoption of the AISC *Specification* equations.
- Adoption of the AISC component slenderness (KL/r) modification equation only.
- Adoption of a revised Q factor calculation.

This paper addresses the first two options. A separate paper by the authors (Talaat et al., 2017) evaluates proposed changes to the Q factor calculation that would address the nonconservatism associated with low Q factors. It is shown that using the Q factor formulation from the 1968 AISI Specification, which accounts for twisting of the angle cross section when both legs buckle locally in the same direction, eliminates the Q factor nonconservatism seen in the results.

PROPOSED MODIFICATIONS TO THE 2010 SJI BUCKLING DESIGN EQUATIONS

A number of potential solutions for resolving the lack of conservatism in the SJI Specification's strong-axis strength predictions were investigated. Two options are addressed in this paper:

1. The adoption by SJI of all of the AISC provisions, including both the torsional flexural buckling and the slenderness modification ratio used for built-up compression members.
2. The adoption by SJI of the AISC slenderness modification ratio used for built-up compression members but not the AISC flexural-torsional provisions.

Use of All AISC Buckling Provisions

In addition to the flexural buckling modes considered by the SJI Specification, the AISC *Specification* considers the flexural-torsional buckling failure mode and modification of the slenderness ratio (KL/r) for built-up members. In the case of double angles, this modification applies only to the strong-axis buckling where the spacers affect the deformation of the overall section.

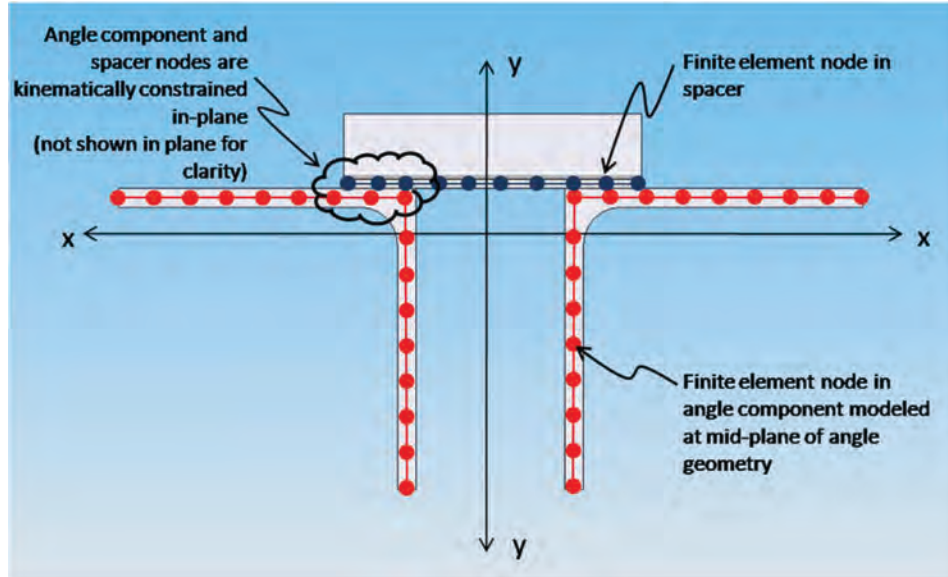


Fig. 7. Double-angle cross-section modeling scheme and constraint between angle and spacer nodes.

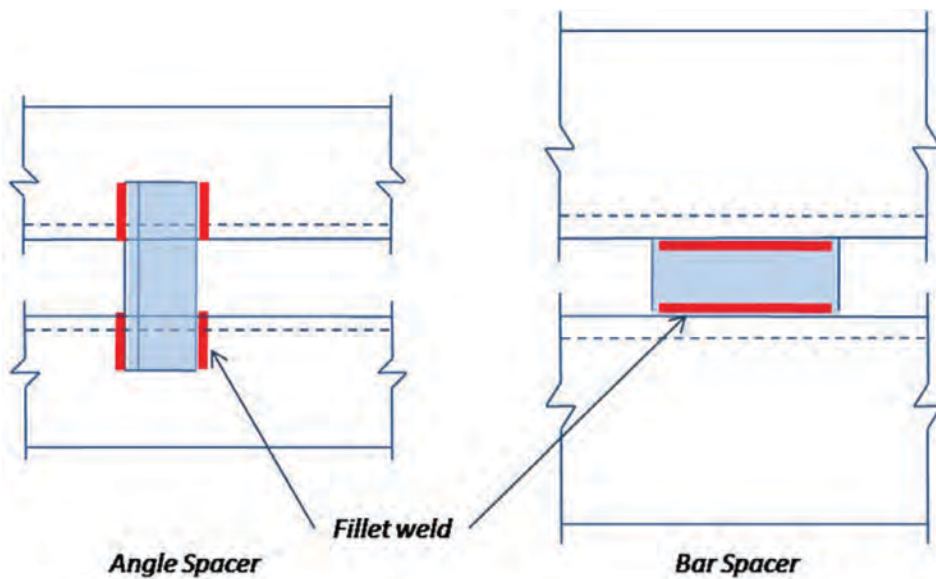


Fig. 8. Double-angle bar spacers (chord members) and angle spacers (web).

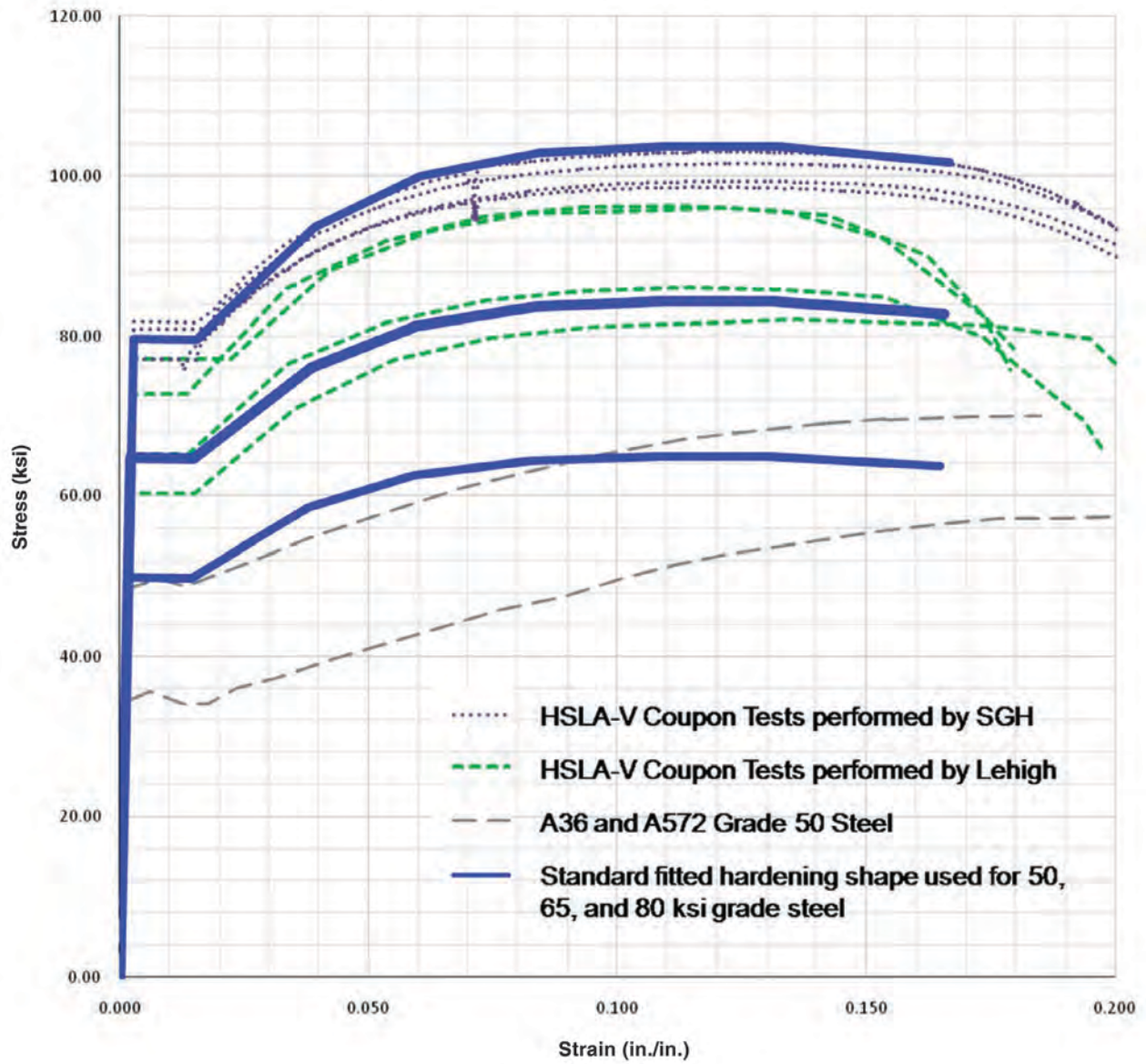


Fig. 9. Fitted hardening shapes compared to coupon tests or ASTM standard response for 50-, 65- and 80-ksi materials [ASTM A36/A 36M-08 (2008) and A 572/A 572M-07 (2007)].

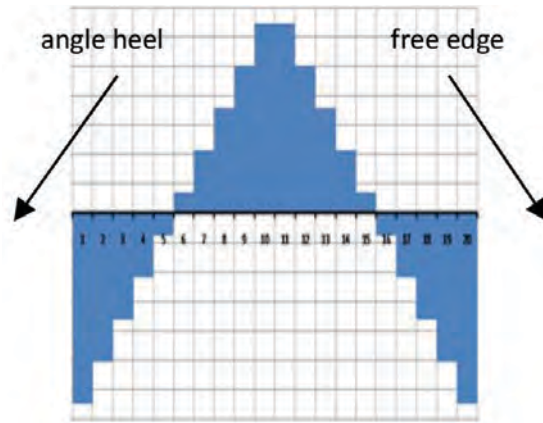


Fig. 10. Residual stress profile discretization across the angle leg.

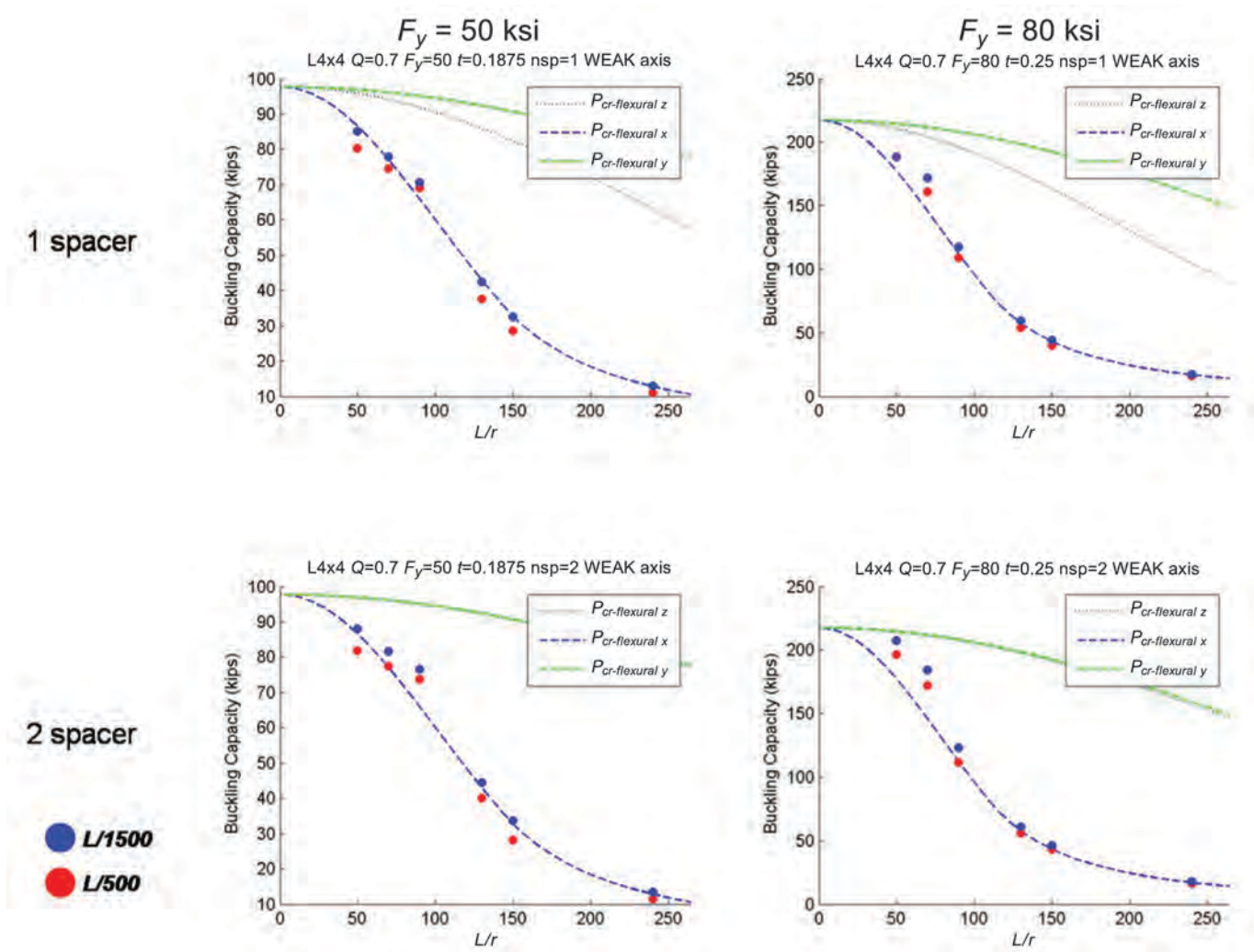
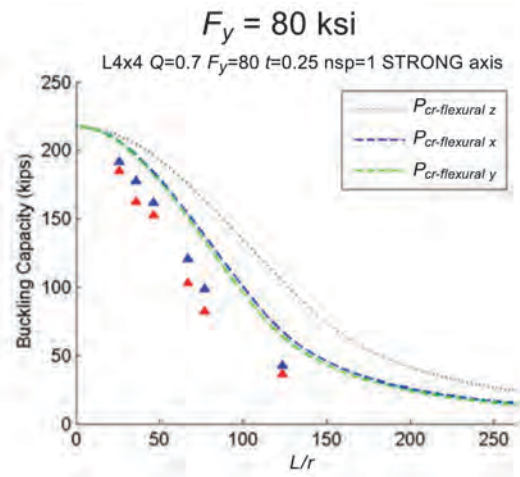
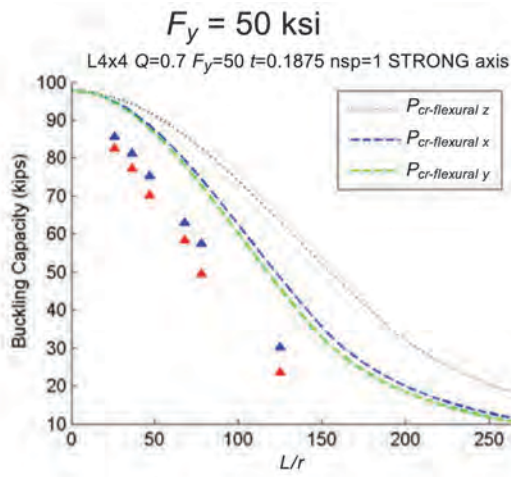


Fig. 11. LL4x4 analytical weak-axis (pinned) buckling strengths compared to the SJI Specification equations; L/500 and L/1500 imperfection magnitudes; $F_y = 50$ -ksi and 80-ksi materials; $Q = 0.7$.

1 spacer



2 spacer

▲ L/1500
▲ L/500

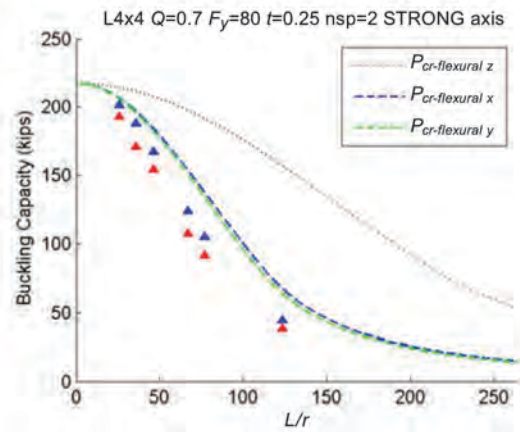
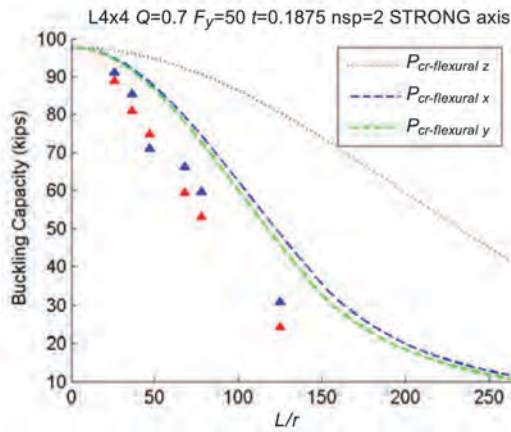
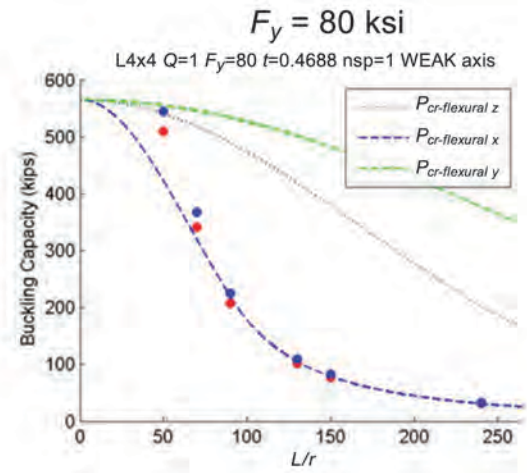
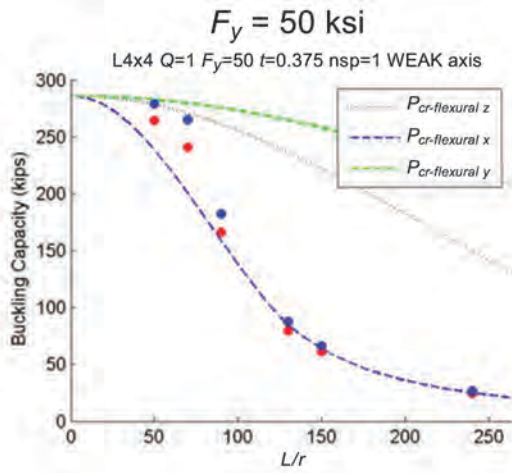
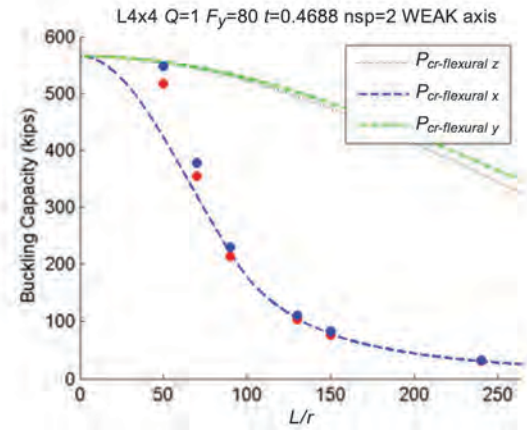
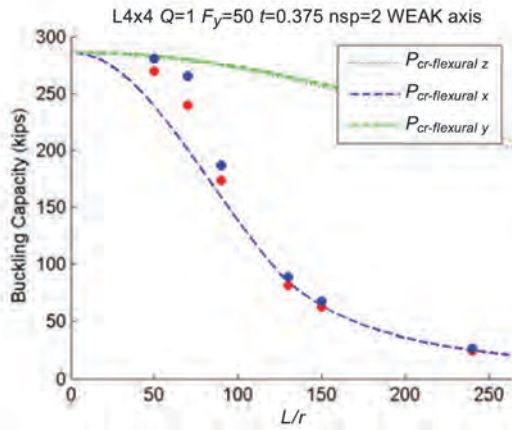


Fig. 12. L4x4 analytical strong-axis (pinned) buckling strengths compared to the SJI Specification equations; L/500 and L/1500 imperfection magnitudes; $F_y = 50$ -ksi and 80-ksi materials; $Q = 0.7$.

1 spacer



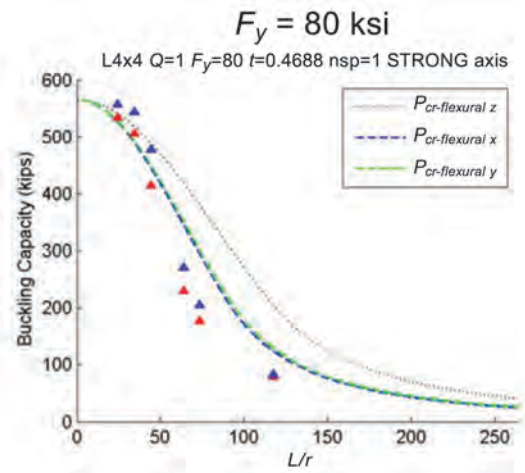
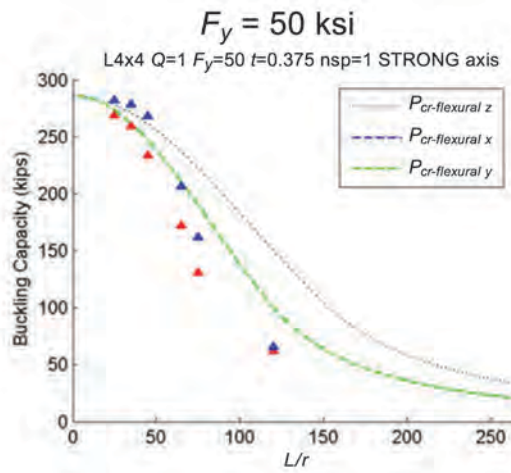
2 spacer



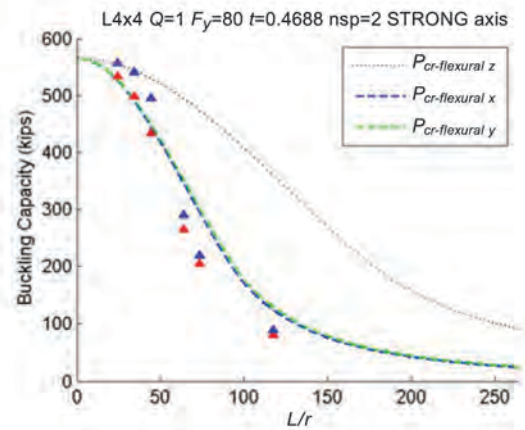
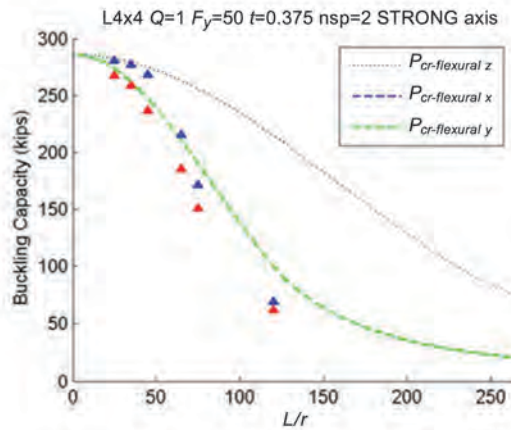
● L/1500
● L/500

Fig. 13. LL4x4 analytical weak-axis (pinned) buckling strengths compared to the SJI Specification equations; L/500 and L/1500 imperfection magnitudes; $F_y = 50$ -ksi and 80-ksi materials; $Q = 1.0$.

1 spacer



2 spacer



▲ $L/1500$
▲ $L/500$

Fig. 14. L4x4 analytical strong-axis (pinned) buckling strengths compared to the SJI Specification equations; $L/500$ and $L/1500$ imperfection magnitudes; $F_y = 50$ -ksi and 80-ksi materials; $Q = 1.0$.

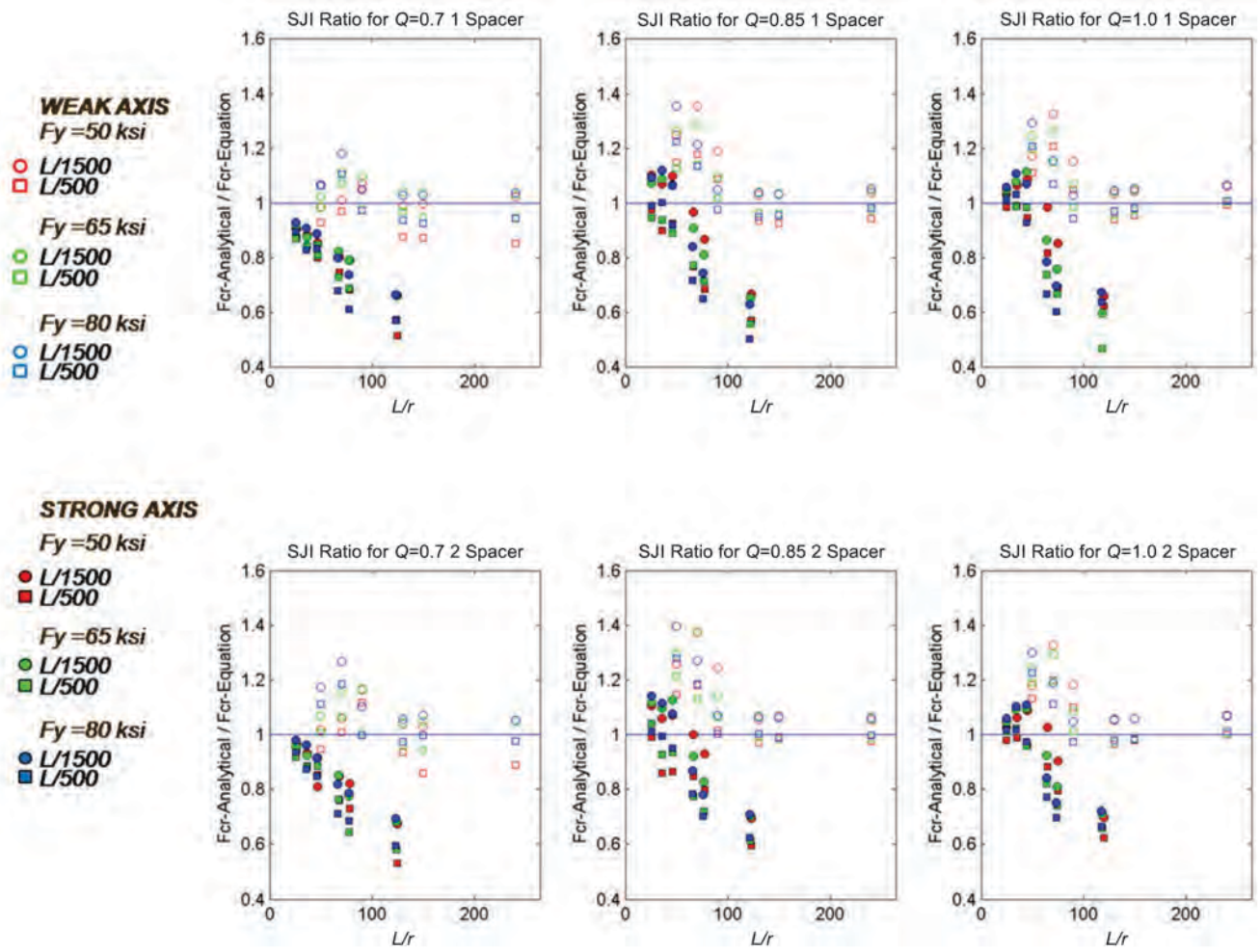


Fig. 15. LL4x4 ratios of analytical buckling strength to the SJI Specification buckling strength; L/500 and L/1500 imperfection magnitudes; $F_y = 50$ -, 65- and 80-ksi materials—organized per Q values and spacer count.

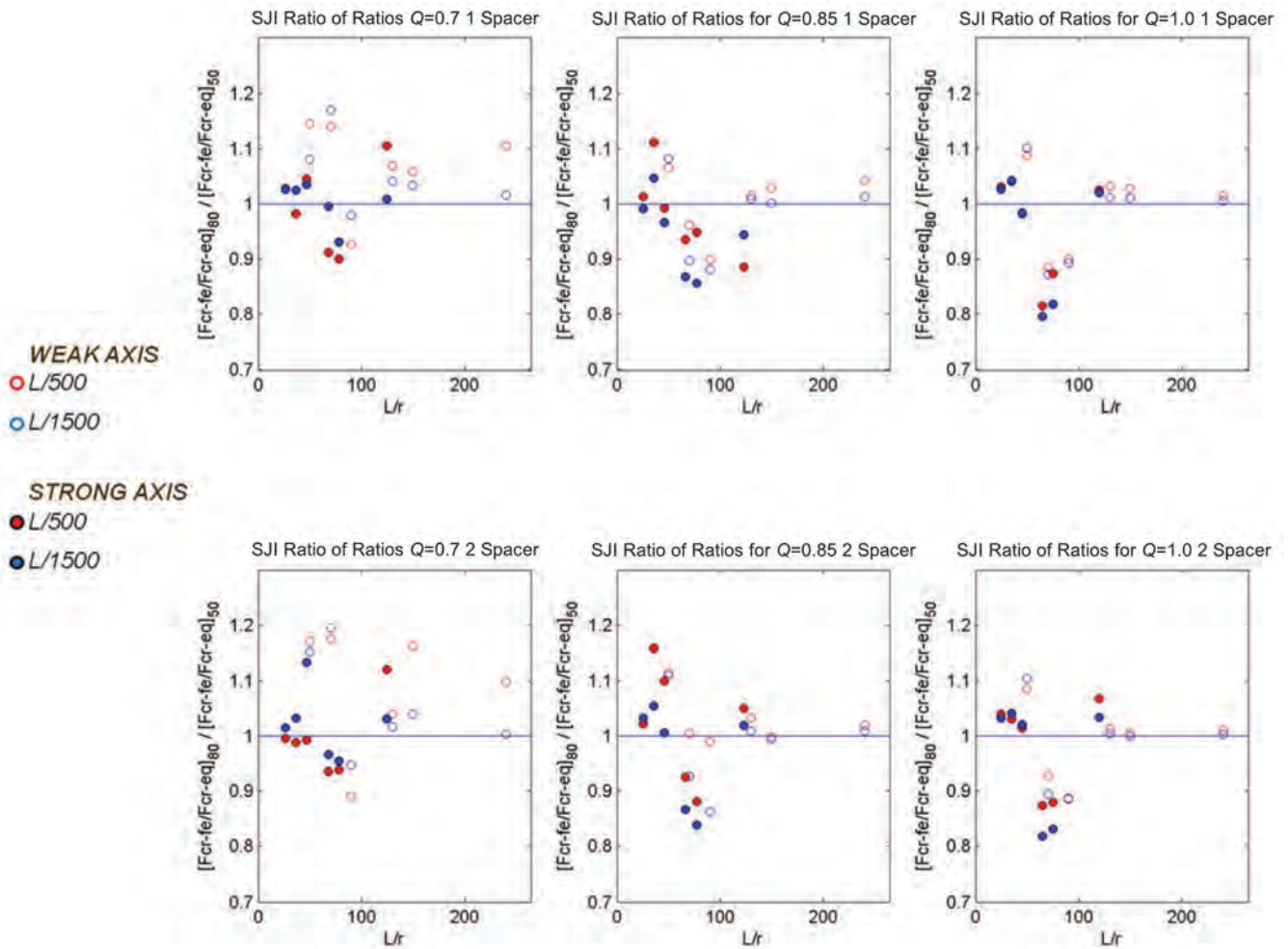


Fig. 16. LL4x4 ratio of ratios of analytical to SJI Specification buckling strength for the 80- and 50-ksi grade steel; L/500 and L/1500 imperfection magnitudes organized per Q values and spacer count.

Table 3. Global Comparison of Analytical to SJI Specification Buckling Strength Ratio of Ratios per Material Strength							
Global Average of $(P_{fe}/P_{n_SJI})_{Fy}/(P_{fe}/P_{n_SJI})_{50}$							
		L/1500			L/500		
Axis	Variable	50 ksi	65 ksi	80 ksi	50 ksi	65 ksi	80 ksi
	Q Factor						
Strong	0.7	1.000	1.040	1.015	1.000	1.036	1.009
	0.85	1.000	1.000	0.986	1.000	1.017	1.017
	1	1.000	0.991	0.986	1.000	1.000	1.001
Weak	0.7	1.000	1.056	1.048	1.000	1.077	1.084
	0.85	1.000	0.989	0.981	1.000	1.017	1.014
	1	1.000	0.993	0.986	1.000	0.999	0.995
	Number of Spacers						
Strong	1	1.000	1.000	0.984	1.000	1.007	0.999
	2	1.000	1.010	1.001	1.000	1.022	1.019
Weak	1	1.000	1.005	0.997	1.000	1.022	1.016
	2	1.000	1.005	0.998	1.000	1.024	1.028

Mean: Strong	1.000	1.005	0.992	1.000	1.014	1.009
Mean: Weak	1.000	1.005	0.998	1.000	1.023	1.022
Mean: Weak and strong	1.000	1.005	0.995	1.000	1.019	1.015
Grand total	1.000			1.011		

Tables 4 and 5 and Figures 17 through 22 illustrate the results of our study using the same format used above for presentation of the SJI Specification buckling equation comparison for different material yield stress values.

It is clear from the results that the use of the AISC buckling equations solves the nonconservatism observed with the use of the SJI equations for strong-axis bending and low Q factors. However, due to the flexural-torsional buckling check, the AISC buckling equations are highly conservative for combinations of low slenderness ratio and Q factor under 1.0. Also, as seen in Table 5, the AISC equations produce less conservative nominal buckling strength predictions for higher-strength steels than for 50-ksi steel, though they are conservative even for the higher strength steels, as indicated in Table 4.

Use of AISC Modified Slenderness Ratio Provision Only

As observed, the AISC flexural-torsional buckling equation for double-angle sections results in highly conservative strength predictions in many cases. The flexural buckling equations used alone provide better predictions for compression members with low slenderness ratios.

The following tables and figures illustrate the results of SJI adopting the AISC modified slenderness ratio provisions without the flexural-torsional buckling equations. Table 6 summarizes the ratios of the analytical results to the predicted buckling strengths. This approach provides good results, except for strong-axis buckling cases with $Q = 0.7$, where the buckling strengths are overpredicted by the SJI Specification equations and are thus unconservative. However, even for these cases, this approach provides better results than the existing SJI equations that do not include the modified slenderness ratio (Figure 12 compared to Figure 18).

Figures 23 through 25 compare normalized analytical results to predicted strengths for $Q = 1.0, 0.85$ and 0.7 , respectively. These graphs also include the test results from the Kennedy and Murty (1972) and Kitipornchai and Lee (1986) studies. These historical test results generally fall within the range of the parametric study results, with the exception of the Kennedy and Murty test results for specimens with low slenderness ratios and $Q = 1.0$, which, though at the lower edge of the range of our study results, still show good agreement with the predicted strengths using the AISC flexural buckling equation with the modified slenderness ratio.

**Table 4. Global Comparison of Analytical to AISC Specification
Nominal Buckling Strength Ratios (compare to Table 2)**

Global Average of P_{fe}/P_{n_AISC}							
Axis	Variable	L/1500			L/500		
		50 ksi	65 ksi	80 ksi	50 ksi	65 ksi	80 ksi
	Q Factor						
Strong	0.7	2.243	1.988	1.996	2.068	1.813	1.828
	0.85	1.714	1.610	1.624	1.491	1.425	1.454
	1	1.199	1.169	1.159	1.094	1.075	1.074
Weak	0.7	1.892	1.678	1.657	1.722	1.547	1.559
	0.85	1.549	1.431	1.420	1.391	1.321	1.319
	1	1.163	1.140	1.125	1.088	1.074	1.064
	Number of Spacers						
Strong	1	1.607	1.504	1.505	1.444	1.354	1.371
	2	1.643	1.532	1.538	1.474	1.387	1.399
Weak	1	1.452	1.353	1.337	1.332	1.260	1.251
	2	1.490	1.387	1.373	1.353	1.285	1.290

Mean: Strong	1.625	1.518	1.521	1.459	1.371	1.385
Mean: Weak	1.471	1.370	1.355	1.343	1.272	1.270
Mean: Weak and strong	1.548	1.444	1.438	1.401	1.322	1.328
Grand total	1.477			1.350		

Table 7 summarizes the ratios of ratios (compare to Table 3). It is clear from these results that the three material strengths result in generally similar degrees of conservatism for the range of variables in this study. For cases where $Q = 0.7$, there is slightly more conservatism for the higher-strength material specimens.

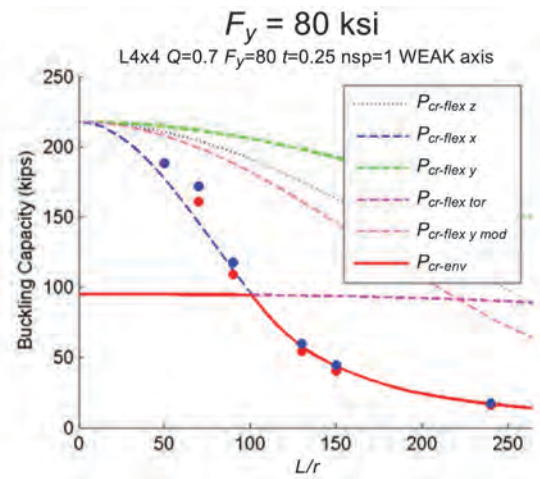
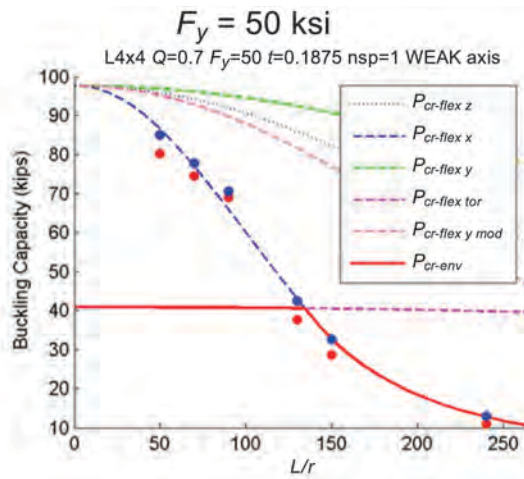
The results show that the modified slenderness ratio in the current AISC provisions significantly improves the accuracy of the SJI buckling strength predictions for strong-axis buckling of members with Q lower than 1.0. The ratio of analytical to code buckling prediction is above unity for all but the lowest Q factor value of 0.7 and strong-axis buckling using the code-basis imperfection magnitude of L/1500. The overall means are above unity for both weak- and strong-axis buckling, and the grand total mean is 1.09. Moreover, the ratios shown in Table 7 exhibit no discernible bias based on material yield stress, which means that the proposed buckling prediction equation is equally reliable for conventional 50-ksi and HSLA-V steels when considering all of the variables included in this study.

CONCLUSIONS

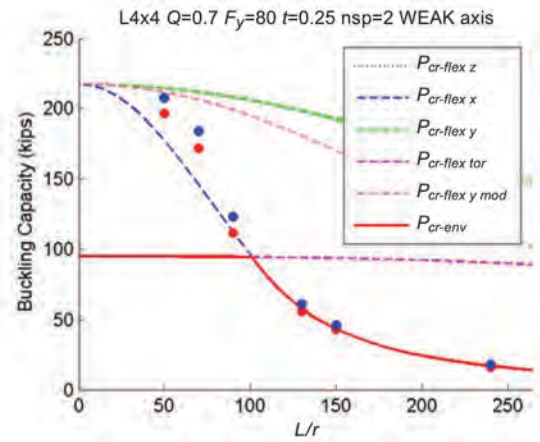
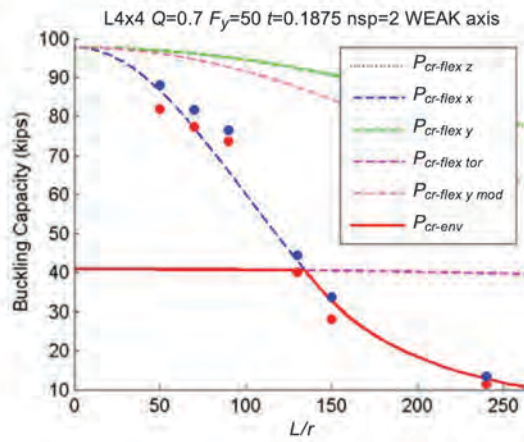
This study extensively evaluates the 2010 AISC and SJI design equations for double-angle buckling, resulting in significant findings and recommendations for both specifications.

One of the primary goals of this parametric study was to determine if the 2010 SJI design equations for double-angle buckling would produce a similar margin of safety for HSLA-V and 50-ksi steels. By comparing the ratio of the analytical buckling strength to the limiting SJI buckling strength for the higher-grade steels to the ratio of the analytical buckling strength to the limiting SJI buckling strength for the base 50-ksi strength material, it was demonstrated that there is no discernible bias in the SJI current buckling equations when used with grades representative of HSLA-V material. The overall margin of safety for the higher-yield stress HSLA-V steels is the same as 50-ksi steel when considering all of the variables included in this study.

1 spacer



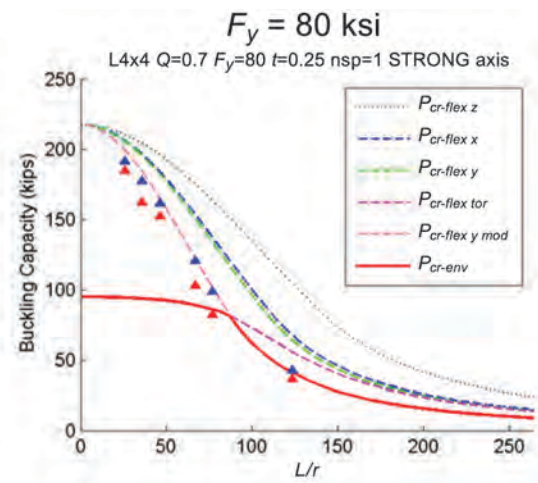
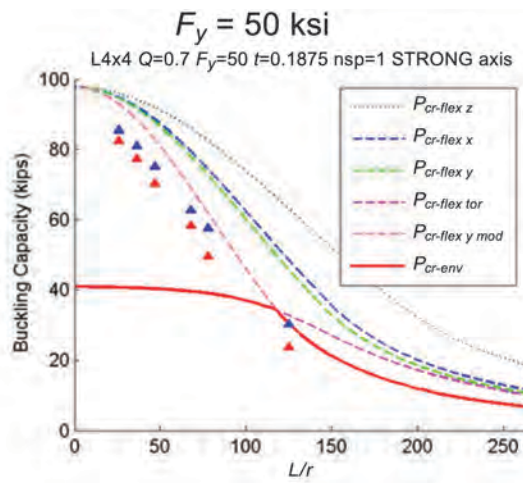
2 spacer



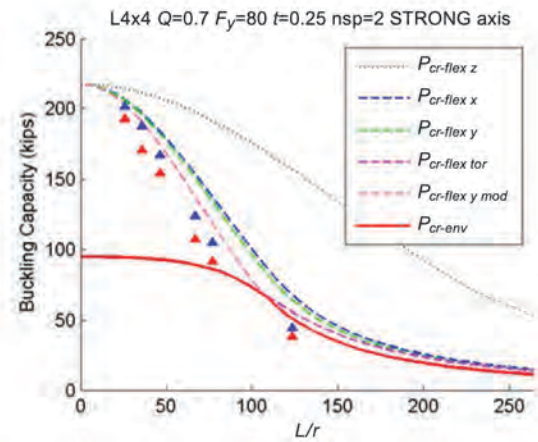
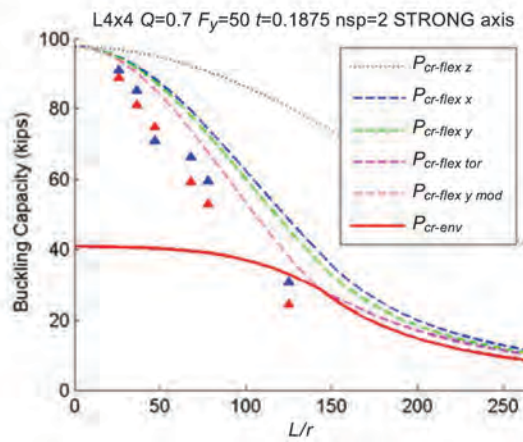
● L/1500
● L/500

Fig. 17. L4x4 analytical weak-axis (pinned) buckling strengths compared to AISC Specification equations; L/500 and L/1500 imperfection magnitudes; $F_y = 50$ -ksi and 80-ksi materials; $Q = 0.7$ (compare to Fig. 11).

1 spacer



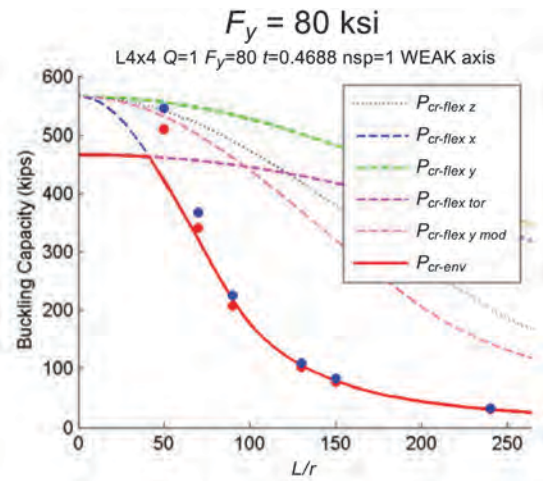
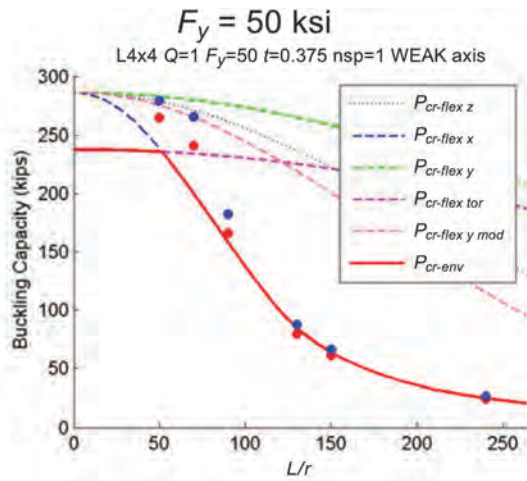
2 spacer



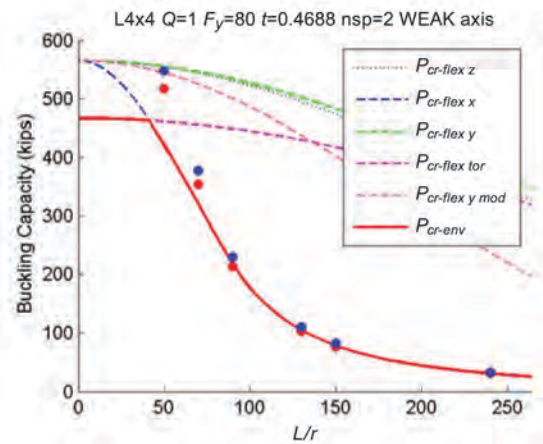
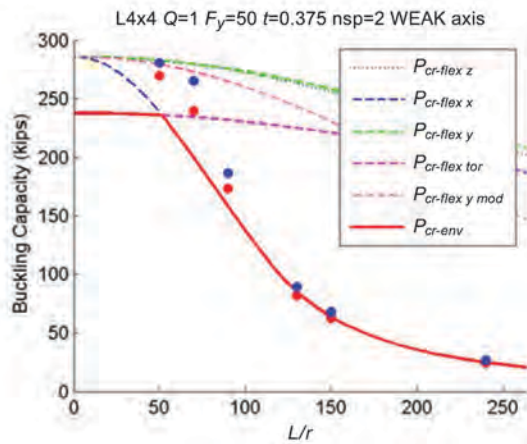
▲ $L/1500$
▲ $L/500$

Fig. 18. L4x4 analytical strong-axis (pinned) buckling strengths compared to AISC Specification equations; L/500 and L/1500 imperfection magnitudes; $F_y = 50$ -ksi and 80-ksi materials; $Q = 0.7$ (compare to Fig. 12).

1 spacer



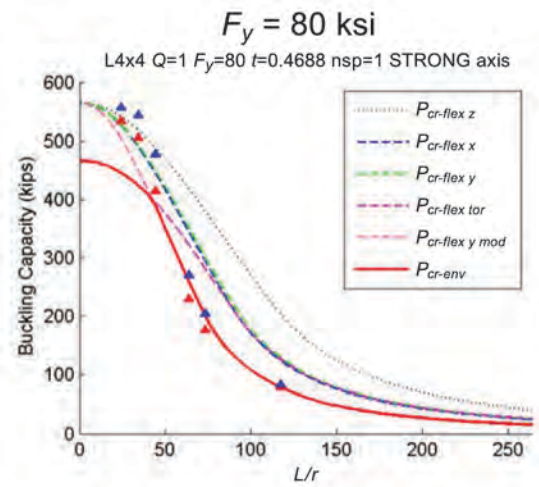
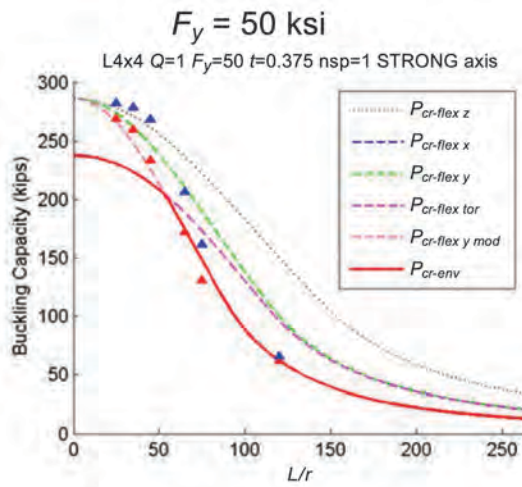
2 spacer



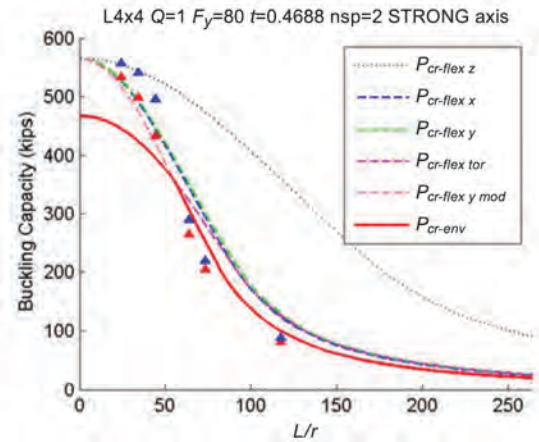
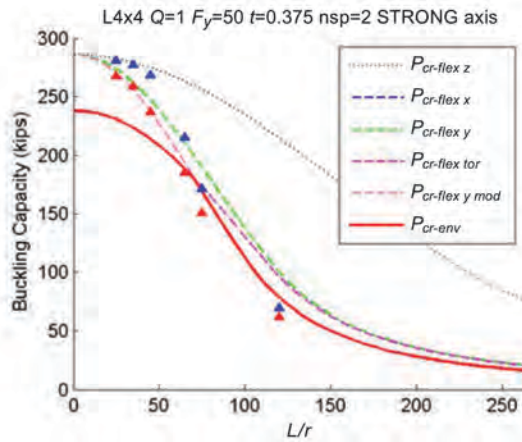
● L/1500
● L/500

Fig. 19. L4x4 analytical weak-axis (pinned) buckling strengths compared to AISC Specification equations; L/500 and L/1500 imperfection magnitudes; $F_y = 50$ -ksi and 80-ksi materials; $Q = 1.0$ (compare to Fig. 13).

1 spacer



2 spacer



▲ $L/1500$
▲ $L/500$

Fig. 20. L4x4 analytical strong-axis (pinned) buckling strengths compared to AISC Specification equations; $L/500$ and $L/1500$ imperfection magnitudes; $F_y = 50$ -ksi and 80-ksi materials; $Q = 1.0$ (compare to Fig. 14).

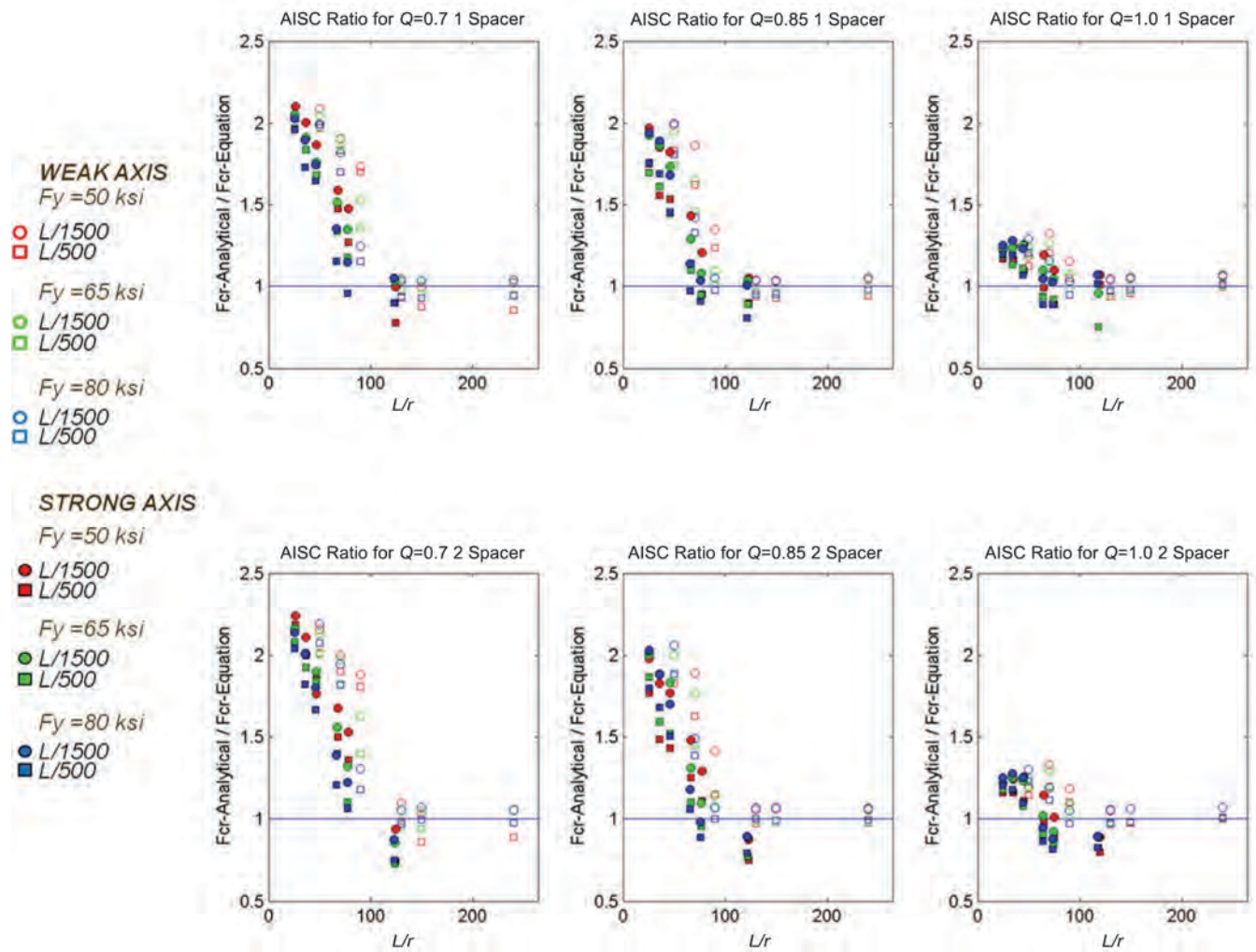


Fig. 21. LL4x4 ratios of analytical to AISC Specification nominal strength; $L/500$ and $L/1500$ imperfection magnitudes; $F_y = 50$ -, 65 - and 80 -ksi materials—organized per Q values and spacer count (compare to Fig. 15).

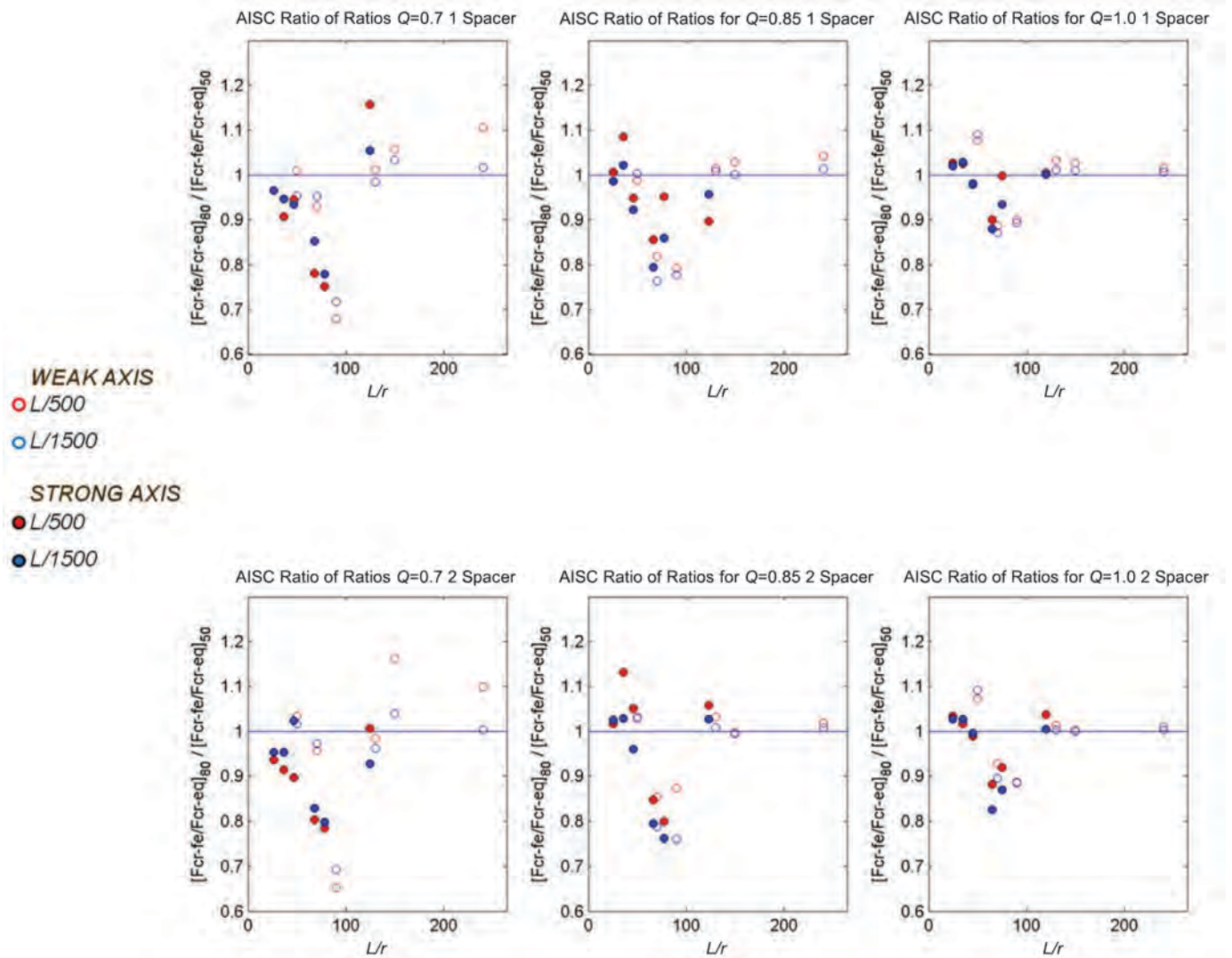


Fig. 22. LL4×4 ratio of ratios of analytical to AISC Specification nominal strength for 80- and 50-ksi grade steel; L/500 and L/1500 imperfection magnitudes—organized per Q values and spacer count (compare to Fig. 16).

**Table 5. Global Comparison of Analytical to AISC Specification
Nominal Strength Ratio of Ratios per Material Strength (compare to Table 3)**

Global Average of $(P_{fe}/P_{n_AISC})_{Fy}/(P_{fe}/P_{n_AISC})_{50}$							
Axis	Variable	L/1500			L/500		
		50 ksi	65 ksi	80 ksi	50 ksi	65 ksi	80 ksi
	Q Factor						
Strong	0.7	1.000	0.890	0.883	1.000	0.887	0.877
	0.85	1.000	0.946	0.944	1.000	0.963	0.972
	1	1.000	0.976	0.969	1.000	0.985	0.985
Weak	0.7	1.000	0.902	0.889	1.000	0.920	0.919
	0.85	1.000	0.940	0.927	1.000	0.966	0.958
	1	1.000	0.982	0.972	1.000	0.989	0.981
	Number of Spacers						
Strong	1	1.000	0.947	0.942	1.000	0.955	0.958
	2	1.000	0.944	0.939	1.000	0.956	0.957
Weak	1	1.000	0.949	0.936	1.000	0.965	0.953
	2	1.000	0.948	0.937	1.000	0.965	0.964

Mean: Strong	1.000	0.946	0.941	1.000	0.955	0.957
Mean: Weak	1.000	0.949	0.937	1.000	0.965	0.958
Mean: Weak and strong	1.000	0.947	0.939	1.000	0.960	0.958
Grand total	0.962			0.973		

Another goal of the parametric study was to determine if modifications to the 2010 SJI buckling equations would be required for the use of HSLA-V material. Results for weak-axis buckling showed that the SJI buckling equations are adequate and appropriately conservative for almost all weak-axis buckling cases included in the study. Results for strong-axis buckling showed that the SJI buckling equations are nonconservative for many cases, and the nonconservatism increases as the Q factor decreases from 1.0 to 0.7. This nonconservatism in the strong-axis buckling equations is an issue that is independent of the steel strength.

This paper investigated the following potential solutions and their impact on resolving the observed lack of conservatism in the strong-axis buckling predictions:

- SJI adoption of all AISC provisions, including flexural-torsional buckling and a modified slenderness ratio.
- SJI adoption of only the modified slenderness ratio from the AISC Specification.

The use of all the AISC buckling provisions resolved the nonconservatism observed with the use of the SJI buckling equations for strong-axis bending of members with low Q factors. However, the AISC buckling equations were overly conservative and were biased against higher-strength steels. This option is not recommended for adoption.

The modified slenderness ratio in the AISC provisions significantly improved the accuracy of the SJI buckling strength predictions for strong-axis buckling cases for members with Q values less than 1.0. Furthermore, the results did not show significant bias in conservatism in relation to material strength. The authors strongly recommend that SJI consider adopting the AISC slenderness modification ratio for built-up members into the SJI Specifications. [Note: SJI adopted the modified slenderness ratio for built-up web members in its 2015 Specification (SJI, 2015).]

Additional investigation of the use of the AISC flexural-torsional buckling equations for double angles is recommended because this study suggests that these provisions produce overly conservative results in the low slenderness ratio range.

Table 6. Global Comparison of Analytical to AISC Specification Nominal Buckling Strength Ratios Excluding Flexural-Torsional Buckling Checks (compare to Table 2)

Global Average of P_{fe}/P_n _AISC_NoFT_Balloted							
Axis	Variable	L/1500			L/500		
		50 ksi	65 ksi	80 ksi	50 ksi	65 ksi	80 ksi
	Q Factor						
Strong	0.7	0.898	0.950	0.936	0.819	0.861	0.846
	0.85	1.091	1.094	1.089	0.949	0.969	0.976
	1	1.087	1.075	1.084	0.988	0.987	1.003
Weak	0.7	1.047	1.102	1.093	0.946	1.014	1.020
	0.85	1.185	1.172	1.161	1.065	1.083	1.081
	1	1.135	1.126	1.115	1.062	1.061	1.054
	Number of Spacers						
Strong	1	1.062	1.076	1.070	0.950	0.969	0.973
	2	1.034	1.036	1.038	0.924	0.937	0.944
Weak	1	1.124	1.127	1.116	1.030	1.051	1.043
	2	1.148	1.151	1.141	1.047	1.069	1.071

Mean: Strong	1.048	1.056	1.054	0.937	0.953	0.959
Mean: Weak	1.136	1.139	1.129	1.038	1.060	1.057
Mean: Weak and strong	1.092	1.098	1.091	0.988	1.006	1.008
Grand total	1.094			1.001		

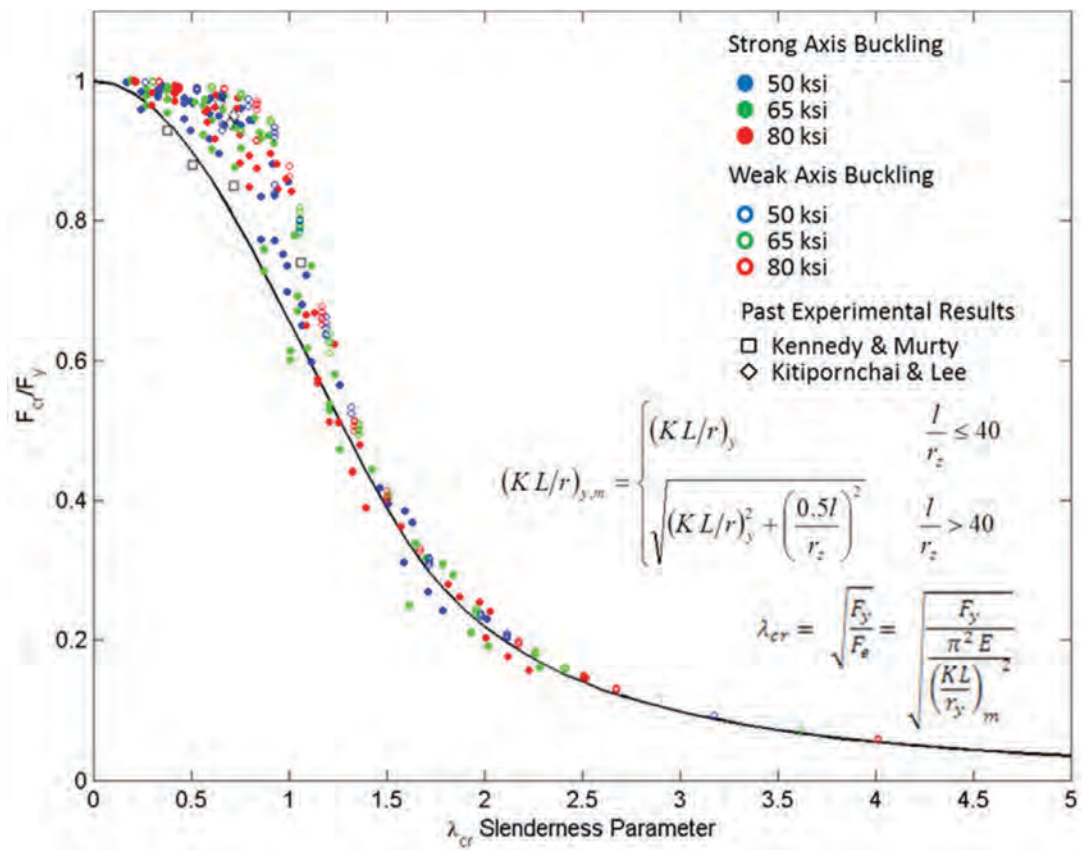


Fig. 23. Comparison of the normalized flexural buckling equation and parametric study analyses with $Q = 1.0$ and using the AISC slenderness modification for built-up sections.

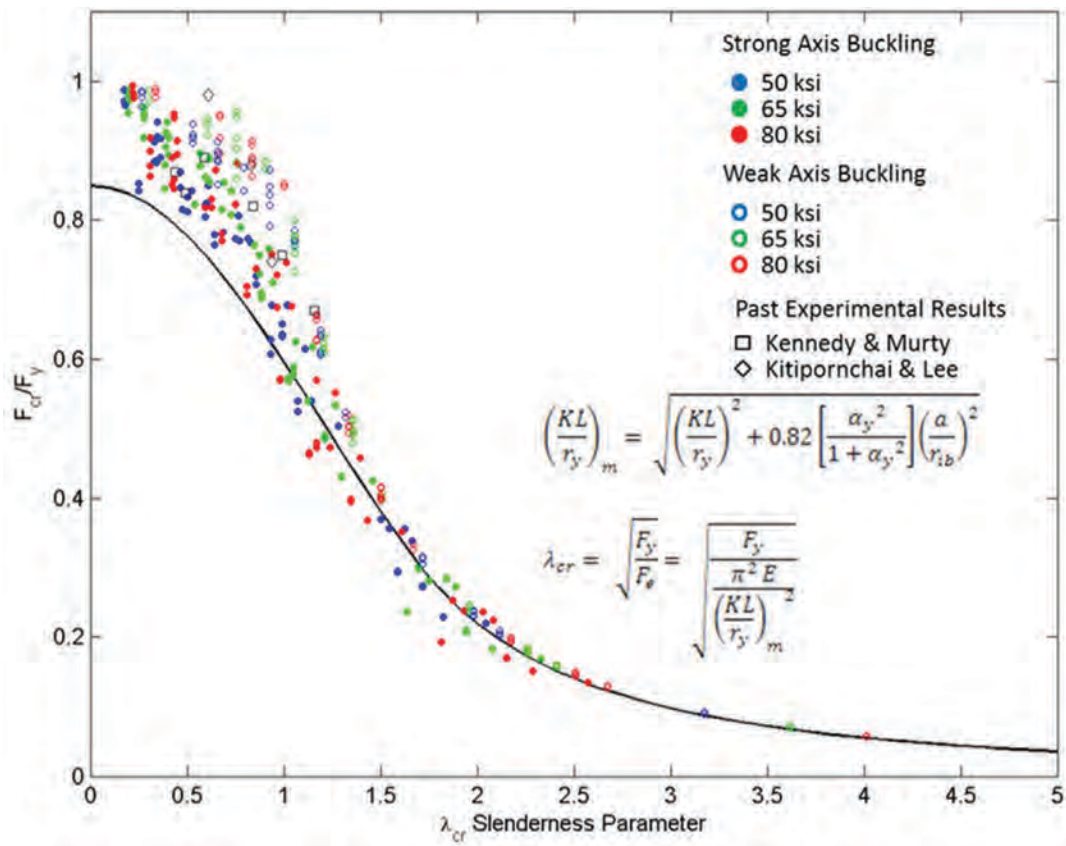


Fig. 24. Comparison of the normalized flexural buckling equation and parametric study analyses with $Q = 0.85$ and using the AISC slenderness modification for built-up sections.

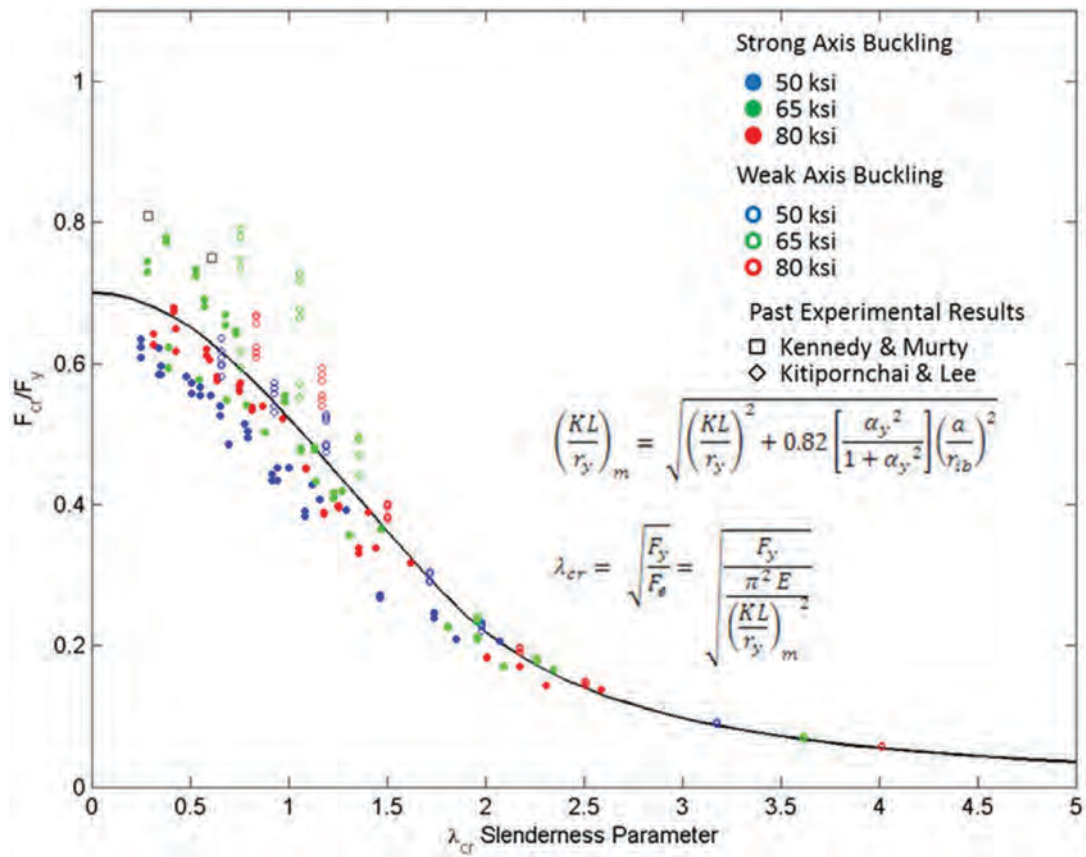


Fig. 25. Comparison of the normalized flexural buckling equation and parametric study analyses with $Q = 0.7$ and using the AISC slenderness modification for built-up sections.

Table 7. Global Comparison of Analytical to AISC Specification Nominal Buckling Strength Ratio of Ratios Excluding Flexural-Torsional Buckling Checks (compare to Table 3)

Global Average of $(P_{fe}/P_{n_AISC_NoFT_Bal})_{Fy}/(P_{fe}/P_{n_AISC_NoFT_Bal})_{50}$							
Axis	Variable	L/1500			L/500		
		50 ksi	65 ksi	80 ksi	50 ksi	65 ksi	80 ksi
	Q Factor						
Strong	0.7	1.000	1.059	1.043	1.000	1.056	1.037
	0.85	1.000	1.002	0.997	1.000	1.020	1.028
	1	1.000	0.989	0.999	1.000	0.997	1.015
Weak	0.7	1.000	1.053	1.045	1.000	1.074	1.080
	0.85	1.000	0.991	0.983	1.000	1.018	1.016
	1	1.000	0.994	0.986	1.000	1.000	0.994
	Number of Spacers						
Strong	1	1.000	1.015	1.009	1.000	1.022	1.025
	2	1.000	1.004	1.006	1.000	1.016	1.024
Weak	1	1.000	1.005	0.997	1.000	1.022	1.015
	2	1.000	1.005	0.998	1.000	1.024	1.027

Mean: Strong	1.000	1.009	1.007	1.000	1.019	1.025
Mean: Weak	1.000	1.005	0.997	1.000	1.023	1.021
Mean: Weak and strong	1.000	1.007	1.002	1.000	1.021	1.023
Grand total	1.003			1.015		

REFERENCES

- ABAQUS (2007), *ABAQUS User's Manual*, Version 6.7, Dassault Systemes, RI.
- AISC (1978), *Specification for the Design, Fabrication and Erection of Structural Steel for Buildings*, American Institute of Steel Construction, Chicago, IL.
- AISC (2010), *Specification for Structural Steel Buildings*, ANSI/AISC 360, American Institute of Steel Construction, Chicago, IL.
- AISI (1968), *Specifications for the Design of Cold-Formed Steel Structural Members*, American Iron and Steel Institute, Washington, DC.
- Aslani, F. and Goel, S. (1991), "An Analytical Criterion for Buckling Strength of Built-up Compression Members," *Engineering Journal*, AISC, Vol. 28 No. 4.
- ASTM (2007), "Standard Specification for High-Strength Low-Alloy Columbium-Vanadium Structural Steel," A572/A572M-07, ASTM International, West Conshohocken, PA.
- ASTM (2008), "Standard Specification for Carbon Structural Steel," A36/A36M-08, ASTM International, West Conshohocken, PA.
- Chuenmei, G. (1984), "Elastoplastic Buckling of Single Angle Columns," *Journal of Structural Engineering*, Vol. 110, No. 6, pp. 1,391–1,395.
- Elgaaly, M., Dagher, H. and Davids, W. (1991), "Behavior of Single-Angle-Compression Members," *Journal of Structural Engineering*, Vol. 117, No. 12, pp. 3,720–3,741.
- Elgaaly, M., Dagher, H. and Davids, W. (1992), "Non-Slender Single Angle Struts," *Engineering Journal*, AISC, Vol. 29, No. 2.
- Galambos, T.V. (1991), "Design of Axially Loaded Compressed Angles," *Proceedings, 1991 Annual Technical Session, Inelastic Behavior and Design of Frames*, AISC, April 15–17.
- Kennedy, J.B. and Murty, M.K.S. (1972), "Buckling of Steel Angle and Tee Struts," *Journal of the Structural Division*, ASCE, Nov.

- Kennedy, J.B. and Murty, M.K.S. (1982), "Buckling of Angles: State of the Art," *Journal of the Structural Division*, ASCE, Sept.
- Kitipornchai, S. and Lee, H.W. (1986), "Inelastic Experiments on Angle and Tee Struts," *Journal of Constructional Steel Research*, Vol. 6, pp. 219–236.
- Popovic, D., Hancock, G.J. and Rasmussen, K.J.R. (1999), "Axial Compression Tests of Cold-Formed Angles," *Journal of Structural Engineering*, ASCE, May.
- Salmon, C.G. and Johnson, J.E. (1990), *Steel Structures: Design and Behavior*, 3rd Ed., Harper & Row, New York, NY.
- SGH (2011), *Correlation and Sensitivity Study on the Buckling of HSLA-V Steel in Single and Double Angle Members*, Project 047079, Simpson Gumpertz and Heger Inc.
- SGH (2012), *Parameter Study to Assess Modifications to the SJI Design Equations for HSLA-V Steels. Rev.1.*, Project 047079, Simpson Gumpertz and Heger Inc.
- SJI (2010), *Standard Specification for Longspan Steel Joists, LH-Series and Deep Longspan Steel Joists, DLH-Series*, ANSI/SJI-LH/DLH, Steel Joist Institute, Florence, SC.
- SJI (2015), *Standard Specification for K-Series, LH-Series, and DLH-Series Open Web Steel Joists and for Joist Girders*, ANSI/SJI 100, Steel Joist Institute, Florence, SC.
- Talaat, M.M., Mayes, R.L., Webster, M.D., Citipitioglu, A. and Kan, F.W. (2017), "Buckling of Conventional and High-Strength Vanadium Steel Double-Angle Compression Members: Computational Parametric Evaluation of Slenderness Modification Factors." *Engineering Journal*, AISC, Vol. 54, No. 4.
- XYZ Scientific Applications (n.d.), *TrueGrid*. Livermore, CA: <http://www.truegrid.com>.

Buckling of Conventional and High-Strength Vanadium Steel Double-Angle Compression Members: Computational Parametric Evaluation of Slenderness Modification Factors

MOHAMED M. TALAAT, RONALD L. MAYES, MARK D. WEBSTER,
AHMET CITIPITIOGLU and FRANK W. KAN

ABSTRACT

High-strength, low-alloy vanadium (HSLA-V) steel offers higher strength and toughness than conventional steel. The resulting lighter weight and more slender structural components are more susceptible to buckling in compression. Of particular interest to this study are open-web joists, which utilize double-angle sections—typically for chord members and often for web members. Design specification treatment for both global and specifically local buckling of double-angle compression members is evaluated in this study. Specification equation predictions of the buckling load strength for a wide range of specimens and material strengths are examined and compared to analytical simulations. This paper proposes two alternative modifications to the so-called Q-factor formulation in order to address the nonconservative buckling strength predictions for double-angle compression members with low Q factors. This study concludes that the adoption of a modified Q-factor formulation for local elements of compression members in the element elastic buckling region produces consistent predictions of the buckling strength. This finding is equally applicable to both HSLA-V and conventional steels. For design and other applications where a lower-bound estimate of the strength is required, this combination of proposed Q-factor formulation and AISC built-up member slenderness modification is recommended.

Keywords: high-strength vanadium steel, compression, computational parametric study, modification factors, buckling analysis, Q factor.

INTRODUCTION

A long-term research project sponsored by the Army Research Laboratory (ARL) under Cooperative Agreement DAAD 19-03-2-0036 and executed by the Advanced Technology Institute (ATI) was initiated in 2003 to assess the impact of high-strength, low-alloy microalloyed vanadium (HSLA-V) steels on a wide variety of different applications. HSLA-V steels can have specified yield strengths of up to 90 ksi and thus provide the opportunity both for weight reduction and enhanced sustainability.

This paper evaluates the treatment for both global and specifically local buckling of double-angle compression members in the Steel Joist Institute (SJI) Specification and proposes modifications to improve the specification equation buckling strength results for a wide range of parameters and material strength. It presents results from a computational correlation and parametric study the authors performed on double-angle compression components (SGH, 2011, 2012) and complements a companion paper by the authors (Webster et al., 2017).

In *Correlation and Sensitivity Study on the Buckling of HSLA-V Steel in Single and Double Angle Members* (SGH, 2011), the authors described the successful use of nonlinear finite element (FE) analysis to closely match buckling failure modes and strengths observed in 20 double-angle compression member tests with a range of properties. Based on the success of this correlation study and verification of the modeling and simulation approach, a parametric study was executed to extend the range of parameters beyond those in the physical test program.

In the companion paper (Webster et al., 2017), the authors described the validity of applying the buckling equations in the SJI Design Specification (SJI, 2010) to double-angle compression members manufactured using higher strength HSLA-V steel. Present SJI specifications are applicable only for steel with specified yield stress of 50 ksi or less.

Mohamed M. Talaat, Adjunct Assistant Professor, Cairo University, Egypt and Senior Structural Engineer, Simpson Gumpertz & Heger Inc., Newport Beach, CA. Email: MTalaat@sgh.com (corresponding)

Ronald L. Mayes, Staff Consultant, Simpson Gumpertz & Heger Inc., San Francisco. Email: RLMayes@sgh.com

Mark D. Webster, Senior Structural Engineer, Simpson Gumpertz & Heger Inc., Waltham, MA. Email: MDWebster@sgh.com

Ahmet Citipitioglu, Director of Engineering and Design, TAV Construction, İstanbul, Turkey. Email: Ahmet.Citipitioglu@tav.aero

Frank W. Kan, Principal, Simpson Gumpertz & Heger Inc., Waltham, MA. Email: FWKan@sgh.com

The design equations for compression buckling in the SJI Specification were also compared to the 2010 American Institute of Steel Construction (AISC) *Specification*. For both conventional and HSLAV steel members, the Webster et al. study found that the flexural-torsional buckling equation in AISC produces highly conservative estimates of nominal buckling strength and that the 2010 AISC slenderness modification for built-up members enhances the accuracy of the SJI buckling equations, which do not incorporate the AISC flexural-torsional buckling provisions. When comparing the analytical results to the nominal buckling strengths calculated using SJI equations, the observed differences showed a pattern dependence on element local slenderness—that is, the Q factor. The use of AISC built-up member slenderness modification improved the accuracy of the buckling equation on average yet did not significantly reduce this dependence on element slenderness. [Note: SJI adopted the modified slenderness ratio for built-up web members in its 2015 Specification (SJI, 2015)]

This paper extends the analytical parametric study to examine the effect of element slenderness (Q factor) on the accuracy of the specification buckling equations. The analytical and design specification nominal buckling strengths of double-angle members with Q factors ranging from 0.7 to 1.0 are compared. The impacts of introducing two proposed reformulations of the Q factor are examined. The two alternative Q -factor formulations are based on the American Iron and Steel Institute (AISI) 1968 *Specifications for the Design of Cold-Formed Steel Structural Members*. The influence of each alternative Q factor is examined with and without the modified built-up section slenderness ratio as defined in the 2010 AISC *Specification*.

PROVISIONS FOR BUCKLING IN SJI AND AISC SPECIFICATION

The estimation of the critical buckling load depends on the mode and type (i.e., elastic or inelastic) of buckling. Critical buckling load is computed for several possible buckling modes depending on the compression member profile. The lowest critical load for the associated buckling mode is assumed to represent the governing buckling phenomenon. The SJI Specification mostly follows the AISC *Specification* but ignores the provisions for built-up member slenderness modification and flexural-torsional buckling. The details of these equations are discussed in the authors' companion paper, mentioned earlier (Webster et al., 2017). This paper focusses on an assessment of various formulations for the Q -factor definition.

Element Slenderness Modification

Compression members with slender cross-section elements have a reduced inelastic buckling strength due to local instabilities that can be evaluated based on plate buckling theory. To capture this local effect, a reduction factor, Q , is introduced to the buckling equations as a reduction multiplier to the material yield strength, with values ranging from 0.7 to 1.0 for common angle sizes.

The local slenderness of an element of the compression member (i.e., angle leg) is determined by the ratio of element size to thickness (b/t) and material yield stress. More slender elements have lower Q -factor values (Figure 1) and thus greater reduction in the buckling strength.

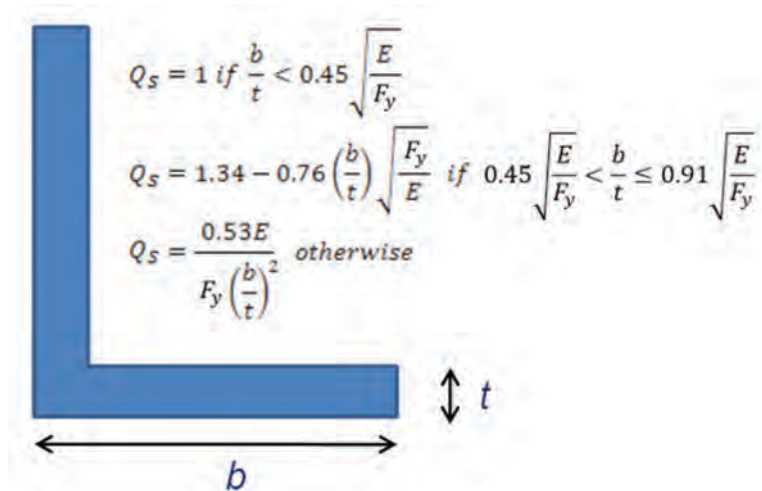


Fig. 1. Angle local element slenderness ratio.

Modified Flexural Buckling for Built-Up Sections

The member slenderness term may be modified if the compression member is built up from two or more sections and interconnected by bolted or welded elements. The modification in slenderness accounts for the impact on the buckling strength of the relative displacement due to shear forces in the connectors between the individual components forming the member. For double angles with welded spacers, the 2010 AISC *Specification* modifies the slenderness ratio as follows:

$$\text{For } \frac{a}{r_i} \leq 40 \quad (KL/r)_{y,m} = (KL/r)_o \quad (1)$$

$$\text{For } \frac{a}{r_i} > 40 \quad (KL/r)_{y,m} = \sqrt{(KL/r)_o^2 + (K_i a/r_i)^2} \quad (2)$$

where $(KL/r)_{y,m}$ is the modified slenderness ratio of the built-up member, $(KL/r)_o$ is the slenderness ratio of the built-up member acting as a unit, $K_i = 0.50$ for back-to-back angles, a is the connector spacing along the length of the compression member, and r_i is the minimum radius of gyration of an individual component.

This modification addresses the ability of the built-up section to act compositely in the direction(s) where the radius of gyration of a single component is significantly less than the distance between the centroids of the individual components and, consequently, than the composite radius of gyration of the built-up member (Aslani and Goel, 1991). In the case of double-angle compression members, this modification applies only to strong-axis buckling because the spacers have no influence in the weak-axis buckling case.

Effect of Modification Factors on Strong-Axis Flexural Buckling Strength

The critical stress for flexural buckling given in both the SJI *Specification* and the 2010 AISC *Specification* is as follows:

$$F_{cr} = \min_i \left\{ \begin{array}{l} \left(0.658 \frac{QF_y}{F_{e,i}} \right) QF_y \\ 0.877 F_{e,i} \end{array} \right\} \quad (3)$$

$$(KL/r)_i \leq 4.71 \sqrt{\frac{E}{QF_y}}, \quad \frac{QF_y}{F_e} \leq 2.25$$

$$(KL/r)_i > 4.71 \sqrt{\frac{E}{QF_y}}, \quad \frac{QF_y}{F_e} > 2.25$$

where F_{cr} is the critical buckling stress, Q is the section element slenderness reduction factor for unstiffened elements,

$$F_{e,i} = \frac{\pi^2 E}{(KL/r)_i^2}$$

stress, E is the material's Young's modulus of elasticity, and KL/r is the slenderness ratio of the compression member (modified for built-up sections in AISC). Subscript i refers to the two buckling axes: strong and weak axis.

Hence, the material yield stress is multiplied directly by the Q factor and reduced to account for local buckling of slender elements, while the modified global slenderness indirectly reduces the nominal buckling strength by reducing the value of the elastic buckling stress to account for influence of the built-up section.

BACKGROUND AND PROPOSED MODIFICATIONS FOR Q FACTOR

The companion paper by the authors that presented the computational parameter study (Webster et al., 2017) reviewed past research on single- and double-angle buckling behavior, published over the course of nearly three decades. The following sections will present the theoretical and historical development of the Q factor.

Theoretical Development of Element Slenderness Factor

The 2010 AISC *Specification* identifies two types of elements when considering local buckling depending on the element disposition within the overall member (Figure 2). An element bounded on both edges along its length with other elements, such as the web of an I-beam, is defined as a *stiffened element*. An element that has one free edge along its length, such as the leg of an angle, is defined as an *unstiffened element*.

The 2010 AISC slender element reduction factor for unstiffened slender member elements (e.g., angle legs), Q_s , is directly based on a simple-element, elastic buckling model of a plate subjected to uniform in-plane compression. The reduction factor is simply the ratio of the critical (local) buckling stress determined by this simple plate model to the material yield strength. This reduction factor is directly applied to the material yield strength when specifying the overall member nominal buckling strength.

The plate elastic buckling stress relationship is given in Equation 4, where μ is the material Poisson ratio and k is a plate buckling coefficient dependent on the plate boundary conditions and aspect ratio. For unstiffened slender-angle elements, the buckling coefficient, k converges to 0.425:

$$F_{cr} = k \frac{\pi^2 E}{12(1-\mu^2)(b/t)^2} \quad (4)$$

Figure 3 plots the ratios of critical buckling stress to yield stress versus compression member slenderness for plates and columns. Three distinct regions of behavior are observed in this figure:

- For very slender elements with a slenderness parameter, λ_c greater than 1.4 the buckling is essentially elastic.
- For very stout elements (λ_c less than e.g. 0.46 for plates), the entire cross-section under compression can reach and exceed the yielding stress of the material by hardening. However, for design purposes, hardening in the material is ignored, and the cross-section strength is limited to the material yield stress.
- Finally, there is a transition zone between the element elastic buckling region and the full yielding region, where the buckling strength is lower than the theoretical critical load envelope (solid line in Figure 3) due to residual stress and geometric imperfections.

For unstiffened plates under uniform compression, the transition zone is idealized as a linear transition as shown in Figure 4a, which also compares the analytical buckling

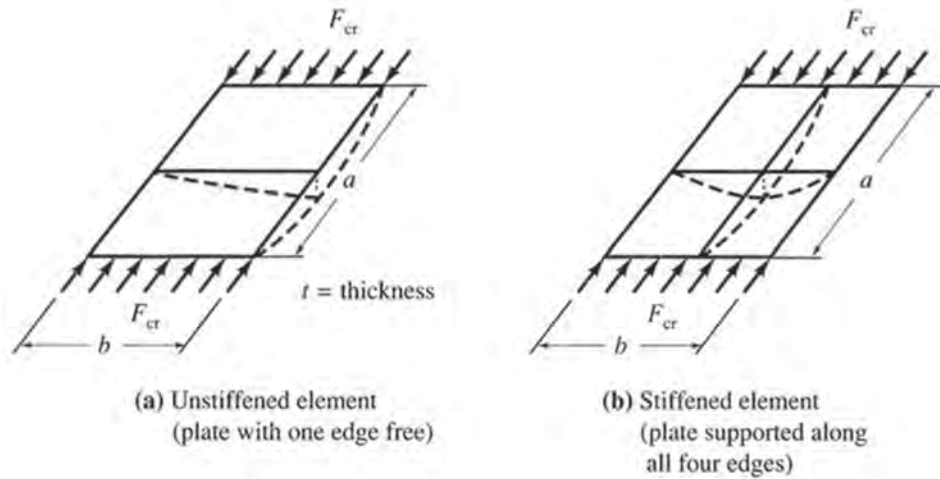


Fig. 2. Plate buckling configuration for unstiffened and stiffened compression elements [AISI S100-2007-C (AISI, 2007)].

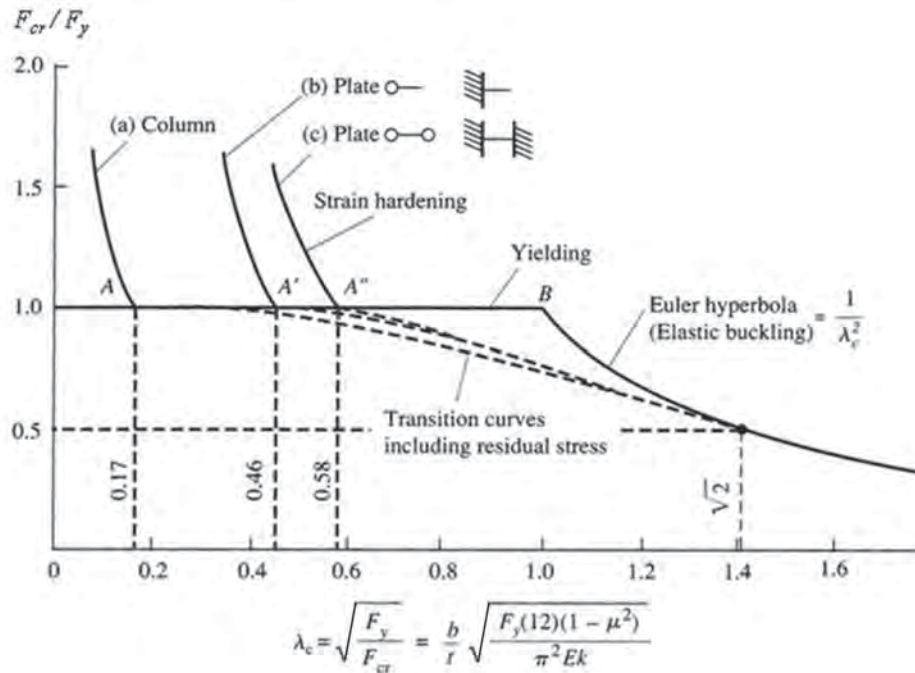


Fig. 3. Comparison of critical buckling stress to yield stress ratio versus member slenderness for (a) columns, (b) unstiffened plates, and (c) stiffened plates (Salmon and Johnson, 1990).

stresses defined in the three regions to test results. For each test, two data points are plotted in the figure: the local buckling stress and the member failure stress. For stout compression members with low slenderness parameters, the difference between the two plotted points is small, whereas as the slenderness parameter increases the difference between the two points becomes greater. This is attributed to the post-buckling strength where the section stress increases as the applied displacement increases.

The additional post-buckling strength available in slender elements is accounted for by increasing the element elastic buckling stress as shown in Figure 4b. Line A marks the strength of elements that are stout enough to reach the full-section yield strength. Line B is the linear transition zone between the element yielding and elastic buckling zones. Line D is the plate elastic buckling curve, which is increased by a factor to account for the post-buckling strength mentioned earlier and is shown with line E.

The 2010 AISC *Specification* accounts for post-buckling strength of unstiffened elements as depicted by line E in Figure 4b. The 1968 AISI Specification ignored this additional strength for angle components, stating the following in its Commentary: “There is a type of cross-section composed entirely of unstiffened elements which shows little or no post-buckling strength. This is the angle section when used for compression struts. This is because, when an equal leg, thin angle reaches the buckling stress of the two equal, component plates (legs), both of them buckle in the same direction; this results in a twisting distortion of the angle as a whole, leading to early collapse...” The compression strength is thus distinguished for angle components, as shown in Figure 5a. The 2010 AISC *Specification* does not distinguish the behavior of slender elements and slender angle legs, as shown in Figure 5b.

Proposed Q Factor Modifications

Two alternative redefinitions for the slender cross-section element buckling reduction factor, Q , are proposed and assessed in this study. Both proposals are based on a return to the 1968 AISI Specification that did not consider post-buckling strength for angle components. The two alternative Q -factor formulations use the plate elastic buckling formulation for calculating the local buckling strength of slender elements. Alternative 1, Q_{A1} , shown in Figure 6, uses the plate elastic buckling relationship up to the point where it intersects the linear transition zone as defined in the 2010 AISC *Specification*. Alternative 2, Q_{A2} , shown in Figure 7, uses the plate elastic buckling relationship until it reaches the full cross-section yield strength.

COMPUTATIONAL PARAMETER STUDY

The parameter study consisted of analytical buckling simulations on double-angle specimens made of steel materials with 50-, 65- and 80-ksi nominal yield strengths (Candas et

al., 2008). The angle sizes included in the study were LL8×8, LL6×6, LL4×4 and LL2×2. The parameters assessed were the member slenderness (KL/r), element slenderness (Q factor), number of spacers, the imperfection magnitude, and the end conditions about the weak and strong axes. A total of 3552 cases were analyzed, resulting in a database of 1776 buckling strengths.

The generation of the set of parametric models was automated using customized scripts and the mesh generation program Truegrid (XYZ Scientific Computing, n.d.) The buckling analyses of the double angles were carried out using the general-purpose, nonlinear, FE software ABAQUS. ABAQUS has extensive capabilities for modeling continuum mechanics, including contact, and for solving elastic buckling as well as unstable post-buckling problems. The nonlinear buckling analyses were solved using the Modified Riks algorithm, which is available in ABAQUS for loading regimes with geometrically unstable phases. Further details are discussed in the companion paper (Webster et al., 2017).

Analysis Results

Table 1 summarizes the ratios of buckling strengths from the analysis results to the nominal buckling strengths calculated using the SJI Specification equations for the different parameter study variables. The comparison results are shown for modeled geometric imperfection magnitude values of code-basis $L/1500$ as well as $L/500$. The results for weak-axis buckling show that the SJI buckling equations are adequate and appropriately conservative for nearly all the cases included in the study. The results for strong-axis buckling show that the SJI buckling equations are nonconservative for many cases in the study. This nonconservatism is particularly pronounced for cases where $Q = 0.7$ and is present for all three steel grades.

While the average strong-axis results for $Q = 1.0$ and $Q = 0.85$ cases are above unity when the code-basis $L/1500$ imperfection magnitude is used (note that the ratios for $Q = 0.85$ are slightly yet consistently more conservative than $Q = 1.0$), the results for several individual specimens are nonconservative, as can be seen in Figure 8. Hence, this nonconservatism increases as the member slenderness (L/r) and/or element slenderness (b/t) increases.

To address the nonconservatism in the strong-axis buckling results, the two alternative formulations proposed for the Q factor were investigated. In the companion paper, the adoption of all the 2010 AISC *Specification* buckling equations and the adoption of selected provisions addressing the built-up member slenderness (KL/r) modification equation were evaluated. In this study, the influence of the proposed changes to the Q -factor calculation in order to specifically address the nonconservatism associated with the low Q factors is evaluated. Using the proposed Q factors both with and without the AISC built-up member slenderness modification is also assessed.

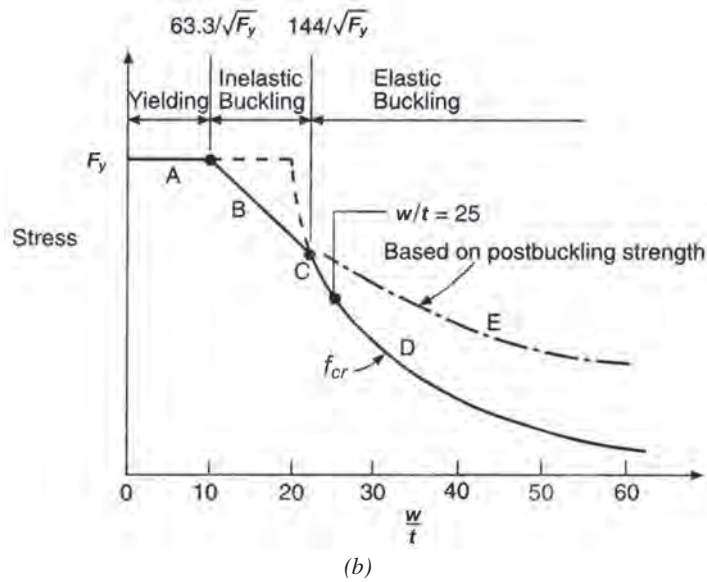
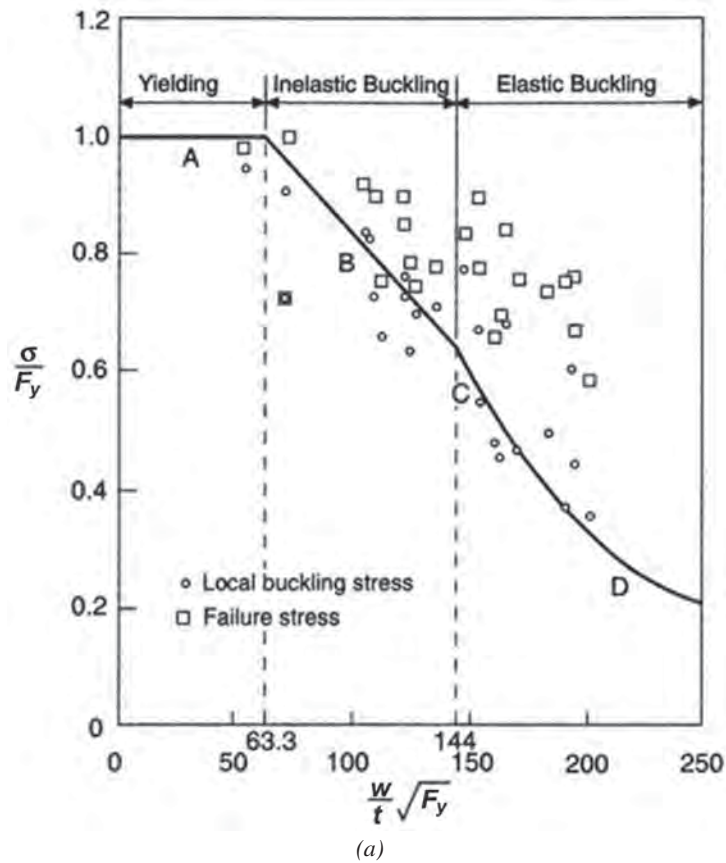


Fig. 4. Relationship between unstiffened compression plate elements and predicted maximum compressive stress: (a) correlation between test data and predicted maximum stress (Yu, 2010); (b) comparison between idealizations that include and exclude post-buckling strength (AISI S100-2007-C).

PROPOSED MODIFICATIONS TO ELEMENT AND COMPONENT SLENDERNESS EFFECTS

Element Slenderness

The slender cross-section element buckling reduction factor alternatives Q_{A1} and Q_{A2} introduced in Figures 6 and 7 are based on the 1968 AISI assumptions regarding slender angle cross-sections and their inability to develop post-buckling strength due to twisting instability in the angle

legs once the element elastic buckling load is reached. A preliminary comparison of both alternatives suggests the following characteristics:

1. Alternative Q_{A1} represents a more limited change from the 2010 provisions, while alternative Q_{A2} represents a more simplified relationship for design.
2. For elements in the elastic local buckling region ($Q < 0.8$), both alternatives result in lower Q factor values than

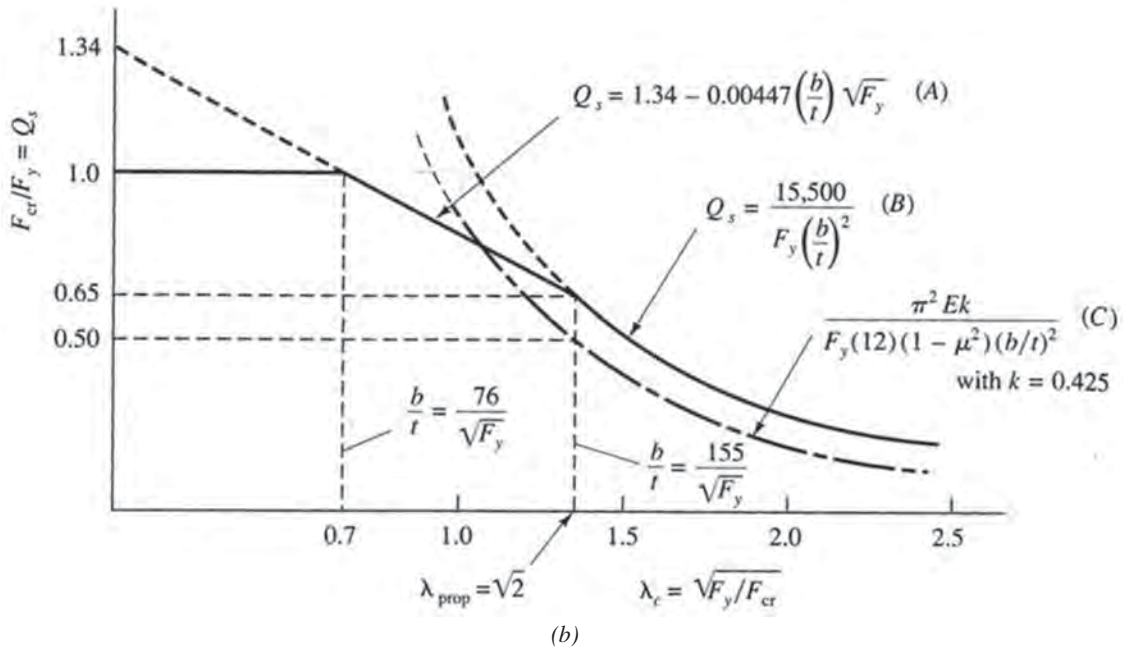
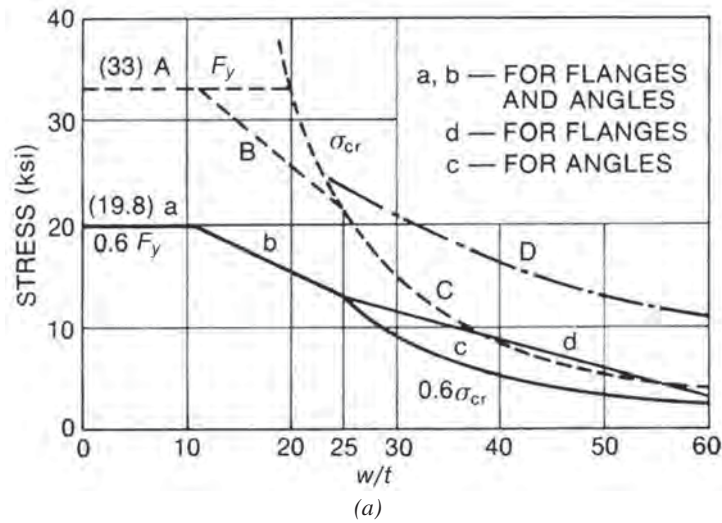
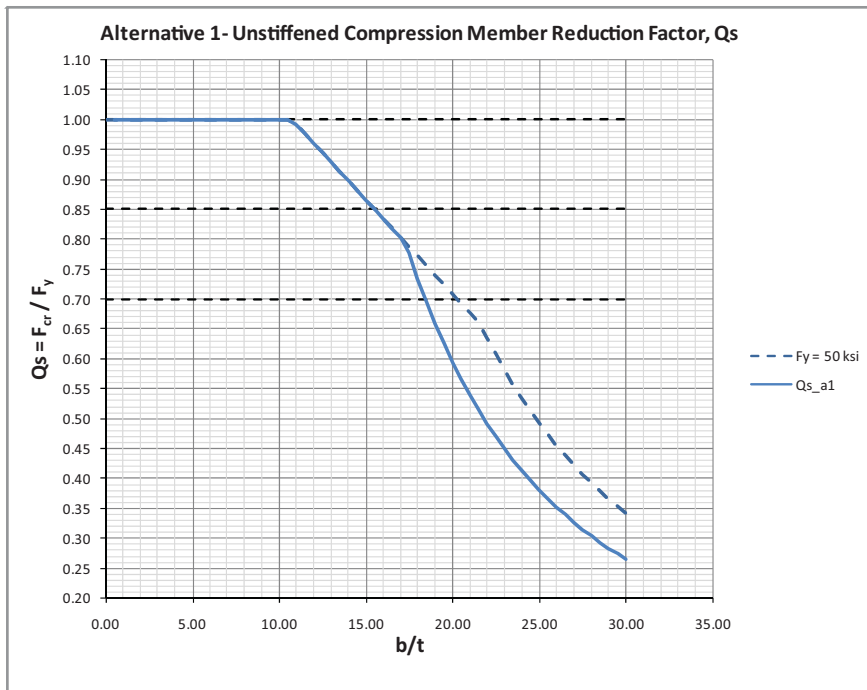


Fig. 5. Q factor according to 1968 AISI and 2010 AISI: (a) permissible design stress for unstiffened compression elements for 33-ksi steel in the 1968 AISI Specification Commentary (Winter, 1970); (b) 2010 AISI Specification definition (dashed line labeled (C) shows plate elastic buckling).

Table 1. Global Comparison of FE Analysis to SJI Nominal Strength Ratios

Global Average of P_{fe}/P_n per SJI Specification							
Axis	Variable	L/1500			L/500		
		50 ksi	65 ksi	80 ksi	50 ksi	65 ksi	80 ksi
	Q Factor						
Strong	0.7	0.855	0.890	0.868	0.782	0.808	0.787
	0.85	1.033	1.034	1.021	0.900	0.916	0.917
	1	1.019	1.011	1.004	0.928	0.930	0.929
Weak	0.7	1.045	1.104	1.095	0.945	1.016	1.021
	0.85	1.186	1.172	1.160	1.066	1.083	1.080
	1	1.136	1.126	1.116	1.062	1.060	1.055
	Number of Spacers						
Strong	1	0.973	0.973	0.958	0.872	0.878	0.873
	2	1.005	1.015	1.005	0.899	0.918	0.915
Weak	1	1.124	1.127	1.116	1.030	1.050	1.043
	2	1.148	1.151	1.142	1.047	1.069	1.072

Mean: Strong	0.989	0.994	0.982	0.886	0.898	0.894
Mean: Weak	1.136	1.139	1.129	1.038	1.060	1.058
Mean: Weak and strong	1.063	1.067	1.055	0.962	0.979	0.976
Grand total	1.061			0.972		



(i) $b/t \leq 0.45 \sqrt{E/F_y}$
 $Q_s = 1.0$

(ii) $0.45 \sqrt{E/F_y} < b/t \leq 0.71 \sqrt{E/F_y}$
 $Q_s = 1.34 - 0.76 \left(\frac{b}{t}\right) \sqrt{\frac{F_y}{E}}$

(iii) $b/t > 0.71 \sqrt{E/F_y}$
 $Q_s = \frac{0.41E}{F_y \left(\frac{b}{t}\right)^2}$

Fig. 6. Proposed Q_{A1} factor Q_s equation versus angle leg-to-thickness ratio for 50-ksi steel (dashed curve shows Q factor per AISC, 2010).

calculated by the 2010 AISC provisions. This can offset the nonconservatism observed in Table 1 for $Q = 0.7$ cases.

3. For elements in the transition region ($1 > Q > 0.8$), Q_{A1} follows the 2010 AISC provisions, while Q_{A2} results in higher Q factor values. This can reduce the consistent slight conservatism in $Q = 0.85$ cases.
4. For elements in the inelastic local buckling region ($Q = 1$), Q_{A1} and Q_{A2} follow the 2010 AISC provisions.

Member Slenderness

The use of the slender cross-section element buckling reduction factor alternatives was investigated with and without the built-up member slenderness modification per the 2010 AISC provisions according to Equations 1 and 2. The built-up member slenderness modification only affects the strong-axis buckling strength. It primarily affects the buckling strength of slender members in the elastic buckling region by increasing their effective slenderness and, therefore, reducing their nominal buckling strengths. (Meanwhile, the modified element slenderness—i.e., modified Q factor—reduces the nominal buckling strength of members with slender elements in the inelastic buckling range.) The companion paper (Webster et al., 2017) demonstrated that the adoption of AISC slenderness modification adequately addresses the observed nonconservatism in analytical-to-nominal buckling strength ratios with increasing member slenderness.

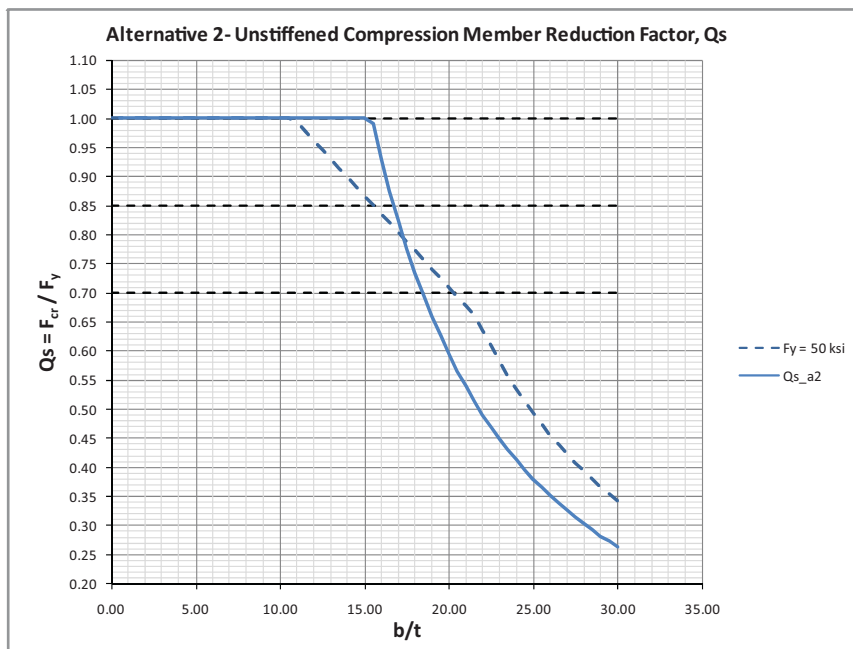
ASSESSMENT OF PROPOSED MODIFICATIONS

Modification of Element Slenderness Q Factor

Table 2 summarizes the ratios of the analytically determined to the calculated buckling strengths using the SJI Specification and modified using the proposed Q factor alternative Q_{A1} . Comparison with Table 1 reveals the following observations:

- The proposed Q factor modifications only affects the results for $Q = 0.7$ cases.
- For $Q = 0.7$, strong-axis buckling, the average ratios for all steel grades is between 0.99 and 1.04 (for code-basis $L/1500$ imperfection magnitude). This reflects a consistent margin of safety when compared to components with higher Q -factor values (the corresponding margins of safety for $Q = 0.85$ and $Q = 1.0$ cases in Table 2 range between 1.00 and 1.03). The overall mean ratios for 50-, 65- and 80-ksi steel grades are 1.03, 1.02 and 1.01, respectively.
- For weak-axis buckling, the average ratios for all steel grades and Q factor combinations are between 1.13 and 1.17, reflecting a consistent margin of safety when compared to angles of higher Q -factor values. The overall mean ratios for all three steel grades are between 1.14 and 1.16.

Table 3 summarizes the ratios of the analytically determined to the calculated buckling strengths using the



$$(i) \quad b/t \leq 0.64 \sqrt{E/F_y}$$

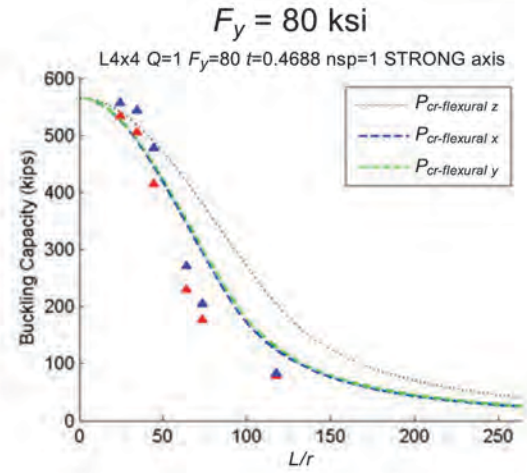
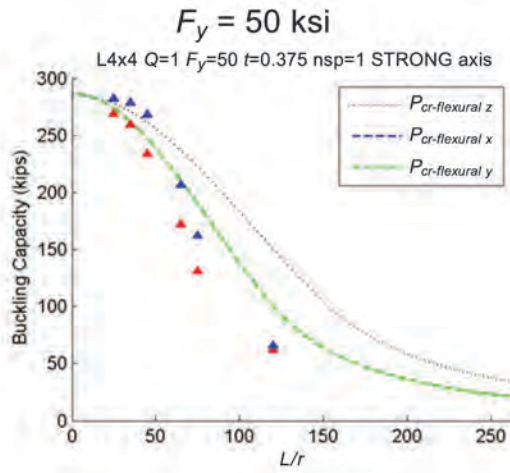
$$Q_s = 1.0$$

$$(ii) \quad b/t > 0.64 \sqrt{E/F_y}$$

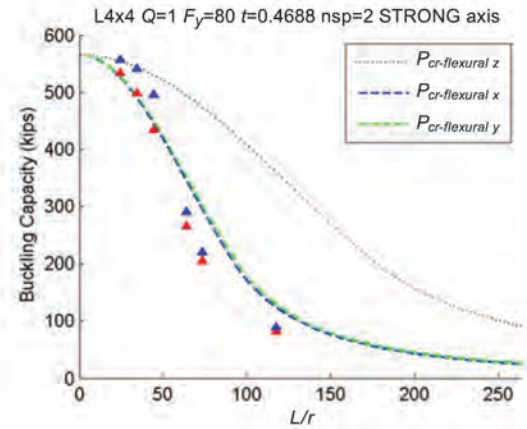
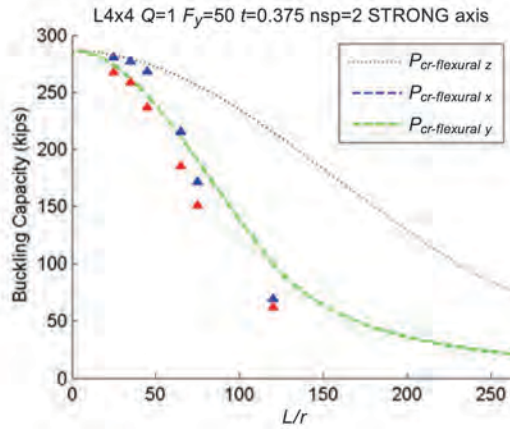
$$Q_s = \frac{0.41E}{F_y \left(\frac{b}{t}\right)^2}$$

Fig. 7. Proposed Q_{A2} factor, Q_s equation versus angle leg-to-thickness ratio for 50-ksi steel (dashed curve shows Q factor per AISC, 2010).

1 spacer



2 spacer



▲ L/1500
▲ L/500

Fig. 8. LL4x4 analytical strong-axis (pinned) buckling strengths compared to the SJI nominal strengths; L/500 and L/1500 imperfection magnitudes; $F_y = 50$ -ksi and 80-ksi materials; $Q = 1.0$.

Table 2. Global Comparison of FE Analysis to Q_{A1} Modified SJI Strength Ratios (compare to Table 1)

Global Average of $(F_{fe}/F_y)/(F_{cr}/F_y \cdot Q_{A1})$							
Axis	Variable	L/1500			L/500		
		50 ksi	65 ksi	80 ksi	50 ksi	65 ksi	80 ksi
	Q Factor						
Strong	0.7	1.044	0.986	0.988	0.958	0.897	0.898
	0.85	1.032	1.034	1.022	0.899	0.916	0.917
	1	1.018	1.012	1.003	0.927	0.930	0.929
Weak	0.7	1.171	1.162	1.164	1.061	1.070	1.088
	0.85	1.185	1.172	1.161	1.065	1.083	1.081
	1	1.135	1.126	1.115	1.062	1.061	1.054
	Number of Spacers						
Strong	1	1.012	0.993	0.983	0.908	0.897	0.896
	2	1.046	1.037	1.032	0.937	0.938	0.939
Weak	1	1.149	1.139	1.130	1.054	1.062	1.057
	2	1.176	1.165	1.157	1.071	1.081	1.086

Mean: Strong	1.029	1.015	1.007	0.923	0.918	0.918
Mean: Weak	1.163	1.152	1.144	1.063	1.072	1.072
Mean: Weak and strong	1.096	1.084	1.075	0.993	0.995	0.995
Grand total	1.085			0.994		

SJI Specification and modified using the proposed Q factor alternative Q_{A2} . Comparison with Tables 1 and 2 reveals the following observations:

- The effect of the QA2 proposal on the $Q = 0.7$ cases is identical to that of the QA1 proposal.
- For $Q = 0.85$, the Q_{A2} proposal results in a reduction in the average ratios of analytical-to-predicted buckling strengths for all steel grades. For strong-axis buckling, this reduction results in nonconservative predictions of the buckling load. For weak-axis buckling, this reduction results in a minor decrease in the margin of safety.
- For strong-axis buckling, the overall mean ratios for all three steel grades are between 0.98 and 1.0, which reflects a nonconservative bias.

Figures 9 through 13 show graphical comparisons of the analytical results to the predictions of the SJI Specification using the 2010 AISC nominal buckling strengths and the buckling strengths modified using the two proposed Q -factor definitions.

Figures 9 and 10 show the results for LL8×8 LL6×6 angles, respectively. These two angle sizes have Q -factor values not lower than 0.8. For angles with relatively low

member slenderness parameters ($\lambda_{cr} < 1$), it is clear that Q_{A2} returns a better fit on average, while Q_{A1} and Q_{SJI} can be seen as a lower bound for design, which maintains a safety margin. For angles with higher member slenderness parameter λ_{cr} , there are cases where the SJI Specification slightly overpredicts the strong-axis buckling strength for all three Q -factor formulations.

Figures 11 and 12 show the results for LL4×4 and LL2×2 angles, respectively. These two angle sizes have Q -factor values as low as 0.67. For specimens with $Q = 0.8$ or higher, the comparison yields similar results to that of LL8×8 and LL6×6 angles (Figures 9 and 10). For angles with lower Q -factor values and relatively low member slenderness parameter ($\lambda_{cr} < 1$), both proposed Q -factor formulations result in predicted buckling strengths that constitute a lower bound of nearly all the analytical results, while the 2010 AISC Q -factor formulation overpredicts the strong-axis analytical strength in all but four of 72 cases. For angles with higher member slenderness parameters λ_{cr} , there are cases where the SJI Specification slightly overpredicts the strong-axis buckling strength for all three Q -factor formulations.

Figure 13 shows that the inclusion of residual stresses in the analytical model to determine the buckling strength produces limited reduction in the analytical strength for

Table 3. Global Comparison of FE Analysis to Q_{A2} Modified SJI Strength Ratios (compare to Table 1)

Global Average of $(F_{fe}/F_y)/(F_{cr}/F_y \cdot Q_{a2})$							
Axis	Variable	L/1500			L/500		
		50 ksi	65 ksi	80 ksi	50 ksi	65 ksi	80 ksi
	Q Factor						
Strong	0.7	1.044	0.986	0.988	0.958	0.897	0.898
	0.85	0.953	0.956	0.951	0.829	0.846	0.853
	1	1.018	1.012	1.003	0.927	0.930	0.929
Weak	0.7	1.171	1.162	1.164	1.061	1.070	1.088
	0.85	1.126	1.118	1.114	1.012	1.033	1.037
	1	1.135	1.126	1.115	1.062	1.061	1.054
	Number of Spacers						
Strong	1	0.981	0.963	0.955	0.882	0.870	0.871
	2	1.015	1.006	1.004	0.909	0.910	0.913
Weak	1	1.127	1.118	1.112	1.034	1.043	1.040
	2	1.152	1.143	1.138	1.051	1.061	1.069

Mean: Strong	0.998	0.984	0.979	0.895	0.890	0.892
Mean: Weak	1.139	1.131	1.125	1.042	1.052	1.054
Mean: Weak and strong	1.069	1.057	1.052	0.969	0.971	0.973
Grand total	1.059			0.971		

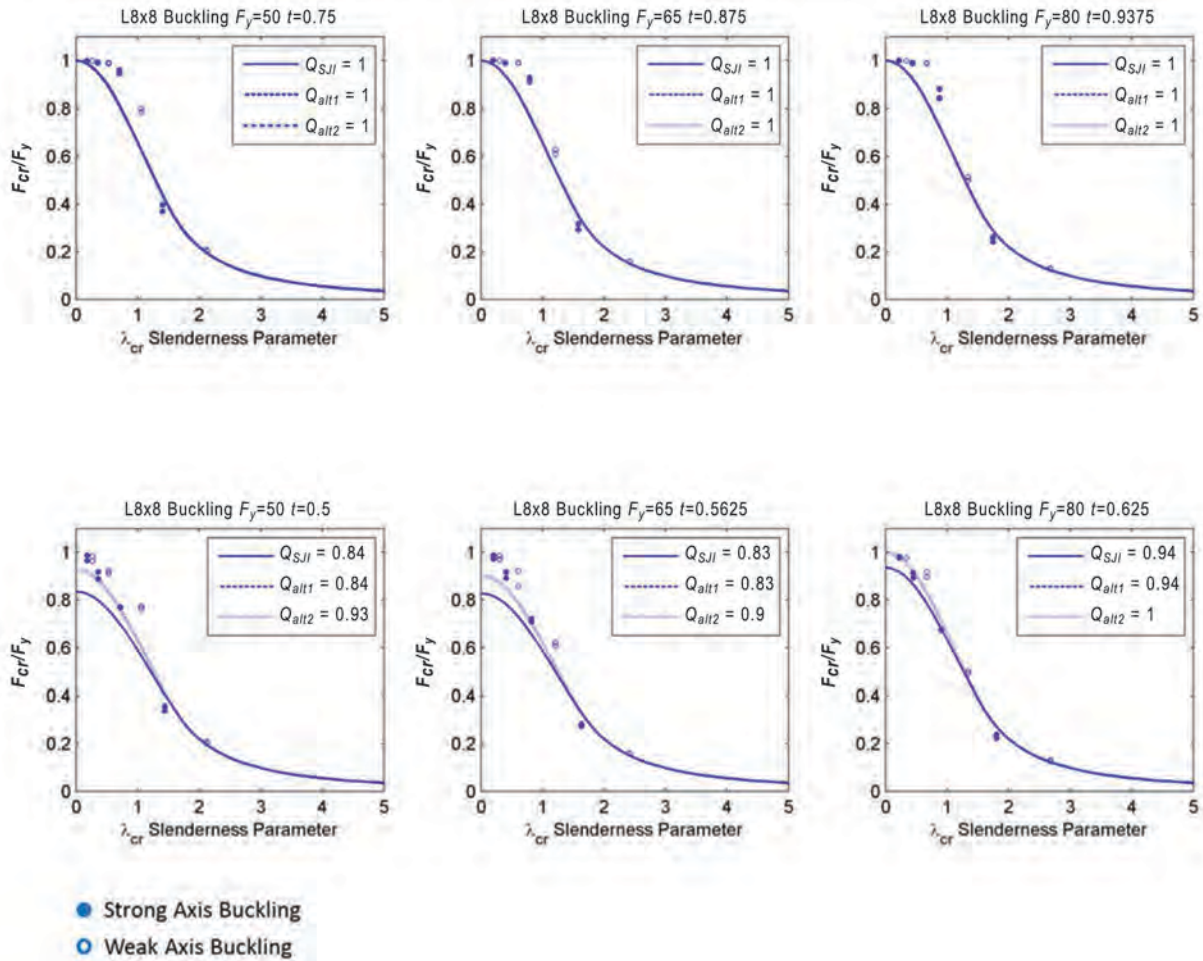


Fig. 9. L8x8 normalized analytical buckling strength (L/1500 imperfection) compared to normalized flexural buckling equations using Q-factor definitions per 2010 AISC Specification, Q_{A1} , and Q_{A2} .

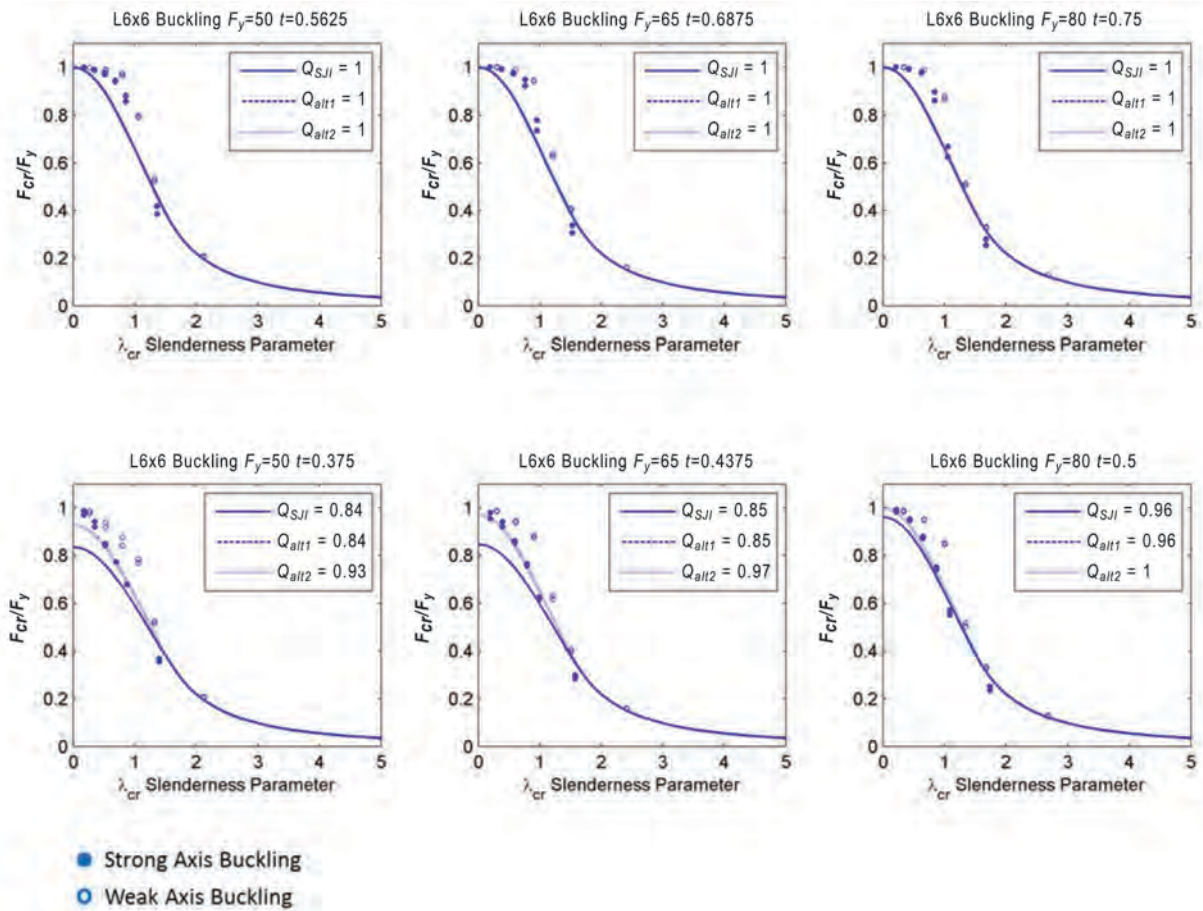


Fig. 10. L6x6 normalized analytical buckling data ($L/1500$ imperfection) compared to normalized flexural buckling equations using Q-factor definitions per 2010 AISC Specification, Q_{A1} , and Q_{A2} .

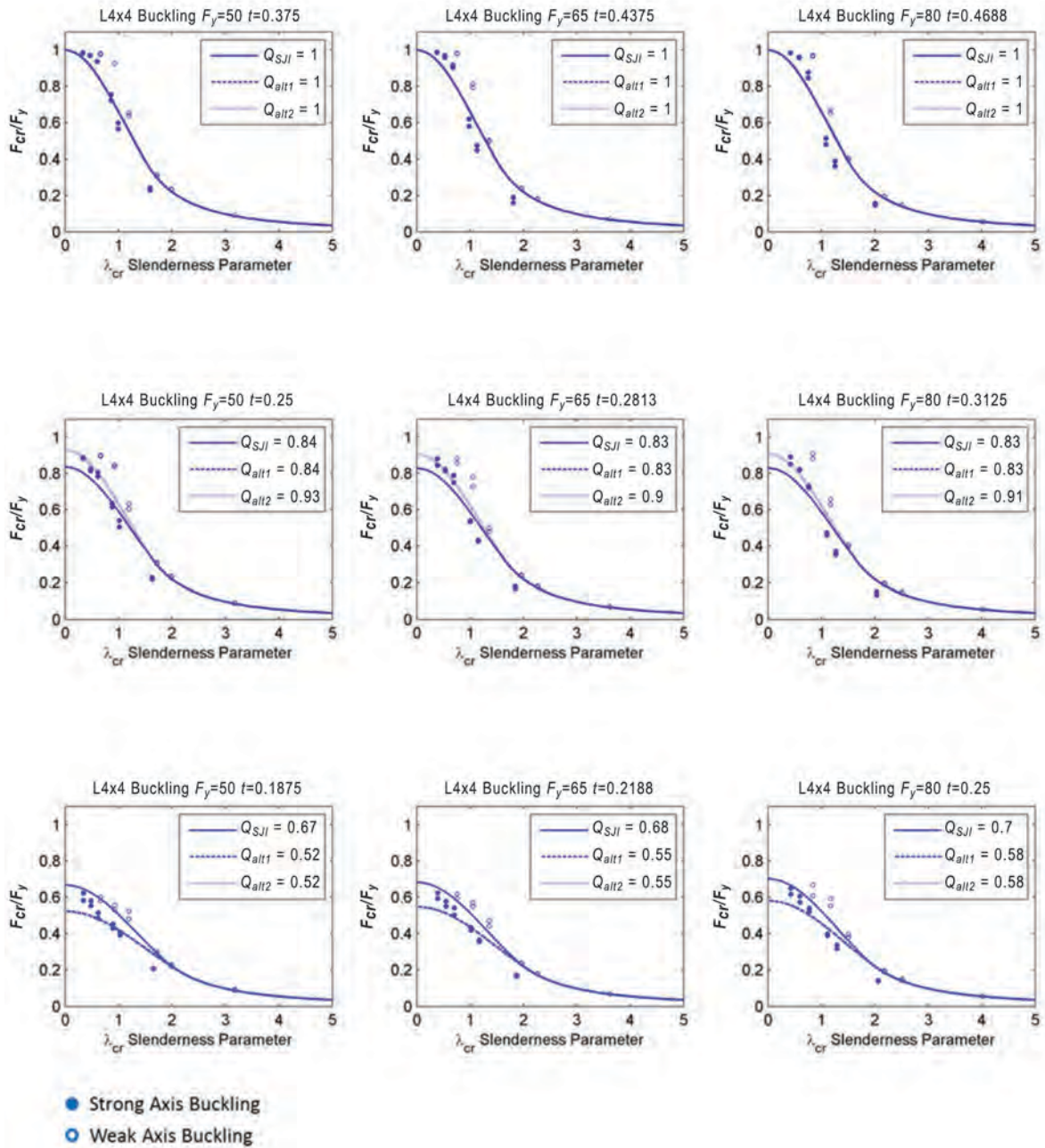


Fig. 11. LL4x4 normalized analytical buckling data ($L/1500$ imperfection) compared to normalized flexural buckling equations using Q-factor definitions per 2010 AISC Specification, Q_{A1} , and Q_{A2} .

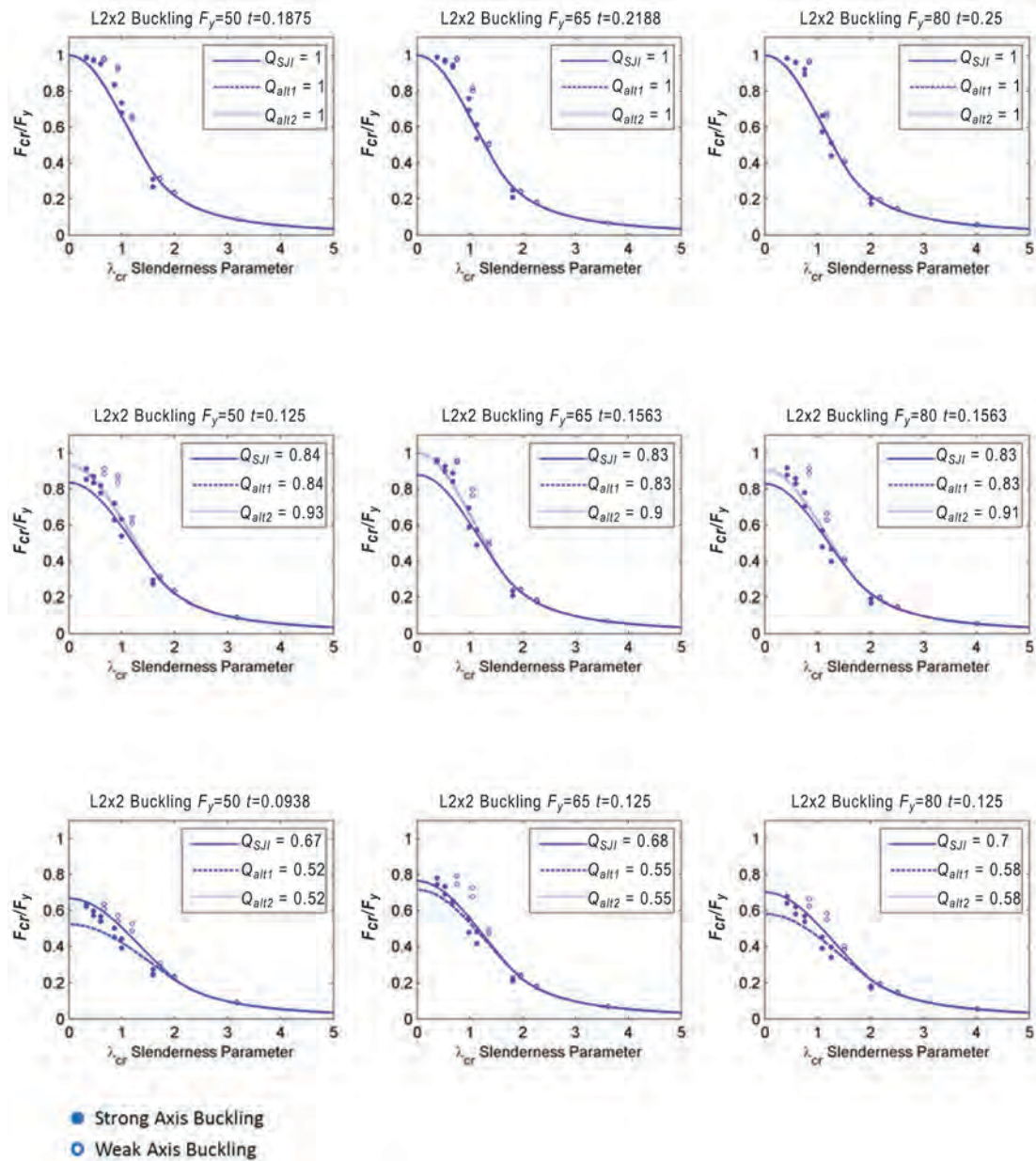


Fig. 12. LL2x2 normalized analytical buckling data ($L/1500$ imperfection) compared to normalized flexural buckling equations using Q-factor definitions per 2010 AISC Specification, Q_{A1} , and Q_{A2} .

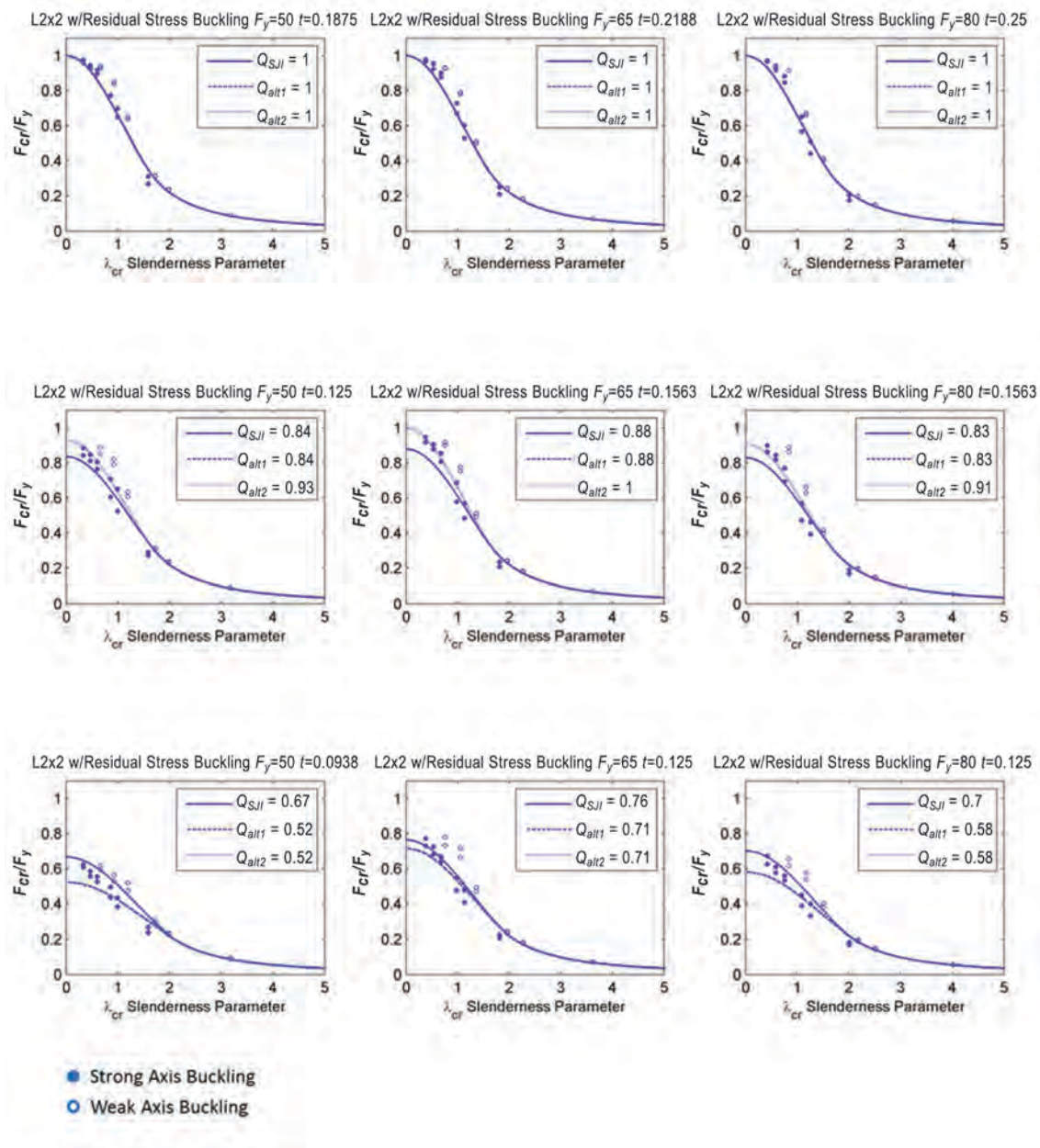


Fig. 13. LL2x2 (with residual stress) normalized analytical buckling data ($L/1500$ imperfection) compared to normalized flexural buckling equations using Q-factor definitions per 2010 AISC Specification, Q_{A1} , and Q_{A2} .

Table 4. Global Comparison of Ratios of FE Analysis to SJI Strength Modified Q_{A1} and AISC Built-Up Member Slenderness Modification (compare to Tables 1 and 2)

Global Average of $(F_{fe}/F_y)/(F_{cr}/F_y_Modified_Q_{A1})$							
Axis	Variable	L/1500			L/500		
		50 ksi	65 ksi	80 ksi	50 ksi	65 ksi	80 ksi
	Q Factor						
Strong	0.7	1.092	1.053	1.064	0.999	0.956	0.965
	0.85	1.090	1.104	1.100	0.949	0.977	0.986
	1	1.087	1.090	1.090	0.989	0.999	1.008
Weak	0.7	1.171	1.162	1.164	1.061	1.070	1.088
	0.85	1.185	1.172	1.161	1.065	1.083	1.081
	1	1.135	1.126	1.115	1.062	1.061	1.054
	Number of Spacers						
Strong	1	1.102	1.101	1.103	0.987	0.992	1.004
	2	1.077	1.074	1.073	0.964	0.971	0.976
Weak	1	1.149	1.139	1.130	1.054	1.062	1.057
	2	1.176	1.165	1.157	1.071	1.081	1.086

Mean: Strong	1.089	1.088	1.088	0.975	0.981	0.990
Mean: Weak	1.163	1.152	1.144	1.063	1.072	1.072
Mean: Weak and strong	1.126	1.120	1.116	1.019	1.026	1.031
Grand total	1.121			1.025		

members with low slenderness parameters λ_{cr} , yet it does not have a significant effect on the relative impact of switching from the 2010 AISC provisions to the proposed Q -factor modifications when compared to Figure 12.

It is clear from the results that the use of the proposed Q -factor modifications eliminates the nonconservatism in the average analytical-to-predicted buckling strength ratios for members with low Q factors ($Q = 0.7$). Alternative Q_{A1} produces consistent average margins of safety for all steel grades and Q -factor values. Alternative Q_{A2} produces non-conservative average ratios for members with intermediate Q factors ($Q = 0.85$). For all three Q -factor formulations, there are a few individual cases with high member slenderness parameters ($\lambda_{cr} \geq 1$) where the predicted buckling strengths are nonconservative.

Inclusion of AISC Built-Up Member Slenderness Modification Provision

Table 4 summarizes the ratios of the analytically determined to the calculated buckling strengths using the SJI Specification with the AISC built-up slenderness modification and the proposed Q -factor alternative Q_{A1} . Comparison

with Table 2 and Table 3 reveals the following observations:

- The proposed Q -factor and built-up slender modifications only affect the results for strong-axis buckling.
- For all Q -factor values and steel grade combinations, the average ratio for strong-axis buckling is between 1.06 and 1.10 (for code-basis L/1500 imperfection magnitude), which reflects a consistent average margin of safety above unity.
- The average ratio for weak-axis buckling is always greater than one. The average margins of safety are nearly consistent between 1.12 and 1.19.
- The overall mean ratios for strong-axis buckling in all three steel grades are about 1.09. The overall mean ratios for weak-axis buckling in all three steel grades are between 1.14 and 1.16. Hence, the design equation leads to similar levels of conservatism for both sets of boundary conditions and corresponding failure modes.
- The individual result plots (not shown) demonstrate a better performance for the calculated buckling strengths at relatively high member slenderness parameters λ_{cr} than

Table 5. Global Comparison of Ratios of FE Analysis to SJI Strength Modified by Q_{A2} and AISC Built-Up Member Slenderness Modification (compare to Tables 1, 3 and 4)

Global Average of $(F_{fe}/F_y)/(F_{cr}/F_y_Modified_Q_{A2})$							
Axis	Variable	L/1500			L/500		
		50 ksi	65 ksi	80 ksi	50 ksi	65 ksi	80 ksi
Q Factor							
Strong	0.7	1.092	1.053	1.064	0.999	0.956	0.965
	0.85	1.013	1.027	1.031	0.881	0.909	0.924
	1	1.087	1.090	1.090	0.989	0.999	1.008
Weak	0.7	1.171	1.162	1.164	1.061	1.070	1.088
	0.85	1.126	1.118	1.114	1.012	1.033	1.037
	1	1.135	1.126	1.115	1.062	1.061	1.054
Number of Spacers							
Strong	1	1.072	1.072	1.077	0.961	0.966	0.980
	2	1.046	1.043	1.046	0.936	0.942	0.951
Weak	1	1.127	1.118	1.112	1.034	1.043	1.040
	2	1.152	1.143	1.138	1.051	1.061	1.069

Mean: Strong	1.059	1.057	1.061	0.949	0.955	0.966
Mean: Weak	1.139	1.131	1.125	1.042	1.052	1.054
Mean: Weak and strong	1.099	1.094	1.093	0.995	1.003	1.010
Grand total	1.095			1.003		

observed in Figures 9 through 13. Fewer cases underpredict the analytically determined buckling strength than shown in Figures 9 through 13.

Table 5 summarizes the ratios of the analytically determined to the calculated buckling strengths using the SJI Specification with the AISC built-up slenderness modification and the proposed Q -factor alternative Q_{A2} . Comparison with Tables 1, 3 and 4 reveals the following observations:

- The effect of Q_{A2} proposal on $Q = 0.7$ cases is identical to that of Q_{A1} proposal. Its effect on cases with relatively high member slenderness parameters, λ_{cr} , is also similar to using alternative Q_{A1} .
- For all combinations of Q -factor values and steel grades, the average ratio for strong-axis buckling is between 1.01 and 1.09 (for code-basis L/1500 imperfection magnitude), which reflects an average margin of safety slightly above 1. However, the average margin of safety for $Q = 0.85$ cases are consistently lower than other cases.
- The overall mean ratios for strong-axis buckling in all three steel grades are about 1.06. The overall mean

ratios for weak-axis buckling in all three steel grades are between 1.13 and 1.14.

The inclusion of the 2010 AISC slenderness modification produces better predictions for members with high slenderness parameter values. At relatively low member slenderness ratios, it introduces moderate conservatism in the strong-axis buckling prediction (within 10% margin on average). For Q_{A1} , the extra conservatism is consistent on average for each steel grade and range of Q factors. The margins of safety for strong- and weak-axis buckling are more aligned than they are using Q_{A2} . For Q_{A2} , the extra conservatism is not consistent, having lower values for $Q = 0.85$ cases than $Q = 0.70$ and $Q = 1.0$ cases for each steel grade.

In summary, the use of the modified Q -factor definitions eliminates the nonconservatism observed with the use of the SJI equations for strong-axis bending in members with low Q -factor values. However, alternative Q_{A1} produces consistent average margins of safety of about unity for all examined combinations of Q -factors and steel grades, while Q_{A2} produces less conservative average predictions for $Q = 0.85$ cases. To achieve a consistent factor of safety across the full range of Q factors, the authors recommend the use of the

cross-section element slenderness factor alternative Q_{A1} . The effect of using the proposed Q -factor modifications only affects cases with low member slenderness parameters.

CONCLUSIONS

In a separate computational parametric study (Webster et al., 2017), the authors showed that the SJI buckling equations are nonconservative in the strong-axis direction for many double-angle configurations, independent of material strength, and that this nonconservatism increases as the Q factor decreases from 1.0 to 0.7 and as the member (global) slenderness ratio increases. The authors demonstrated that the modified slenderness ratio for built-up sections in the 2010 AISC *Specification* significantly improves the accuracy of the SJI nominal buckling strength predictions for strong-axis buckling of members with high slenderness ratios in steel grades ranging from 50 to 80 ksi, yet it does not completely eliminate the nonconservatism for members with low Q -factor values. The authors also found that the 2010 AISC equations for flexural-torsional buckling produced overly conservative results for members with low slenderness ratios.

The present paper investigated the adoption of modified Q -factor definitions for element slenderness, based on the 1968 AISI Specification, to resolve the observed lack of conservatism in strong-axis buckling predictions for members with low Q factors. Two alternative element slenderness definitions, Q_{A1} and Q_{A2} , were proposed.

For both conventional and HSLA-V steels, the use of the modified Q -factor definitions in conjunction with the AISC built-up member slenderness modification eliminated the nonconservatism observed with the use of the SJI equations for strong-axis bending for members with low Q factors. Alternative Q -factor definition Q_{A1} produced consistent average margins of safety of about 1.1 for all examined combinations of Q factors and steel grades, while alternative Q -factor definition Q_{A2} produced lower average margins of safety for $Q = 0.85$ cases compared to $Q = 0.7$ and $Q = 1.0$ cases.

The authors recommend modifying both the AISC and the SJI Specifications to uniformly address double-angle compression members as follows:

- Eliminate the flexural-torsional buckling provisions for double-angle compression members from the AISC *Specification*.
- Add the 2010 AISC modified slenderness ratio provisions for built-up members to the SJI Specifications.
- Replace the existing Q -factor definition with the proposed Q_{A1} definition in both the AISC Specification and the SJI Specification.

REFERENCES

- ABAQUS (2007), *ABAQUS User's Manual*, Version 6.7, Dassault Systemes, RI.
- AISC (2010), *Specification for Structural Steel Buildings*, ANSI/AISC 360, American Institute of Steel Construction, Chicago, IL.
- AISI (2007), *Commentary on North American Specification for the Design of Cold-Formed Steel Structural Members*, AISI S100-C, American Iron and Steel Institute, Washington, DC.
- AISI (1968), *Specifications for the Design of Cold-Formed Steel Structural Members*, American Iron and Steel Institute, Washington, DC.
- Aslani, F. and Goel, S. (1991), "An Analytical Criterion for Buckling Strength of Built-up Compression Members," *Engineering Journal*, AISC, Vol. 28, No. 4.
- Candas, A.B., Sause, R. and Ricles, J.M. (2008), *Experimental Study on Buckling of Vanadium Steel Members with Single- or Double-Angle Cross-Sections*, Report No. 08-07, Lehigh University ATLSS Center, Bethlehem, PA.
- Salmon, C.G. and Johnson, J.E. (1990), *Steel Structures: Design and Behavior*, 3rd Ed., Harper & Row, New York, NY.
- SGH (2011), *Correlation and Sensitivity Study on the Buckling of HSLA-V Steel in Single and Double Angle Members*, Project 047079, Simpson Gumpertz and Heger Inc.
- SGH (2012), *Parameter Study to Assess Modifications to the SJI Design Equations for HSLA-V Steels. Rev.1.*, Project 047079, Simpson Gumpertz and Heger Inc.
- SJI (2010), *Standard Specification for Longspan Steel Joists, LH-Series and Deep Longspan Steel Joists, DLH-Series*, ANSI/SJI-LH/DLH, Steel Joist Institute, Florence, SC.
- SJI (2015), *Standard Specification for K-Series, LH-Series, and DLH-Series Open Web Steel Joists and for Joist Girders*, ANSI/SJI 100, Steel Joist Institute, Florence, SC.
- Webster, M.D., Citipitioglu, A., Mayes, R.L., Talaat, M.M. and Kan, F.W. (2017), "Buckling of Conventional and High-Strength Vanadium Steel Double-Angle Compression Members: Computational Parametric Study," *Engineering Journal*, AISC, Vol. 54, No 4.
- Winter, G. (1970), *Commentary on the 1968 Ed. of the Specification for the Design of Cold-formed Steel Structural Members: Cold-formed Steel Design Manual—Part V*, American Iron and Steel Institute, Washington, DC.
- Yu, W.W. (2010), *Cold-Formed Steel Design*, John Wiley & Sons Inc., Hoboken, NJ.
- XYZ Scientific Applications (n.d.). *TrueGrid*. Livermore, CA: <http://www.truegrid.com>.

The Chevron Effect and Analysis of Chevron Beams— A Paradigm Shift

PATRICK J. FORTNEY and WILLIAM A. THORNTON

ABSTRACT

Beam designers and connection designers have a different standard of care in the analysis of beams in inverted V- and V-type braced frames subjected to lateral loads. When the summation of the vertical components of the brace forces is nonzero, (1) beam designers evaluate required beam shear and moment, treating the unbalanced vertical load as a concentrated force acting at the work point of the braces while ignoring any local effects resulting from the brace connection geometry, and (2) the connection designer evaluates the required beam shear based only on the moment acting at the gusset-to-beam interface(s). Thus, the beam designer considers beam span and work point location, ignoring the local effect of the connection, and the connection designer considers the local effects of the connection while ignoring beam span and the location of the work point.

This paper proposes a new method for evaluating required beam shear and moment that includes consideration of beam span, location of work point, and the local effects of the connection—a method that can be used by both the beam designer and the connection designer. Discussion is also provided to illustrate how this proposed method can be used to evaluate whether or not the local connection effect dominates the global effect. It is shown that the magnitude of the unbalanced vertical load influences the impact of the local connection effects; when the summation of the vertical brace force components is zero or relatively small, the local connection effects dominate the global effect. Conversely, when the unbalanced vertical load is relatively large, the global effects dominate; in this case, including the local connection effects will predict a smaller required beam moment possibly allowing for lighter beams.

Keywords: chevron effect, braced frames, work point, V-type, inverted V-type, unbalanced vertical load.

INTRODUCTION

The presence of the gusset plate in a chevron brace connection imparts increases in beam shear and moment demand not captured by the analysis procedures currently used by beam designers and connection designers. This phenomenon was introduced by Fortney and Thornton (2015), who exposed the issue and made recommendations that beam designers could use to estimate connection geometry in an attempt to capture the chevron effect when sizing the frame beams. However, those recommendations were empirically based—more rules of thumb than approaches based on mechanics.

In this follow-on paper, the authors provide recommendations for an approach that can be used by both beam designers and connections designers; the approach is based on first principles and is given in the form of relatively easy-to-use, closed-form equations.

BRACE CONNECTION FORCE DISTRIBUTION

The force distribution in chevron brace connections where braces frame to the bottom side of the frame beam are derived by Fortney and Thornton (2015). For convenience, those equations are shown in Equations 1 through 10 and are supported with the free-body diagram (FBD) shown in Figure 1. Fortney and Thornton did not provide force distributions for braces framing to the top side of a frame beam. Those equations are given in Equations 11 through 19 and are supported in the FBD shown in Figure 1. Equations 11 through 19 were derived in a similar manner as that shown by Fortney and Thornton relative to bottom side braces.

SIGN CONVENTION

The sign convention used throughout this paper assumes that forces on gusset(s) acting to the right or upward, and clockwise moments acting on gusset(s), are positive.

FORCE AND MOMENT EQUATIONS

When the centroid of the gusset-to-beam interface is not horizontally aligned with the work point (see Figure 1), the parameter Δ can be calculated as

Patrick J. Fortney, Ph.D., P.E., S.E., PEng, Associate Professor, University of Cincinnati, Cincinnati, OH. Email: patrick.fortney@uc.edu (corresponding)

William A. Thornton, Ph.D., P.E., NAE, Cives Engineering Corporation, Roswell, GA. Email: bthornton@cives.com

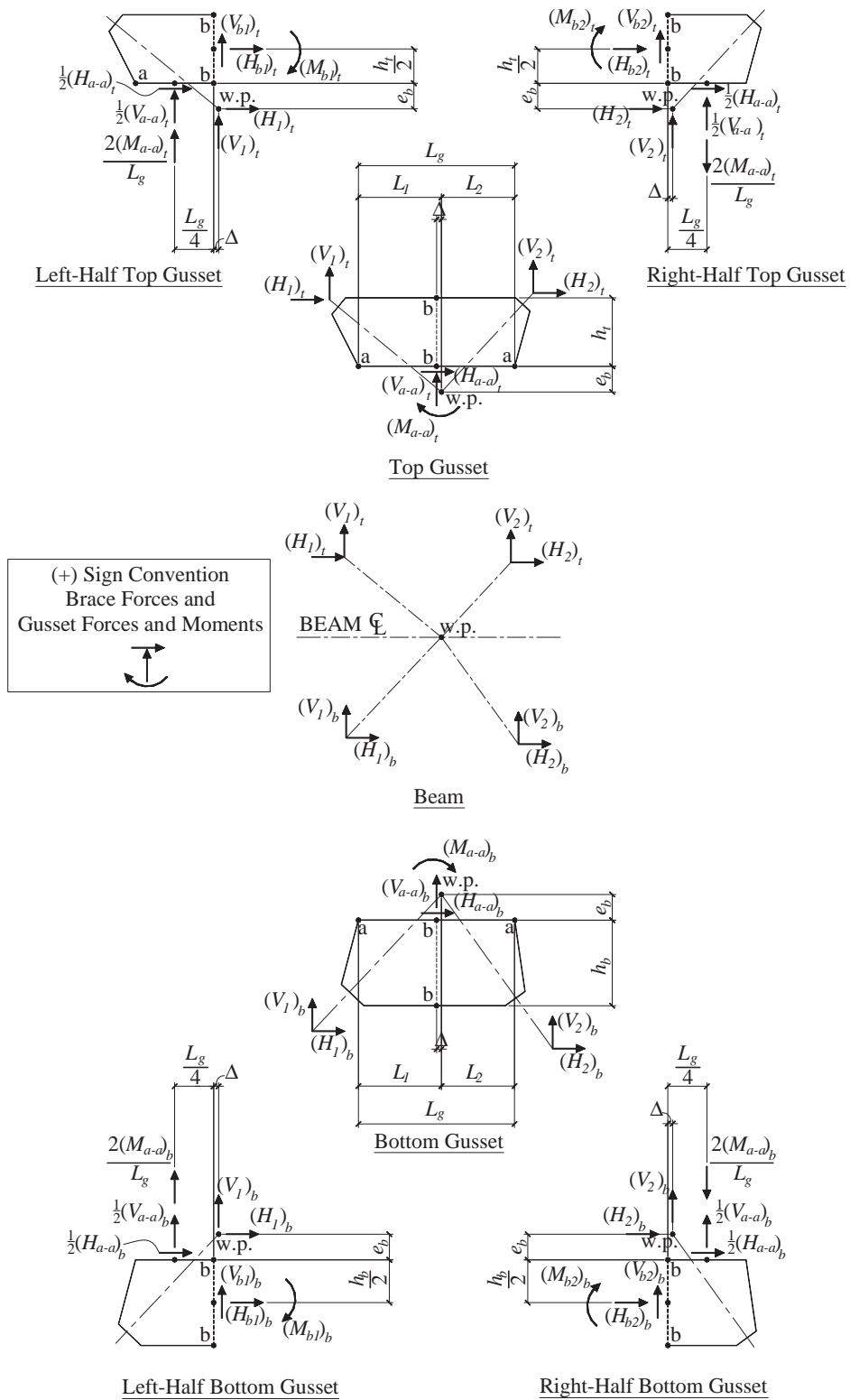


Fig. 1. FBD of force distribution in V-type and inverted V-type brace connections.

$$\Delta = \frac{1}{2}(L_1 - L_2) \quad (1)$$

Bottom Gusset

The forces and moment acting on the bottom gusset at section a-a are

$$(H_{a-a})_b = -(H_1 + H_2)_b \quad (2)$$

$$(V_{a-a})_b = -(V_1 + V_2)_b \quad (3)$$

$$(M_{a-a})_b = (V_1 + V_2)_b \Delta - (H_1 + H_2)_b e_b \quad (4)$$

The forces and moment acting on the bottom gusset at section b-b (left half of gusset) are

$$(H_{b1})_b = \frac{1}{2}(H_1 + H_2)_b - (H_1)_b \quad (5)$$

$$(V_{b1})_b = \frac{1}{2}(V_1 + V_2)_b - \frac{2(M_{a-a})_b}{L_g} - (V_1)_b \quad (6)$$

$$(M_{b1})_b = \frac{L_g}{8}(V_1 + V_2)_b + \frac{h_b}{4}(H_1 + H_2)_b - \frac{(M_{a-a})_b}{2} + \quad (7)$$

$$(V_1)_b \Delta - (H_1)_b \left(e_b + \frac{h_b}{2} \right)$$

The forces and moment acting on the bottom gusset at section b-b (right half of gusset) are

$$(H_{b2})_b = \frac{1}{2}(H_1 + H_2)_b - (H_2)_b \quad (8)$$

$$(V_{b2})_b = \frac{1}{2}(V_1 + V_2)_b + \frac{2(M_{a-a})_b}{L_g} - (V_2)_b \quad (9)$$

$$(M_{b2})_b = -\frac{L_g}{8}(V_1 + V_2)_b + \frac{h_b}{4}(H_1 + H_2)_b - \frac{(M_{a-a})_b}{2} +$$

$$(V_2)_b \Delta - (H_2)_b \left(e_b + \frac{h_b}{2} \right) \quad (10)$$

Note that the equations describing the forces and moment acting on the left half of the gusset on section b-b (Equations 5–7) give forces and moment equal to those forces and moment acting on the right half of the gusset on section b-b (Equations 8–10) but are opposite in sign.

TOP GUSSET

The forces and moments acting on the top gusset at section a-a are

$$(H_{a-a})_t = -(H_1 + H_2)_t \quad (11)$$

$$(V_{a-a})_t = -(V_1 + V_2)_t \quad (12)$$

$$(M_{a-a})_t = (H_1 + H_2)_t e_b + (V_1 + V_2)_t \Delta \quad (13)$$

The forces and moment acting on the top gusset at section b-b (left half of gusset) are

$$(H_{b1})_t = \frac{1}{2}(H_1 + H_2)_t - (H_1)_t \quad (14)$$

$$(V_{b1})_t = \frac{1}{2}(V_1 + V_2)_t - \frac{2(M_{a-a})_t}{L_g} - (V_1)_t \quad (15)$$

$$(M_{b1})_t = \frac{L_g}{8}(V_1 + V_2)_t - \frac{h_t}{4}(H_1 + H_2)_t - \frac{(M_{a-a})_t}{2} + \quad (16)$$

$$(V_1)_t \Delta + (H_1)_t \left(e_b + \frac{h_t}{2} \right)$$

The forces and moment acting on the top gusset at section b-b (right half of gusset) are

$$(H_{b2})_t = \frac{1}{2}(H_1 + H_2)_t - (H_2)_t \quad (17)$$

$$(V_{b2})_t = \frac{1}{2}(V_1 + V_2)_t + \frac{2(M_{a-a})_t}{L_g} - (V_2)_t \quad (18)$$

$$(M_{b2})_t = -\frac{L_g}{8}(V_1 + V_2)_t - \frac{h_t}{4}(H_1 + H_2)_t - \frac{(M_{a-a})_t}{2} + \quad (19)$$

$$(V_2)_t \Delta + (H_2)_t \left(e_b + \frac{h_t}{2} \right)$$

Note that the equations describing the forces and moment acting on the left half of the gusset on section b-b (Equations 14–16) give forces and moment equal to those forces and moment acting on the right half of the gusset on section b-b (Equations 17–19) but are opposite in sign.

THE CHEVRON EFFECT

When the summation of the vertical components of brace forces, $\sum V_i$, sum to zero, a beam analysis assuming a concentrated load acting transversely to the beam and located at the work point (referred to as a Pb/L , Pab/L analysis) will result in the beam having zero shear and zero moment. However, the presence of the brace connection imparts local shear and moment to the beam within the connection region. This local effect is referred to as the chevron effect (Fortney and Thornton, 2015). Under this loading, the beam end reactions and beam shear and moment outside of the connection region are zero. Figure 2 shows representative diagrams for beam shear and moment when $\sum V_i$ sum to zero.

A new proposed analysis method will be discussed in more detail later in this paper. The uniformly distributed loads and moment shown in Figure 2 are a fundamental assumption in that proposed analysis method.

DIVERGENT ANALYSES

The Beam Designer’s Approach

Typically, designers charged with beam analysis and design (beam size selection) will evaluate required beam shear and flexural strength with an analysis that assumes that the $\sum V_i$ is a concentrated load that acts at the work point. Figure 3a shows a representative beam model and resulting beam shear and moment distribution for this loading assumption. This analysis takes into account the span of the beam and the location of the work point along the beam span, but it ignores the local effects of the brace connection, which can be significant as shown previously in Figure 2. Note that the loading in Figure 3a assumes that the brace tension load, P_1 , is larger than the brace compression load, P_2 . The sign of the beam shear and moment is dependent on the relative magnitudes of the brace tension and compression loads.

The Connection Designer’s Approach

Conversely, connection designers will evaluate beam shear based on the moment that acts at the gusset-to-beam interface

and the required beam shear is $2M_{a-a}/L_g$ (the nonzero $\sum V_i$ is ignored altogether). Because the unbalanced vertical force is ignored by connection designers, beam shear and moment as well as beam end reactions are taken as zero. Figure 3b shows a representative beam model and resulting beam shear and moment distribution with this loading assumption. Typically, connection designers do not even evaluate required beam moment. However, to complete this type of analysis, the beam moment associated with this beam shear is $M_{a-a}/2$. With this type of analysis, connection designers consider the local effects of the connection but neglect the beam span and location of the work point and do not wholly consider the unbalanced vertical load. Additionally, because the beam shear is taken as the force couple of the moment, M_{a-a} , beam shear and moment are assumed to exist only within the middle half of the gusset length, L_g .

Comparison of the Two Approaches with the Chevron Effect

Figure 3 compares the divergent analyses performed by beam designers and connection designers. Note that the current standard of care performed by connection designers assumes concentrated forces that are the force couple of the moment, M_{a-a} , and act only within the middle half of the gusset length—unlike the uniformly distributed loads that are assumed when generating the beam shear and moments shown in Figure 2, where the loads are distributed along

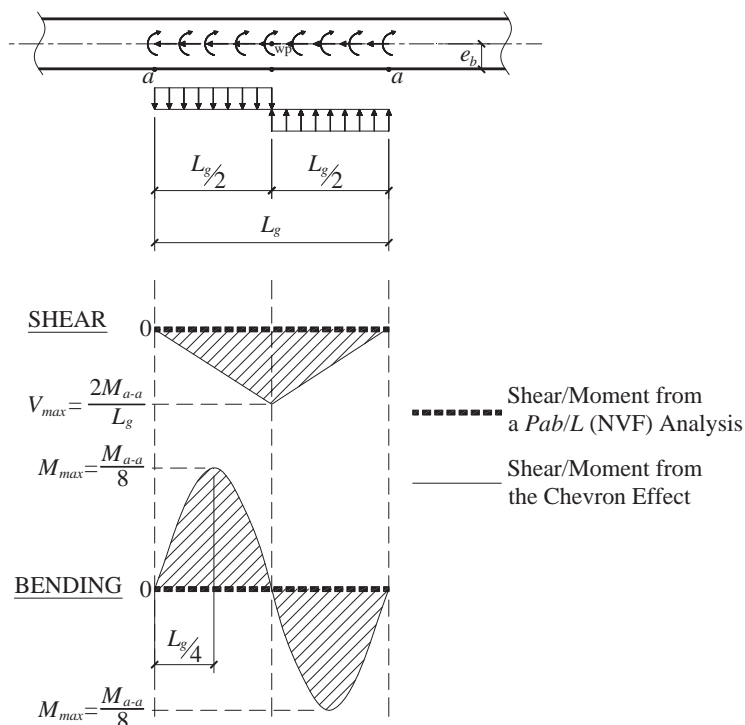
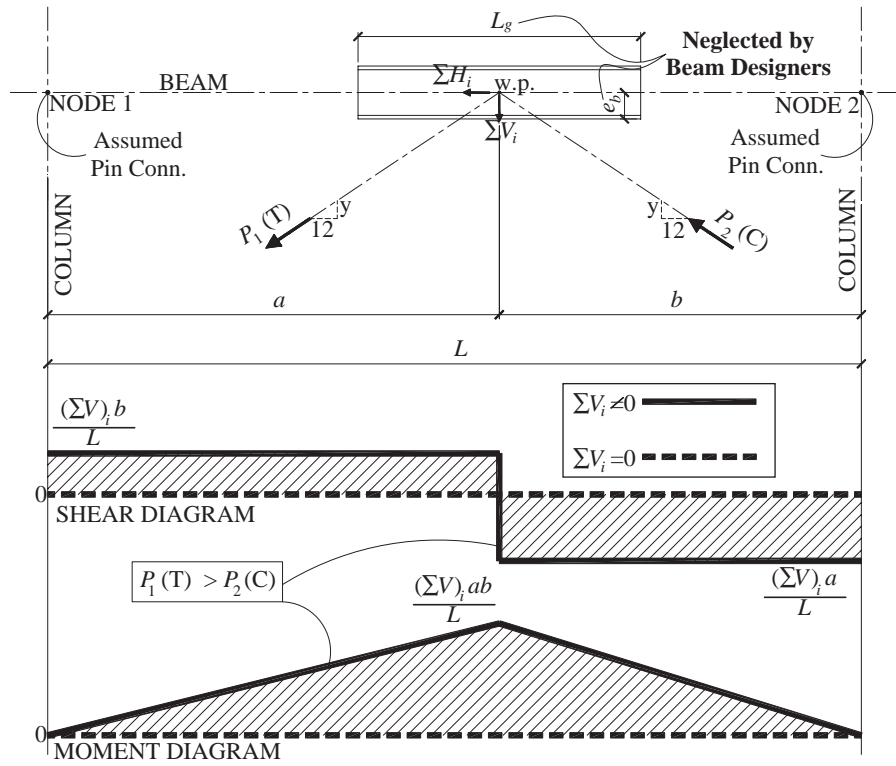
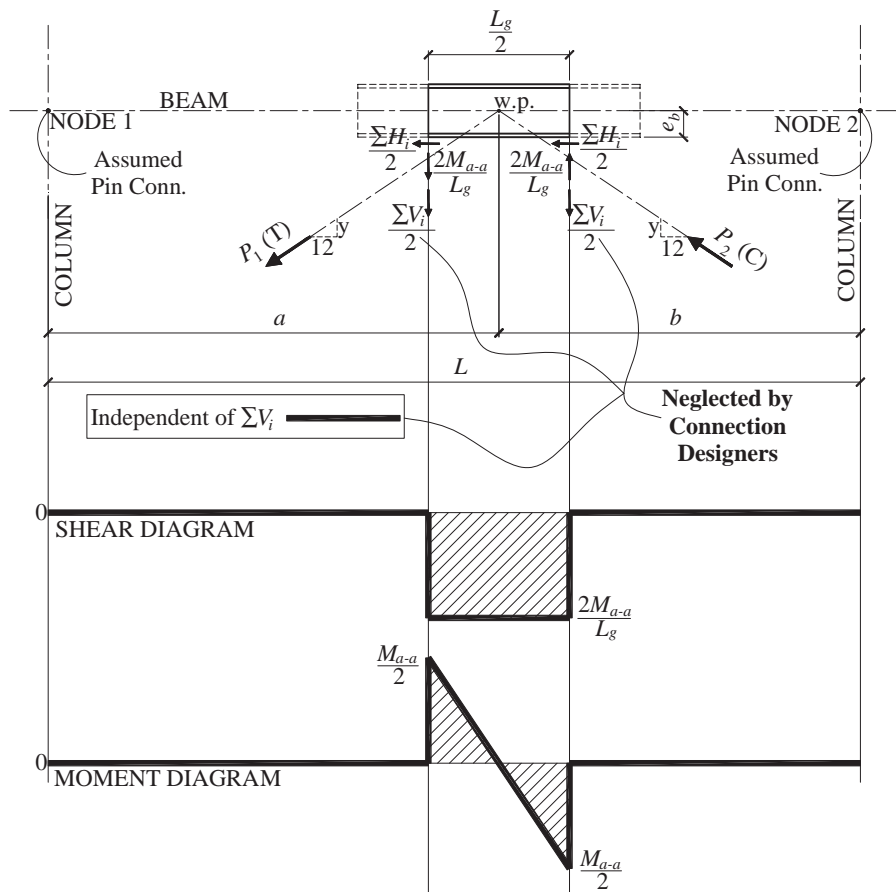


Fig. 2. Representation of the chevron effect; $(\sum V_i) = 0$.



(a) Beam designer analysis; span and work point considered; local effects ignored



(b) Connection designer analysis; span and work point ignored; local effects considered

Fig. 3. Comparison of analysis performed by beam and connection designers. (Note: Δ is assumed to be zero in these figures.)

the entire gusset length. Note that the maximum beam shear is the same for either case. However, the maximum beam moment when assuming uniformly distributed loads as shown in Figure 2 is one-fourth of that when assuming concentrated loads as shown in Figure 3 (recall that beam shear and moment using the current connection designer's approach is independent of the unbalanced vertical load).

As discussed previously, the beam designer's approach neglects the brace connection geometry, thereby neglecting the chevron effect altogether.

As one might expect, the required beam shears and moments determined from the two different procedures (i.e., beam designer versus connection designer) vary drastically. The following discussion attempts to address this issue and propose an analysis procedure that synergizes the analysis performed by beam designers and connection designers such that both individual approaches arrive at the same solution.

SYMBIOTIC ANALYSIS MODEL

The objective for a common method is to develop a procedure that can be used by both beam designers and connection designers, with both arriving at the same required beam shear and moment. The method accounts for beam span, location of work point, and connection geometry. In that there are virtually an infinite number of different possible connection geometries, the method presented here makes the following simplifying assumptions:

- Only lateral load is considered to focus on the issue; in real design, the combination of other applicable loads will need to be carefully considered.
- When braces frame to both the top and bottom flanges,
 - Gusset lengths, L_g , at top and bottom are the same.
 - The vertical edges of the top and bottom gussets are horizontally aligned.

Note that with these two assumptions, the Δ term will be the same for the top and bottom gussets.

- The unbalanced vertical force(s), ΣV_i , is distributed uniformly along the interface(s), L_g .
- The moment(s), M_{a-a} , is distributed uniformly along the interface(s) using a plastic distribution.
- The moment(s) needed to transport the summation of the horizontal forces acting at the interface(s) to the gravity axis of the beam is applied as a uniformly distributed moment, q , over the interface length, L_g .

The Beam Model

The following equations used to evaluate required beam shear and moment are consistent with the sign convention used to derive the equations describing the connection force distributions given in Equations 1 through 19. Refer to the "Sign Convention" section.

The chevron effect does not produce beam end reactions; end reactions are only a function of the unbalanced load, $(\Sigma V)_T$, beam span, L , and location of the work point along the span of the beam, a . Thus, the left beam end reaction, R_1 , shown in Figures 4 and 5 is as given in Equation 20:

$$R_1 = \frac{-(\Sigma V)_T b}{L} \quad (20)$$

where

$$(\Sigma V)_T = (\Sigma V)_t + (\Sigma V)_b \quad (21)$$

In Equation 21, the subscripts t and b represent forces acting on the top and bottom sides of the beam, respectively.

The uniformly distributed loads acting on the beam, w_t and w_b , shown in Figures 4 and 5 are the net transverse loads from both the unbalanced vertical force(s), $(\Sigma V)_T$, and the interface moment(s), M_{a-a} , distributed as a plastic moment

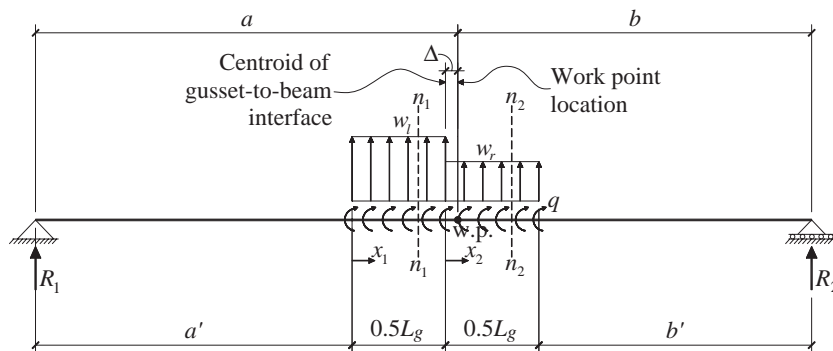


Fig. 4. Beam model; see Fig. 5 for FBDs.

uniformly over the left and right halves of the gussets, respectively, and are calculated as

$$w_l = -\left(\frac{4M_{a-a}}{L_g^2}\right)_t - \left(\frac{4M_{a-a}}{L_g^2}\right)_b + \left(\frac{\sum V}{L_g}\right)_t + \left(\frac{\sum V}{L_g}\right)_b \quad (22)$$

$$w_r = \left(\frac{4M_{a-a}}{L_g^2}\right)_t + \left(\frac{4M_{a-a}}{L_g^2}\right)_b + \left(\frac{\sum V}{L_g}\right)_t + \left(\frac{\sum V}{L_g}\right)_b \quad (23)$$

The third and fourth terms shown in Equations 22 and 23 can be simplified in terms of the total unbalanced vertical force, $(\sum V)_T$, as

$$\left(\frac{\sum V}{L_g}\right)_T = \left(\frac{\sum V}{L_g}\right)_t + \left(\frac{\sum V}{L_g}\right)_b \quad (24)$$

The uniformly distributed moment, q , shown in Figures 4 and 5, is the sum of the horizontal loads acting at the gusset-to-beam interface(s) multiplied by one-half the depth of the beam, e_b , and divided by the gusset length L_g , and is given in Equation 25:

$$q = \left[(\sum H)_t - (\sum H)_b \right] \left(\frac{e_b}{L_g} \right) \quad (25)$$

Maximum Beam Shear and Moment in the Left Half of the Gusset

When the magnitude of the tension brace force is larger than the magnitude of the compression brace force and the left brace and right braces are in tension and compression, respectively, the direction of the distributed moment, q , will be positive (clockwise). Under this type of loading, the maximum beam moment will occur somewhere between the left edge of the gusset(s) and mid-length of the gusset(s), $L_g/2$. The FBD shown in Figure 5a can be used to write equations that describe the distribution of beam shear and moment along the span of the beam.

The moment distribution, $M(x_1)$, is

$$M(x_1) = R_1 a' + R_1 x_1 + 0.5 w_l x_1^2 + q x_1 \quad (26)$$

To locate where the maximum moment occurs, the derivative of Equation 26 is taken and set equal to zero:

$$\frac{d}{dx_1} M(x_1) = 0 = R_1 + w_l x_1 + q \quad (27)$$

Solving Equation 27 for x_1 , the maximum moment occurs a distance from the left edge of the gusset at

$$x_1 = \frac{-R_1 - q}{w_l} \quad (28)$$

where x_1 is valid for a range of

$$0 \leq x_1 \leq \frac{L_g}{2} \quad (29)$$

Substituting Equation 28 into Equation 26 gives the equation for maximum beam moment:

$$M_{\max} = \underbrace{\frac{R_1 a'}{Pab/L} + (R_1 + q)}_{\text{Effect of Gusset}} \left(\frac{-R_1 - q}{w_l} \right) + 0.5 w_l \left(\frac{-R_1 - q}{w_l} \right)^2 \quad (30)$$

To ensure that Equation 30 gives maximum and not minimum moment, the second derivative of Equation 26 is taken. The second derivative is

$$\frac{d^2}{dx_1^2} M(x_1) = w_l \quad (31)$$

When w_l is negative (acting downward), Equation 30 gives a maximum moment in the x_1 region when the moment is positive and gives a minimum moment when the moment is negative. When w_l is positive (acting upward), Equation 30 gives a minimum moment in the x_1 region when the moment is positive and a maximum moment when the moment is

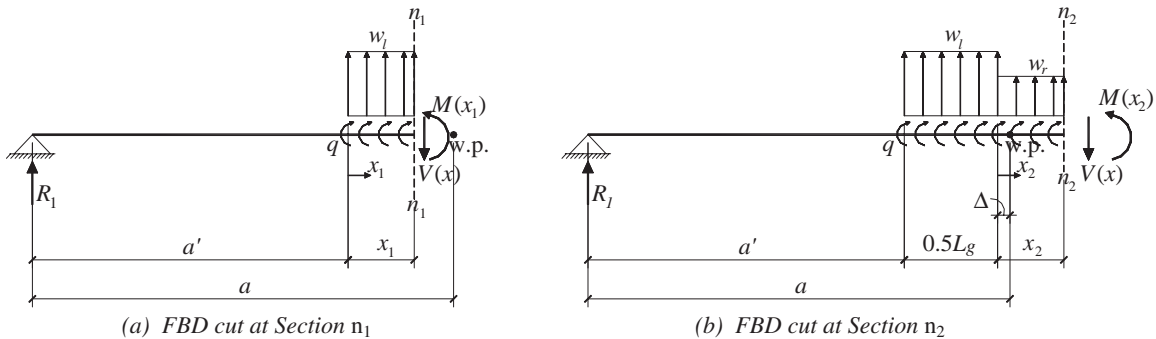


Fig. 5. FBDs used to write beam shear and moment equations; see Fig. 4 for beam model.

negative. In either case, it is best to check the x_2 region (see Figure 5b) and compare the results to determine the overall maximum moment as the maximum beam moment may occur in the beam along the region of the right half of the gusset(s). The equations for the x_2 region (right half of gusset) are presented in the next section of this paper.

The beam shear is distributed over the span of the beam, $V(x_1)$, as given by Equation 32:

$$V(x_1) = \underbrace{R_1}_{\substack{Pb/L \\ \text{Analysis}}} + \underbrace{w_l x_1}_{\text{Effect of Gusset}} \quad (32)$$

In most cases, the maximum beam shear occurs at mid-length of the gusset, $L_g/2$. In rare cases, the net uniformly distributed loads, w_l and w_r , can be the same sign (i.e., both acting downward or both acting upward). In these rare cases, the magnitude of the uniformly distributed plastic moment is smaller than the magnitude of the uniformly distributed unbalanced vertical load. So for most cases, when the magnitude of the plastic moment distribution exceeds the magnitude of the uniformly distributed unbalanced vertical load, the maximum shear can be calculated by substituting $L_g/2$ for the x_1 :

$$V_{max} = R_1 + 0.5w_l L_g \quad (33)$$

Maximum Shear and Moment in Right Half of Gusset

When the magnitude of the tension brace force is larger than the magnitude of the compression brace force and the left brace and right braces are in compression and tension, respectively, the direction of the distributed moment, q , will be negative (counterclockwise). Under this type of loading, the maximum beam moment will occur somewhere between the mid-length of the gusset(s), $L_g/2$ and the right edge of the gusset(s). The FBD shown in Figure 5b can be used to write equations that describe the distribution of beam shear and moment along the span of the beam.

The moment distribution, $M(x_2)$, is

$$M(x_2) = 0.5w_r x_2^2 + (R_1 + 0.5w_l L_g + q)x_2 + R_1(a' + 0.5L_g) + 0.125w_l L_g^2 + 0.5qL_g \quad (34)$$

To locate where the maximum moment occurs, the derivative of Equation 34 is taken and set equal to zero:

$$\frac{d}{dx_2} M(x_2) = 0 = R_1 + 0.5w_l L_g + q + w_r x_2 \quad (35)$$

Solving Equation 35 for x_2 , the maximum moment occurs a distance from the mid-length of the gusset at

$$x_2 = -\frac{R_1 + 0.5w_l L_g + q}{w_r} \quad (36)$$

where x_2 is valid for a range of

$$0 \leq x_2 \leq \frac{L_g}{2} \quad (37)$$

Substituting Equation 36 into Equation 34 gives the equation for maximum beam moment:

$$M(x_2) = 0.5w_r \left(-\frac{R_1 + 0.5w_l L_g + q}{w_r} \right)^2 + (R_1 + 0.5w_l L_g + q) \left(-\frac{R_1 + 0.5w_l L_g + q}{w_r} \right) + R_1(a' + 0.5L_g) + 0.125w_l L_g^2 + 0.5qL_g \quad (38)$$

To ensure that Equation 38 gives maximum moment, and not minimum moment, the second derivate of Equation 34 is taken. The second derivative is

$$\frac{d^2}{dx_2^2} M(x_2) = w_r \quad (39)$$

When w_r is negative (acting downward), Equation 38 gives a maximum moment in the x_2 region when the moment is positive and a minimum moment when the moment is negative. When w_r is positive (acting upward), Equation 38 gives a minimum moment when the moment is positive and a maximum moment when the moment is negative. As stated previously, it is good practice to evaluate moments in both the x_1 and x_2 regions to determine the overall maximum moment.

The beam shear is distributed over the span of the beam, $V(x_2)$, as given by Equation 40:

$$V(x_2) = \underbrace{R_1}_{\substack{Pb/L \\ \text{Analysis}}} + \underbrace{0.5w_l L_g + w_r x_2}_{\text{Effect of Gusset}} \quad (40)$$

In most cases, the maximum beam shear occurs at mid-length of the gusset, $L_g/2$. In rare cases, the net uniformly distributed loads, w_1 and w_2 , can be the same sign (i.e., either both acting downward or both acting upward). In these rare cases, the magnitude of the uniformly distributed plastic moment is smaller than the magnitude of the uniformly distributed unbalanced vertical load. And for the majority of cases, when the magnitude of the plastic moment distribution exceeds the magnitude of the uniformly distributed unbalanced vertical load, the maximum shear can be calculated by substituting $x_2 = 0$ for x_2 . Note that this gives the same maximum shear as given in Equation 33:

$$V_{max} = R_1 + 0.5w_l L_g \quad (41)$$

Rule of Thumb for Connection Geometry

In order for the beam designer to use the proposed equations, the length of the gusset, L_g , and the depth of the beam, $2e_b$, would need to be known. Typically, the brace connection geometry is not known by the beam designer at the time the beam size is selected. Fortney and Thornton (2015)

recommend an approximated gusset length, $L_{g,app}$, equal to

$$L_{g,app} = \frac{L}{6} \quad (42)$$

and an approximated half beam depth, $e_{b,app}$, in in., equal to

$$e_{b,app} = 0.375 \text{ (span of beam in feet)} \quad (43)$$

EVALUATING THE CHEVRON EFFECT

Does the Chevron Effect Dominate?

There are many ways the chevron effect can be evaluated. Two methods are presented here:

1. For a given condition (i.e., the beam span, work point location, and unbalanced vertical force are known), an equivalent gusset length is calculated and compared to the provided gusset length to determine if the chevron effect will dominate—a method that will be useful to the connection designer.
2. For a known beam span, L , an approximated gusset length, $L_{g,app}$, and an approximated half beam depth, $e_{b,app}$, an equivalent unbalanced vertical force can be calculated and compared to the actual unbalanced vertical force to determine if the chevron effect will dominate—a method that will be useful to beam designers.

The equations shown for the following two methods assume that the maximum beam moment occurs in the left half of the gusset. For a specific case where the maximum beam moment occurs in the right half of the gusset, the equations presented can be used by reversing the brace loads.

Comparison of Gusset Lengths, L_g

Figure 6 shows representative beam shear and moment diagrams that consider the local effect as well as the unbalanced vertical loads (brace loads). The maximum moment occurs somewhere between the left edge and the middle of the gusset at a distance, x , from the left edge of the gusset. The change in moment, ΔM_{local} , considering the local effects is

$$\Delta M_{local} = 0.5w_l x^2 + (R_1 + q)x \quad (44)$$

where R_1 is given in Equation 20, w_l is given by Equation 22, and q is given in Equation 25.

Figure 6b shows representative beam shear and moment diagrams that consider only the unbalanced vertical load effect (brace loads). The maximum moment, $M_{max,unbal}$, occurs at the mid-point, which, for this discussion, is considered to be located at mid-length of the gusset (i.e., at $L_g/2$ from the left edge of the gusset). Thus, the change in moment, ΔM_{unbal} , from the left edge of the gusset to mid-length of the gusset is

$$\Delta M_{unbal} = R_1(0.5L_g + \Delta) \quad (45)$$

Equations can be written that will allow one to determine, rather easily, whether or not the chevron effect produces a beam moment larger than what would be calculated considering only the unbalanced vertical loads. It's important to recognize the local connection effects produce no beam end reactions. Thus, the beam end reactions R_1 and R_2 are a function of only the unbalanced vertical load (ΣV_i). By setting Equations 44 and 45 equal, one could calculate an equivalent gusset length, $L_{g,eq}$, that would produce the same beam moment change, ΔM , using either Equation 44 or 45. If the actual gusset length, L_g , is larger than $L_{g,eq}$, the beam moment using the symbiotic method will be smaller than what would be calculated using the connection designer's current method (i.e., if the connection designer even checked beam moment).

Setting Equations 44 and 45 equal, and setting L_g equal to $L_{g,eq}$,

$$\begin{aligned} \Delta M_{local} = 0.5w_l x^2 + (R_1 + q)x &= \Delta M_{unbal} = R_1(0.5L_g + \Delta) \\ 0.5w_l x^2 + (R_1 + q)x &= R_1(0.5L_{g,eq} + \Delta) \end{aligned} \quad (46)$$

Substituting Equation 28, which is in terms of x_1 , for x into Equation 46 and solving for $L_{g,eq}$ gives a quadratic equation. It's important to recognize that the terms w_l and q are also a function of L_g and that when Δ is nonzero, $q = [(M_{a-a})_T - (\Sigma V)_T \Delta] / L_g$.

When Δ is nonzero, the quadratic equation is the closed-form equation shown in Equation 47. In Equation 47, the square root of the discriminant, η , is given as a separate calculation for simplification. When using this equation, the negative value of the square root of the discriminant is used.

$$L_{g,eq} = \frac{M_T \left(\frac{b}{L} \right) - \eta}{(\Sigma V)_T \left[\frac{b}{L} - \left(\frac{b}{L} \right)^2 \right]} \quad (47a)$$

$$\eta = \sqrt{(\Sigma V)_T^2 \Delta^2 \left[\frac{b}{L} - \left(\frac{b}{L} \right)^2 \right] + (\Sigma V)_T M_T \Delta \left[-8 \left(\frac{b}{L} \right)^3 + 10 \left(\frac{b}{L} \right)^2 - 2 \left(\frac{b}{L} \right) \right] + M_T^2 \left(\frac{b}{L} \right)} \quad (47b)$$

In Equation 47, the term M_T is the total moment acting on the upper and lower gussets calculated using Equations 4 and 13 $[(M_{a-a})_l$ and $(M_{a-a})_b$, respectively].

When Δ is equal to zero, the quadratic shown in Equation 47 reduces to the closed-form equation shown in Equation 48:

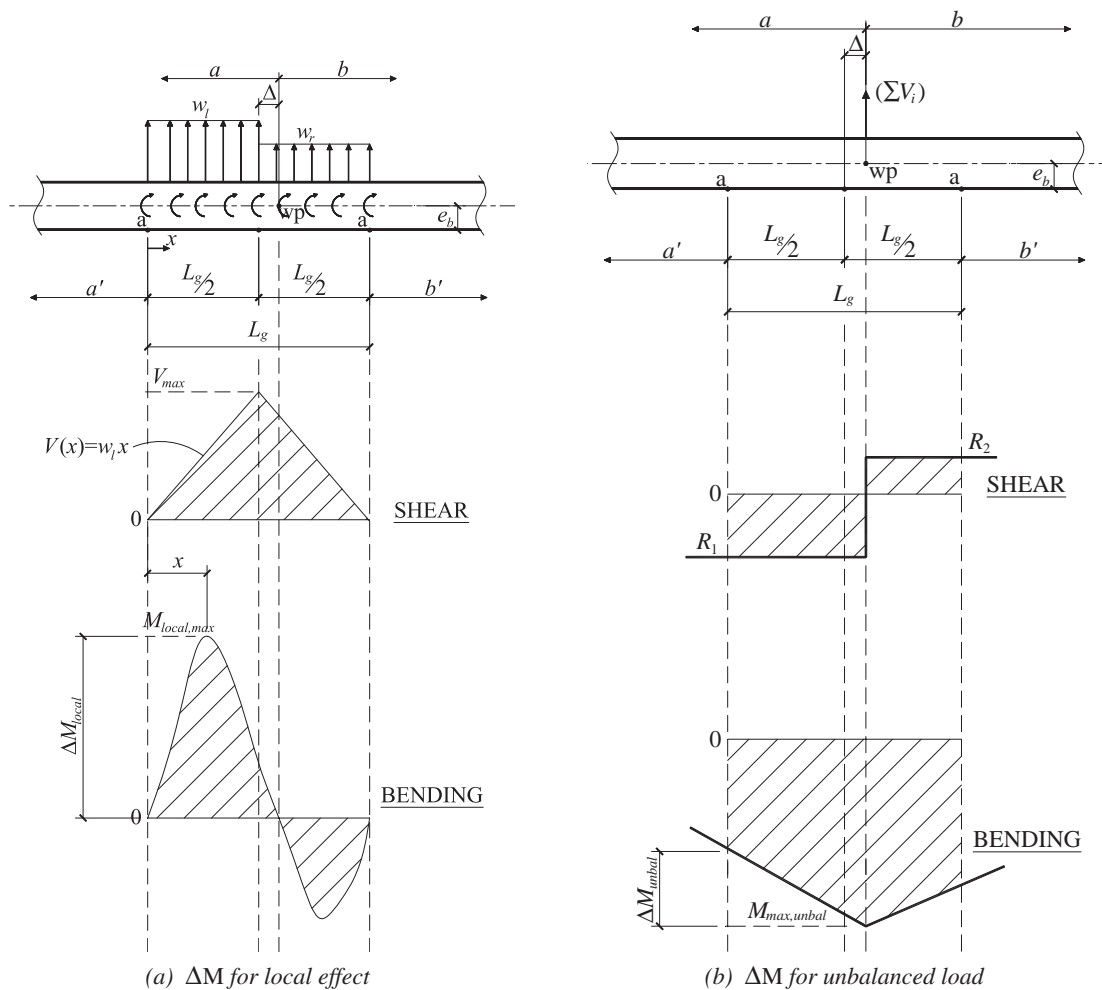


Fig. 6. Change in beam moment from edge of gusset to maximum moment.

$$L_{g,eq} = \frac{M_T}{(\Sigma V)_T} \left[\frac{\frac{b}{L} - \sqrt{\frac{b}{L}}}{\frac{b}{L} - \left(\frac{b}{L}\right)^2} \right] \quad (48)$$

- When L_g is smaller than $L_{g,eq}$, then an analysis that includes the chevron effect will result in a moment that is larger than the moment calculated neglecting the chevron effect (Pab/L is unconservative for bending).
- When L_g is larger than $L_{g,eq}$, then an analysis that includes the chevron effect will result in a moment that is smaller than the moment calculated neglecting the chevron effect (Pab/L is conservative for bending).

Comparison of Unbalanced Vertical Forces

The maximum beam moment using the symbiotic method given by Equation 26 can be set equal to the maximum moment calculated using the current beam designer's, which is Pab/L and is equal to the left beam end reaction, R_1 multiplied by the distance from the left beam end to the location of the work point, a (R_1a). By setting these two equations equal to each other, an equivalent unbalanced vertical force, $(\Sigma V)_T$, can be determined, thereby identifying a magnitude of unbalanced vertical force for which both equations will give the same maximum moment. Setting Equation 26 equal to R_1a gives

$$R_1a' + R_1x_1 + 0.5w_lx_1^2 + qx_1 = R_1a \quad (49)$$

The left beam end reaction, R_1 , in terms of the unbalanced vertical force, $(\Sigma V)_T$, is given by Equation 20. Equation 28 provides a relationship between x_1 and R_1 , and Equation 22 gives a relationship for w_l with the unbalanced vertical force, $(\Sigma V)_T$. The equation for w_l is also a function of the interface moments, $(M_{a-a})_l$ and $(M_{a-a})_b$. Given these relationships, some tedious substitutions, and taking $(\Sigma V)_T$ to be equal to an equivalent unbalanced vertical force for which both equations produce the same moment, $(\Sigma V)_{T,eq}$, gives the following equation:

$$(\Sigma V)_{T,eq} = \frac{q \left[\frac{b}{L} + \frac{4\Delta}{L_g} \left(\frac{b}{L} \right) \right] \pm q \sqrt{\left(\frac{b}{L} \right)^2 \left(\frac{8\Delta}{L_g} + \frac{16\Delta^2}{L_g^2} \right) + \left(\frac{b}{L} \right) \left(1 - \frac{2\Delta}{L_g} - \frac{8\Delta^2}{L_g^2} \right)}}{\left(\frac{b}{L} \right) \left(1 - \frac{2\Delta}{L_g} - \frac{8\Delta^2}{L_g^2} \right) - \left(\frac{b}{L} \right)^2} \quad (50)$$

Equation 50 reduces to a simpler form when the eccentricity, Δ , is equal to zero, as shown in Equation 51.

The roots of Equations 50 and 51 of interest for this application are the negative roots. Therefore, if the eccentricity, Δ , is non-zero, the equivalent unbalanced vertical force, $(\Sigma V)_{T,eq}$, is given by Equation 52:

$$(\Sigma V)_{T,eq} = q \left[\frac{\frac{b}{L} \pm \sqrt{\frac{b}{L}}}{\frac{b}{L} - \left(\frac{b}{L} \right)^2} \right] \quad (51)$$

$$(\Sigma V)_{T,eq} = \frac{q \left[\frac{b}{L} + \frac{4\Delta}{L_g} \left(\frac{b}{L} \right) \right] - q \sqrt{\left(\frac{b}{L} \right)^2 \left(\frac{8\Delta}{L_g} + \frac{16\Delta^2}{L_g^2} \right) + \left(\frac{b}{L} \right) \left(1 - \frac{2\Delta}{L_g} - \frac{8\Delta^2}{L_g^2} \right)}}{\left(\frac{b}{L} \right) \left(1 - \frac{2\Delta}{L_g} - \frac{8\Delta^2}{L_g^2} \right) - \left(\frac{b}{L} \right)^2} \quad (52)$$

If the eccentricity, Δ , is zero, the equivalent unbalanced vertical force, $(\Sigma V)_{T,eq}$, is given by Equation 53:

$$(\Sigma V)_{T,eq} = q \left[\frac{\frac{b}{L} - \sqrt{\frac{b}{L}}}{\frac{b}{L} - \left(\frac{b}{L} \right)^2} \right] \quad (53)$$

A few comments regarding the use of Equations 52 and 53:

- The signs of the quantities $(\Sigma V)_{T,eq}$ and $(\Sigma V)_T$ will be the same. For example, if the actual total unbalanced vertical force, $(\Sigma V)_T$, is negative, the quantity calculated from Equation 52 (or 53), $(\Sigma V)_{T,eq}$, will also be negative, and vice versa.
- When the absolute value of $(\Sigma V)_{T,eq}$ is smaller than the absolute value of $(\Sigma V)_T$, then an analysis that includes the chevron effect will result in a moment that is smaller than the moment calculated neglecting the chevron effect (Pab/L is conservative for bending).
- When the absolute value of $(\Sigma V)_{T,eq}$ is larger than the absolute value of $(\Sigma V)_T$, then an analysis that includes the chevron effect will result in a moment that is larger than the moment calculated neglecting the chevron effect (Pab/L is unconservative for bending).

Note that every term in Equations 52 and 53 is a function of the position of the work point along the span of the beam, b/L . Although it may be counterintuitive to some, Equations 52 and 53 show that the position of the work point along the span of the beam has an effect on whether or not the chevron effect will dominate maximum beam moment.

Possible Beam Shear Diagrams

Unlike beam moment, the local effects of the connection will almost always give a beam shear in excess of the beam shear determined by assuming the unbalanced vertical load acts as a concentrated load at the work point. Figure 7a shows a representative beam shear diagram of this case. However, there are rare instances when the net transverse loads on the beam, w_l and w_r , act in the same direction. This occurs when the magnitude of the uniformly distributed plastic moment acting on section a-a (see Figure 1) is smaller than the magnitude of the net uniformly distributed unbalanced vertical load. In this case, the maximum beam shear calculated using the symbiotic method will be equal to the beam end reaction. Figure 7b shows a representative beam shear diagram for this case.

Note that it is assumed that the unbalanced vertical load acts downward for the shear diagrams shown in Figure 7. When the unbalanced vertical force acts upward, the beam shear diagrams would be mirrored about the x -axis to those shown in Figure 7.

Possible Beam Moment Diagrams

Many factors affect the beam moment diagram in a chevron frame; relative magnitude of the unbalanced vertical force, the direction of the unbalanced vertical force (up or down), the magnitude of the tension brace force relative to the compression brace force, whether or not the tension brace is on the left side and the compression brace on the right side or vice versa can all affect the beam shear diagram. Figure 8 shows some possible diagrams.

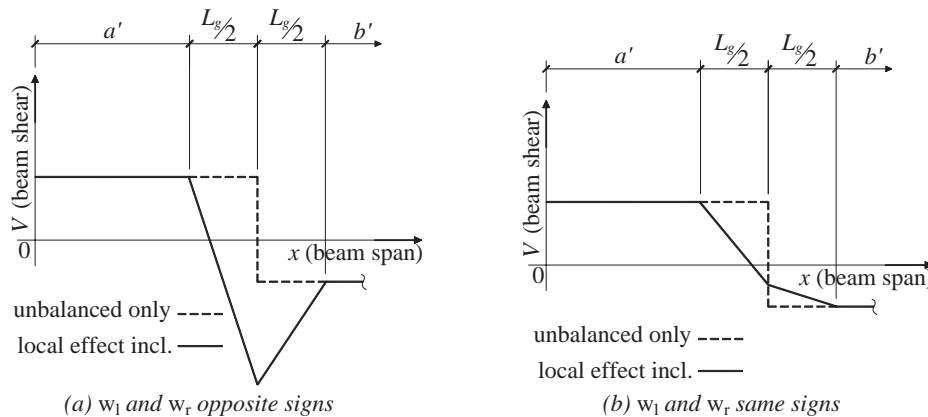


Fig. 7. Representative beam shear diagrams.

In the diagrams shown in Figure 8, it is assumed that the unbalanced vertical force acts downward. Readers should be aware that this is not always the case—for example, if the braces frame to only the bottom side of the beam and the magnitude of the compression brace is larger than that of the tension brace, the unbalanced vertical force will act upward resulting in moment diagrams that would be mirrored about the x -axis to those diagrams shown in Figure 8.

When the unbalanced vertical force is zero (a balanced case) or relatively small, the chevron effect will dominate the demands on the beam relative to considering only the unbalanced vertical load (i.e., the current beam designer method). Figure 8a shows a representative moment diagram for such a case. The required beam moment calculated neglecting the local effect of the connection can be significantly underestimated when the unbalanced load is relatively small.

When q and R_1 are the same sign, the maximum moment calculated considering the local effect will be maximum within the left half of the gusset, but whether the local effect is dominant depends on the relative magnitude of the unbalanced load. See Figures 8a and 8b.

When q and R_1 have different signs, one of two things will occur: (1) The local effect does not dominate the maximum moment (see Figure 8c), and considering the local effects will result in a lighter beam in regard to required moment, or (2) the maximum moment considering the local effects occurs within the right half of the gusset (see Figure 8d), but whether the local effect is dominant varies on the relative magnitude of the unbalanced load. In this case, the maximum moment should be evaluated using the equations derived above for $M(x_2)$.

Additionally, the moment diagram shown in Figure 8d shows a case where the local effect is dominant. This type of diagram occurs when q and R_1 have different signs and $M_{max,local}$ is less than $M_{max,unbal}$. Equations for calculating $M_{max,local}$ and $M_{max,unbal}$ were derived in the “Evaluating the Chevron Effect” section.

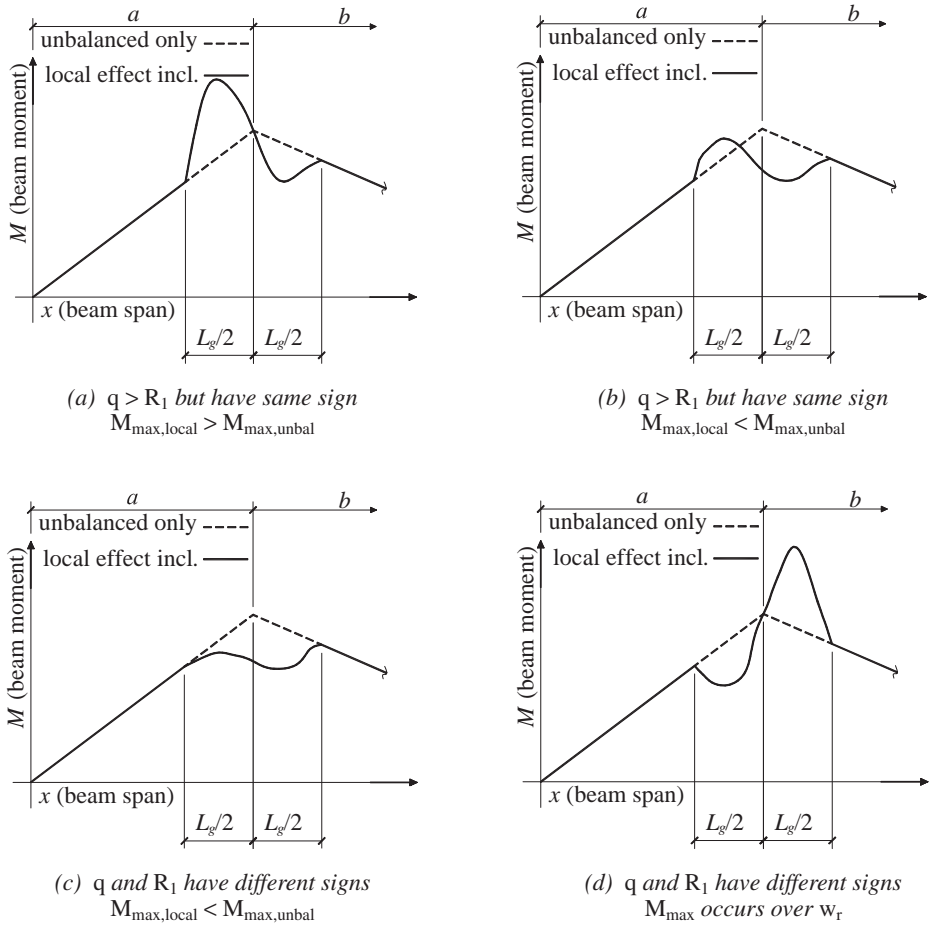


Fig. 8. Representative beam moment diagrams. (Note: Δ is assumed to be zero in these figures.)

EXAMPLE PROBLEM 1

The braced frame shown in the elevation in Figure 9a is used in a special concentrically braced frame. Figure 9b shows the brace forces calculated using the requirements of Section F2.3 of AISC 341-16 (AISC, 2016), which requires an analysis of the frame when the compression braces reach their expected buckling and post-buckling strength while the tension brace reaches its expected tension strength.

Part 1

Considering only the brace forces and load cases shown in Figure 9b for joint 1,

- Determine the approximate gusset length, $L_{g,approx}$, and half-beam depth, $e_{b,app}$.
- Use the proposed equations, using the approximate gusset geometry,
 - To determine if the chevron effect needs to be considered for the required beam moment.
 - To size the beam for shear and bending. Check both load cases; buckling load case and post-buckling load case.

Note that beam selected in this part will be the beam used by the connection designer for performing Part 2 of the problem. Additionally, the beam designer does not communicate the approximated gusset length, $L_{g,app}$, determined in this part to the connection designer for the work to be performed Part 2.

Part 2

Figure 10 shows the connection geometry (chosen by the connection designer) and brace forces for the two load cases being considered. Note that this is not necessarily the L_g dimension approximated by the beam designer in Part 1. The beam size given in Figure 10 is the beam size provided by the beam designer as given in Part 1 of this problem.

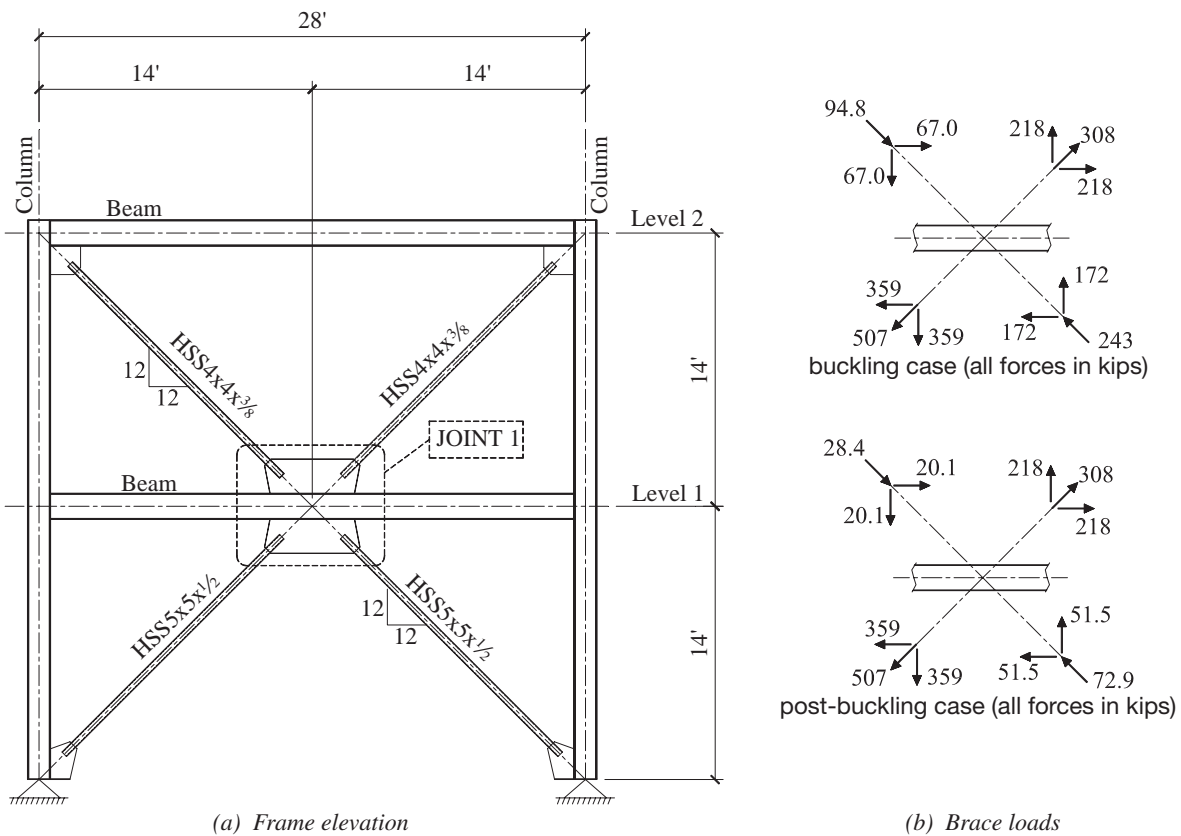


Fig. 9. Braced frame elevation and brace loads.

- Draw free-body diagrams of the left and right halves of the gussets showing the forces acting on sections a-a and b-b for both the top and bottom gussets (similar to Figure 1).
- Draw beam-loading diagrams for the two load cases showing the uniformly distributed loads and moments acting on the beam due to the brace forces (similar to Figure 4).

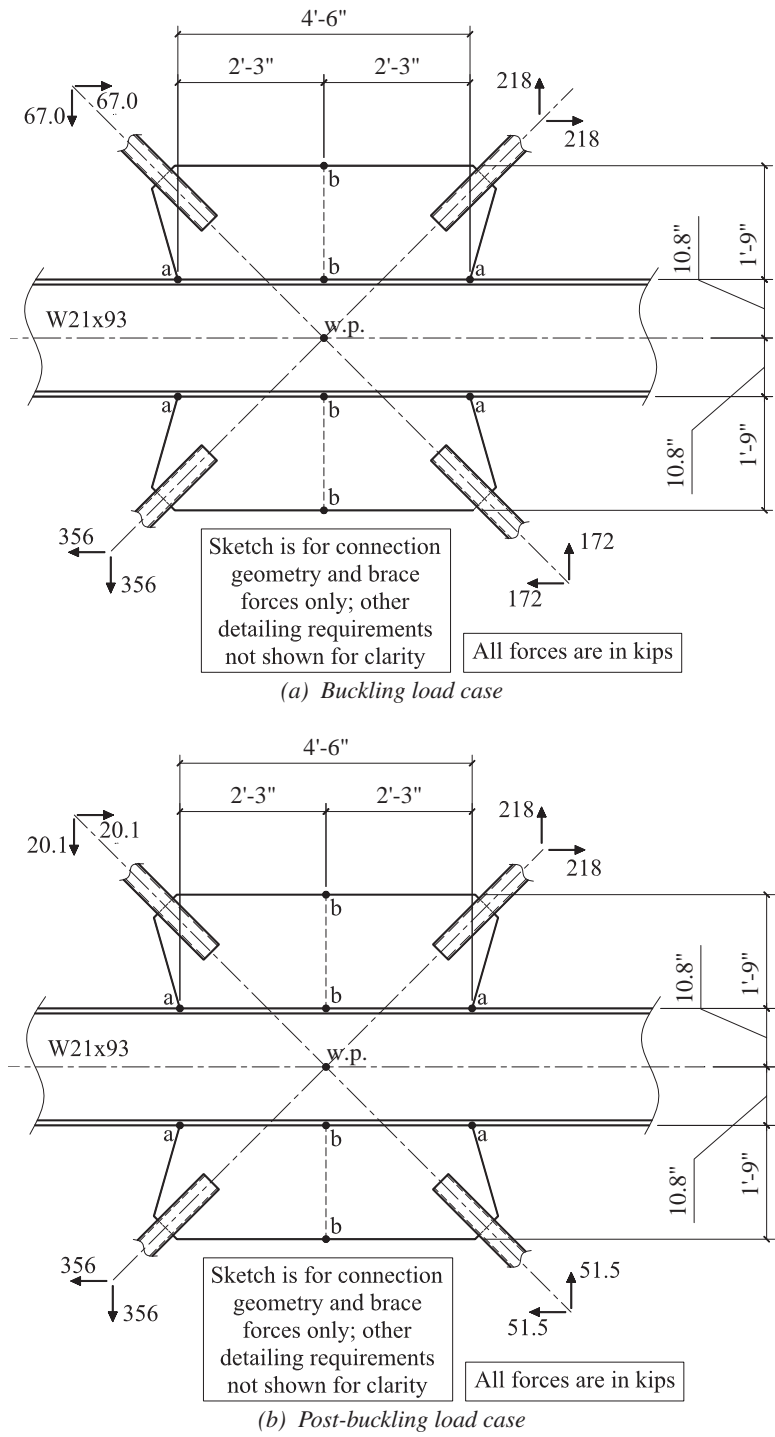


Fig. 10. Connection geometry and brace forces.

Part 3

Draw the beam shear and moment diagrams for both load cases. On each diagram, show plots for the two paradoxical methods (current standard of care used by beam designers and connection designers) as well as the symbiotic method.

Solution

General Calculations

Buckling load case:

$$\begin{aligned}(\Sigma V)_t &= (-67.0 \text{ kips}) + 218 \text{ kips} \\ &= 151 \text{ kips}\end{aligned}$$

$$\begin{aligned}(\Sigma V)_b &= (-359 \text{ kips}) + 172 \text{ kips} \\ &= -187 \text{ kips}\end{aligned}$$

$$\begin{aligned}(\Sigma H)_t &= (67.0 \text{ kips}) + 218 \text{ kips} \\ &= 285 \text{ kips}\end{aligned}$$

$$\begin{aligned}(\Sigma H)_b &= (-359 \text{ kips}) + (-172 \text{ kips}) \\ &= -531 \text{ kips}\end{aligned}$$

$$\begin{aligned}(\Sigma V)_T &= (151 \text{ kips}) + (-187 \text{ kips}) \\ &= -36.0 \text{ kips}\end{aligned}$$

Similar to Equation 21, the total net horizontal load, $(\Sigma H)_T$ is

$$\begin{aligned}(\Sigma H)_T &= (\Sigma H)_t + (\Sigma H)_b \\ &= 285 \text{ kips} + (-531 \text{ kips}) \\ &= -246 \text{ kips}\end{aligned}$$

Post-buckling load case:

$$\begin{aligned}(\Sigma V)_t &= (-20.1 \text{ kips}) + 218 \text{ kips} \\ &= 197.9 \text{ kips}\end{aligned}$$

$$\begin{aligned}(\Sigma V)_b &= (-359 \text{ kips}) + 51.5 \text{ kips} \\ &= -307.5 \text{ kips}\end{aligned}$$

$$\begin{aligned}(\Sigma H)_t &= 20.1 \text{ kips} + 218 \text{ kips} \\ &= 238.1 \text{ kips}\end{aligned}$$

$$\begin{aligned}(\Sigma H)_b &= (-359 \text{ kips}) + (-51.1 \text{ kips}) \\ &= -410.5 \text{ kips}\end{aligned}$$

$$\begin{aligned}(\Sigma V)_T &= 197.9 \text{ kips} + (-307.5 \text{ kips}) \\ &= -109.6 \text{ kips}\end{aligned}$$

$$\begin{aligned}(\Sigma H)_T &= 238.1 \text{ kips} + (-410.5 \text{ kips}) \\ &= -172.4 \text{ kips}\end{aligned}$$

Part 1

The approximate length of the gusset, $L_{g,app}$, and half-depth of the beam, $e_{b,app}$ (Fortney and Thornton, 2015) can be determined using Equations 42 and 43, respectively:

$$\begin{aligned} L_{g,app} &= \frac{L}{6} \\ &= \frac{(28 \text{ ft})(12 \text{ in./ft})}{6} \\ &= 56.0 \text{ in.} \end{aligned} \quad (42)$$

$$\begin{aligned} e_{b,app} &= (0.375)(\text{span of beam in feet}) \\ &= (0.375)(28 \text{ ft}) \\ &= 10.5 \text{ in.} \end{aligned} \quad (43)$$

Equation 48 ($\Delta = 0$) can be used to determine if the chevron effect needs to be considered in regard to beam bending. Equation 48 requires the calculation of M_T [Equations 4 and 13, for $(M_{a-a})_b$ and $(M_{a-a})_t$, respectively].

Buckling Load Case

The gusset interface moments for the buckling case are (noting that $\Delta = 0$ for this problem)

$$\begin{aligned} (M_{a-a})_t &= (H_1 + H_2)_t e_b + (V_1 + V_2)_t \Delta \\ &= (67.0 \text{ kips} + 218 \text{ kips})(10.5 \text{ in.}) + [(-67.0 \text{ kips}) + 218 \text{ kips}](0 \text{ in.}) \\ &= 2,993 \text{ kip-in.} \end{aligned} \quad (13)$$

$$\begin{aligned} (M_{a-a})_b &= (V_1 + V_2)_b \Delta - (H_1 + H_2)_b e_b \\ &= (-359 \text{ kips} + 172 \text{ kips})(0 \text{ in.}) - [(-359 \text{ kips}) + -172 \text{ kips}](10.5 \text{ in.}) \\ &= 5,576 \text{ kip-in.} \end{aligned} \quad (4)$$

$$\begin{aligned} M_T &= (M_{a-a})_t + (M_{a-a})_b \\ &= 2,993 \text{ kips-in.} + 5,576 \text{ kips-in.} \\ &= 8,569 \text{ kip-in.} \end{aligned}$$

The net uniformly distributed moment, q , is

$$\begin{aligned} q &= \left[(\Sigma H)_t - (\Sigma H)_b \right] \left(\frac{e_b}{L_g} \right) \\ &= [285 \text{ kips} - (-531 \text{ kips})] \left(\frac{10.5 \text{ in.}}{56.0 \text{ in.}} \right) \\ &= 153 \text{ kip-in./in.} \end{aligned} \quad (25)$$

The net uniformly distributed load on the left half of the gusset, w_l , is

$$\begin{aligned} w_l &= - \left(\frac{4M_{a-a}}{L_g^2} \right)_t - \left(\frac{4M_{a-a}}{L_g^2} \right)_b + \left(\frac{\Sigma V}{L_g} \right)_t + \left(\frac{\Sigma V}{L_g} \right)_b \\ &= - \left[\frac{(4)(2,993 \text{ kip-in.})}{(56.0 \text{ in.})^2} \right] - \left[\frac{(4)(5,576 \text{ kip-in.})}{(56.0 \text{ in.})^2} \right] + \left(\frac{151 \text{ kips}}{56.0 \text{ in.}} \right) + \left(\frac{-187 \text{ kips}}{56.0 \text{ in.}} \right) \\ &= -11.6 \text{ kip/in.} \end{aligned} \quad (22)$$

The left beam end reaction, R_1 , is

$$\begin{aligned}
 R_1 &= \frac{-(\Sigma V)_T b}{L} \\
 &= \frac{-(-36.0 \text{ kips})(14 \text{ ft})}{28 \text{ ft}} \\
 &= 18.0 \text{ kips}
 \end{aligned} \tag{20}$$

The equivalent gusset length, $L_{g,eq}$ is

$$\begin{aligned}
 L_{g,eq} &= \frac{M_T}{(\Sigma V)_T} \left[\frac{\frac{b}{L} - \sqrt{\frac{b}{L}}}{\frac{b}{L} - \left(\frac{b}{L}\right)^2} \right] \\
 &= \frac{8,569 \text{ kip-in.}}{-36.0 \text{ kips}} \left[\frac{\left(\frac{14 \text{ ft}}{28 \text{ ft}}\right) - \sqrt{\frac{14 \text{ ft}}{28 \text{ ft}}}}{\left(\frac{14 \text{ ft}}{28 \text{ ft}}\right) - \left(\frac{14 \text{ ft}}{28 \text{ ft}}\right)^2} \right] \\
 &= 197 \text{ in.} > L_{g,app} = 56.0 \text{ in.}
 \end{aligned} \tag{48}$$

The chevron effect will dominate the beam moment, producing a larger moment relative to the classical Pab/L type of analysis (i.e., the beam designer's approach). It is unreasonable to consider increasing the gusset length to 135 in.

Post-Buckling Load Case

The gusset interface moments for the post-buckling case are

$$\begin{aligned}
 (M_{a-a})_t &= (H_1 + H_2)_t e_b + (V_1 + V_2)_t \Delta \\
 &= (20.1 \text{ kips} + 218 \text{ kips})(10.5 \text{ in.}) + [(-20.1 \text{ kips}) + 218 \text{ kips}](0 \text{ in.}) \\
 &= 2,500 \text{ kip-in.}
 \end{aligned} \tag{13}$$

$$\begin{aligned}
 (M_{a-a})_b &= (V_1 + V_2)_b \Delta - (H_1 + H_2)_b e_b \\
 &= (-359 \text{ kips} + 51.5 \text{ kips})(0 \text{ in.}) - [-359 \text{ kips} + (-51.5 \text{ kips})](10.5 \text{ in.}) \\
 &= 4,310 \text{ kip-in.}
 \end{aligned} \tag{4}$$

The net uniformly distributed moment, q , is

$$\begin{aligned}
 q &= [(\Sigma H)_t - (\Sigma H)_b] \left(\frac{e_b}{L_g} \right) \\
 &= [238.1 \text{ kips} - (-410.5 \text{ kips})] \left(\frac{10.5 \text{ in.}}{56.0 \text{ in.}} \right) \\
 &= 122 \text{ kip-in./in.}
 \end{aligned} \tag{25}$$

The net uniformly distributed load on the left half of the gusset, w_l , is

$$\begin{aligned}
 w_l &= -\left(\frac{4M_{a-a}}{L_g^2} \right)_t - \left(\frac{4M_{a-a}}{L_g^2} \right)_b + \left(\frac{\Sigma V}{L_g} \right)_t + \left(\frac{\Sigma V}{L_g} \right)_b \\
 &= -\left(\frac{4(2,500 \text{ kip-in.})}{(56.0 \text{ in.})^2} \right) - \left(\frac{4(4,310 \text{ kip-in.})}{(56.0 \text{ in.})^2} \right) + \left(\frac{197.9 \text{ kips}}{56.0 \text{ in.}} \right) + \left(\frac{-307.5 \text{ kips}}{56.0 \text{ in.}} \right) \\
 &= -10.7 \text{ kip/in.}
 \end{aligned} \tag{22}$$

The left beam end reaction, R_1 , is

$$\begin{aligned} R_1 &= \frac{-(\Sigma V)_T b}{L} \\ &= \frac{-(-109.6 \text{ kips})(14 \text{ ft})}{28 \text{ ft}} \\ &= 54.8 \text{ kips} \end{aligned} \quad (20)$$

The equivalent gusset length, $L_{g,eq}$ is

$$\begin{aligned} L_{g,eq} &= \frac{M_T}{(\Sigma V)_T} \left[\frac{\frac{b}{L} - \sqrt{\frac{b}{L}}}{\frac{b}{L} - \left(\frac{b}{L}\right)^2} \right] \\ &= \frac{6,810 \text{ kip-in.}}{-109.6 \text{ kips}} \left[\frac{0.50 - \sqrt{0.50}}{0.50 - (0.50)^2} \right] \\ &= 51.5 \text{ in.} < L_{g,app} = 56.0 \text{ in.} \end{aligned} \quad (48)$$

The chevron effect will not dominate the beam moment and will produce a slightly smaller moment relative to the classical Pab/L type of analysis.

The maximum beam shear can be calculated using Equation 33.

For the buckling case, $R_1 = 18.0$ kips, $w_l = -11.6$ kip/in., and V_{max} is then

$$\begin{aligned} V_{max} &= R_1 + 0.5w_l L_g \\ &= 18.0 \text{ kips} + 0.5(-11.6 \text{ kip-in.})(56.0 \text{ in.}) \\ &= -307 \text{ kips} \end{aligned} \quad (33)$$

For the post-buckling case, $R_1 = 54.8$ kips, $w_l = -10.7$ kip/in., and V_{max} is then

$$\begin{aligned} V_{max} &= 54.8 \text{ kips} + 0.5(-10.7 \text{ kip-in.})(56.0 \text{ in.}) \\ &= -245 \text{ kips} \end{aligned}$$

For both load cases, w_l acts downward. As discussed previously, w_l is the second derivative of $M(x_1)$; when w_l acts downward, the maximum moment occurs along the left half of the gusset. Therefore, Equation 30 can be used to calculate the maximum beam moment, using Equation 28 to determine the location of maximum moment (x_1).

The maximum beam moment for the buckling case is located at

$$\begin{aligned} x_1 &= \frac{-R_1 - q}{w_l} \\ &= \frac{-18.0 \text{ kips} - 153 \text{ kip-in./in.}}{-11.6 \text{ kip/in.}} \\ &= 14.8 \text{ in.} \end{aligned} \quad (28)$$

and is

$$\begin{aligned} M_{max} &= R_1 a' + (R_1 + q) \left(\frac{-R_1 - q}{w_l} \right) + 0.5w_l \left(\frac{-R_1 - q}{w_l} \right)^2 \\ &= (18.0 \text{ kips})(14.0 \text{ in.}) + (18.0 \text{ kips} + 153 \text{ kips})(14.8 \text{ in.}) + 0.5(-11.6 \text{ kip/in.})(14.8 \text{ in.})^2 \\ &= 3,780 \text{ kip-in.} \end{aligned} \quad (30)$$

Table 1. Maximum Beam Shear and Moment		
Load Case	V_{max}	M_{max}
	(kips)	(kip-in.)
Buckling	-307	3780
Post-buckling	-245	9130

The maximum beam moment for the post-buckling case is located at

$$x_1 = \frac{-54.8 \text{ kips} - 122 \text{ kip-in./in.}}{-10.7 \text{ kip/in.}}$$

$$= 16.5 \text{ in.}$$

and is

$$M_{max} = (54.8 \text{ kips})(140 \text{ in.}) + (54.8 \text{ kips} + 122 \text{ kips})(16.5 \text{ in.}) + 0.5(-10.7 \text{ kip/in.})(16.5 \text{ in.})^2$$

$$= 9,130 \text{ kip-in.}$$

As can be seen in Table 1, the buckling case gives the largest beam shear, -307 kips, and the post-buckling case gives the largest beam moment, 9,130 kip-in. A beam size will be selected for these values. Also recall that the beam half-depth, e_b , was approximated to be 10.5 in. Therefore, a beam size will be selected from the W21 family.

Assuming the beam will be laterally braced such that its plastic bending strength can be reached, the required plastic section modulus, Z_{req} , is

$$Z_{req} = \frac{9,130 \text{ kip-in.}}{(0.9)(50 \text{ ksi})}$$

$$= 203 \text{ in.}^3$$

Using AISC *Manual* Table 3-2 (AISC, 2017), a W21×93 has an available design shear and flexural strength of 376 kips and 9,948 kip-in., respectively.

Final beam size: W21×93

Part 2

The force distributions in the top and bottom connections for the buckling and post-buckling load cases are shown in Figures 11a and 11b, respectively. The force distribution equations given in Equations 2 through 19 were used to calculate the forces and moment shown, but the calculations are not shown here in order to conserve space. Fortney and Thornton (2015) provide several examples showing the use of these equations.

Beam Loading Using the Symbiotic Method

Buckling load case:

The moments, $(M_{a-a})_t$ and $(M_{a-a})_b$, are

$$(M_{a-a})_t = (H_1 + H_2)_t e_b + (V_1 + V_2)_t \Delta \tag{13}$$

$$(M_{a-a})_t = (67.0 \text{ kips} + 218 \text{ kips})(10.8 \text{ in.}) + (-67.0 \text{ kips} + 218 \text{ kips})(0 \text{ in.})$$

$$= 3,078 \text{ kip-in.}$$

$$(M_{a-a})_b = (V_1 + V_2)_b \Delta - (H_1 + H_2)_b e_b \quad (4)$$

$$\begin{aligned} (M_{a-a})_b &= (-359 \text{ kips} + 172 \text{ kips})(0 \text{ in.}) - [-359 \text{ kips} + (-172 \text{ kips})](10.8 \text{ in.}) \\ &= 5,735 \text{ kip-in.} \end{aligned}$$

$$\begin{aligned} M_T &= (M_{a-a})_t + (M_{a-a})_b \\ &= 3,078 \text{ kips-in.} + 5,735 \text{ kips-in.} \\ &= 8,813 \text{ kip-in.} \end{aligned}$$

The net uniformly distributed loads, w_l and w_r , can be calculated using Equations 22 and 23, respectively:

$$\begin{aligned} w_l &= -\left(\frac{4M_{a-a}}{L_g^2}\right)_t - \left(\frac{4M_{a-a}}{L_g^2}\right)_b + \left(\frac{\sum V}{L_g}\right)_t + \left(\frac{\sum V}{L_g}\right)_b \quad (22) \\ &= -\left(\frac{4(3,078 \text{ kip-in.})}{(54.0 \text{ in.})^2}\right) - \left(\frac{4(5,735 \text{ kip-in.})}{(54.0 \text{ in.})^2}\right) + \left(\frac{151 \text{ kips}}{54.0 \text{ in.}}\right) + \left(\frac{-187 \text{ kips}}{54.0 \text{ in.}}\right) \\ &= -12.8 \text{ kip/in.} \end{aligned}$$

$$\begin{aligned} w_r &= \left(\frac{4M_{a-a}}{L_g^2}\right)_t + \left(\frac{4M_{a-a}}{L_g^2}\right)_b + \left(\frac{\sum V}{L_g}\right)_t + \left(\frac{\sum V}{L_g}\right)_b \quad (23) \\ &= \left[\frac{4(3,078 \text{ kip-in.})}{(54.0 \text{ in.})^2}\right] + \left[\frac{4(5,735 \text{ kip-in.})}{(54.0 \text{ in.})^2}\right] + \left(\frac{151 \text{ kips}}{54.0 \text{ in.}}\right) + \left(\frac{-187 \text{ kips}}{54.0 \text{ in.}}\right) \\ &= 11.4 \text{ kip/in.} \end{aligned}$$

The net uniformly distributed moment, q , is

$$\begin{aligned} q &= [(\sum H)_t - (\sum H)_b] \left(\frac{e_b}{L_g}\right) \quad (25) \\ &= [285 \text{ kips} - (-531 \text{ kips})] \left(\frac{10.8 \text{ in.}}{54.0 \text{ in.}}\right) \\ &= 163 \text{ kip-in./in.} \end{aligned}$$

Given that $R_1 = 18.0$ kips (calculated previously), and the gusset length, L_g , is 54.0 in., the equivalent gusset length, $L_{g,eq}$, is

$$\begin{aligned} L_{g,eq} &= \frac{M_T}{(\sum V)_T} \left[\frac{\frac{b}{L} - \sqrt{\frac{b}{L}}}{\frac{b}{L} - \left(\frac{b}{L}\right)^2} \right] \quad (48) \\ &= \frac{8,813 \text{ kip-in.}}{-36.0 \text{ kips}} \left[\frac{0.50 - \sqrt{0.50}}{0.50 - (0.50)^2} \right] \\ &= 203 \text{ in.} > L_g = 54.0 \text{ in.} \end{aligned}$$

Therefore, the local effects will dominate the moment. However, for this example, the post-buckling case governs for beam moment.

Post-buckling load case:

The moments, $(M_{a-a})_t$ and $(M_{a-a})_b$, are

$$(M_{a-a})_t = (20.1 \text{ kips} + 218 \text{ kips})(10.8 \text{ in.}) + (-20.1 \text{ kips} + 218 \text{ kips})(0 \text{ in.}) = 2,571 \text{ kip-in.}$$

$$(M_{a-a})_b = (-359 \text{ kips} + 51.5 \text{ kips})(0 \text{ in.}) - [-359 \text{ kips} + (-51.5 \text{ kips})](10.8 \text{ in.}) = 4,433 \text{ kip-in.}$$

$$M_T = (M_{a-a})_t + (M_{a-a})_b = 2,571 \text{ kips-in.} + 4,433 \text{ kips-in.} = 7,004 \text{ kip-in.}$$

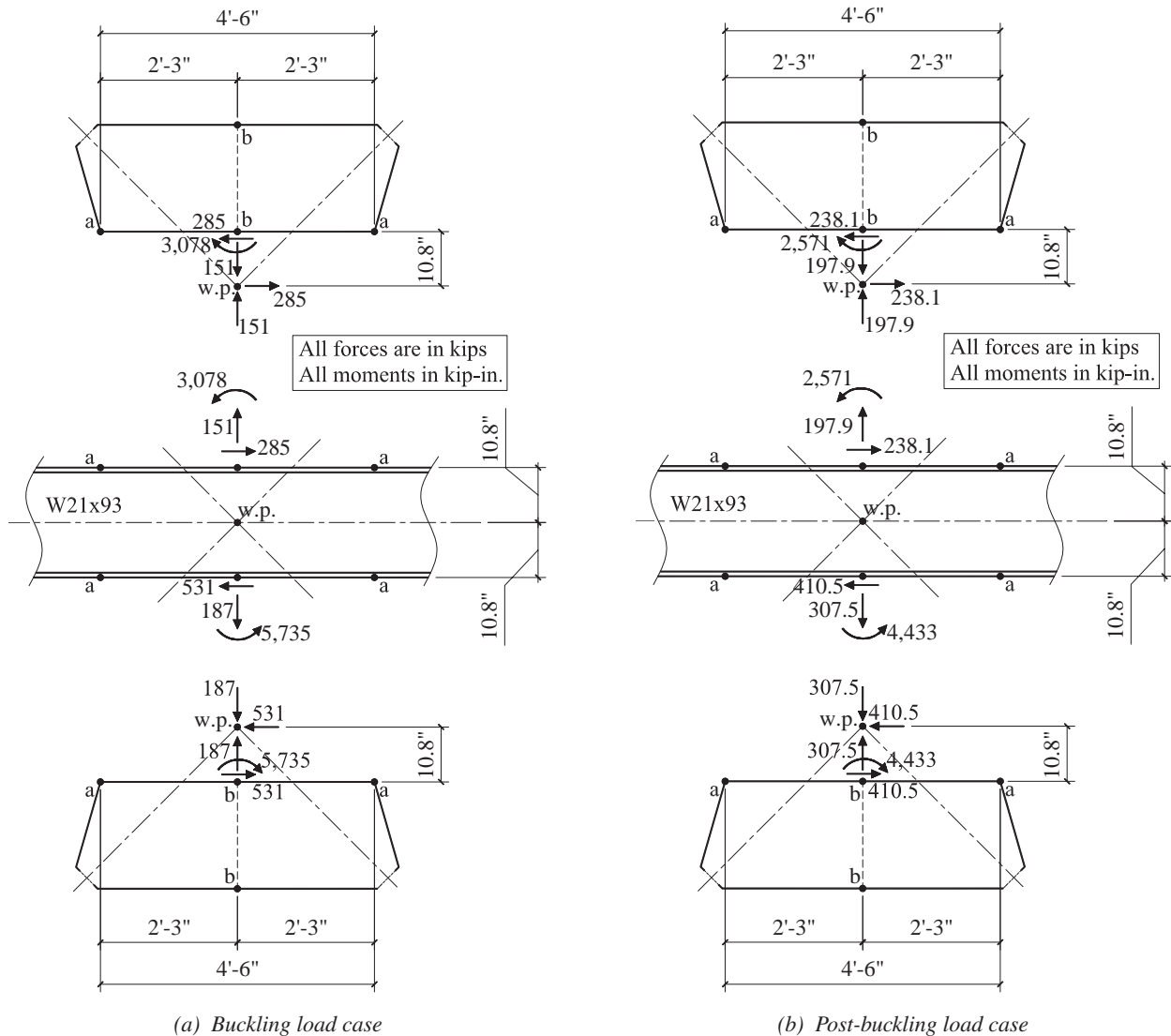


Fig. 11. Connection force distributions.

The net uniformly distributed loads, w_l and w_r , can be calculated using Equations 22 and 23, respectively:

$$w_l = -\left[\frac{4(2,571 \text{ kip-in.})}{(54.0 \text{ in.})^2} \right] - \left[\frac{4(4,433 \text{ kip-in.})}{(54.0 \text{ in.})^2} \right] + \left(\frac{197.9 \text{ kips}}{54.0 \text{ in.}} \right) + \left(\frac{-307.5 \text{ kips}}{54.0 \text{ in.}} \right)$$

$$= -11.6 \text{ kip/in.}$$

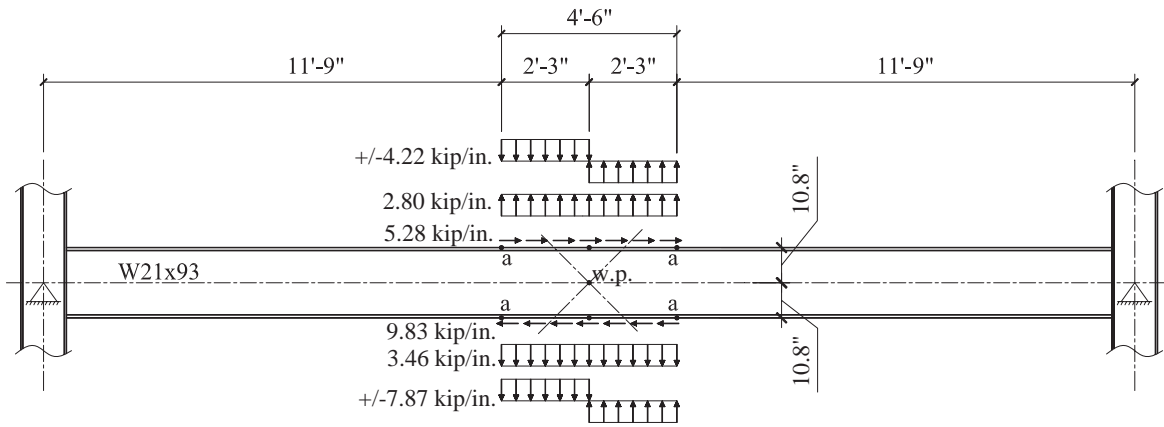
$$w_r = \left[\frac{4(2,571 \text{ kip-in.})}{(54.0 \text{ in.})^2} \right] + \left[\frac{4(4,433 \text{ kip-in.})}{(54.0 \text{ in.})^2} \right] + \left(\frac{197.9 \text{ kips}}{54.0 \text{ in.}} \right) + \left(\frac{-307.5 \text{ kips}}{54.0 \text{ in.}} \right)$$

$$= 7.58 \text{ kip/in.}$$

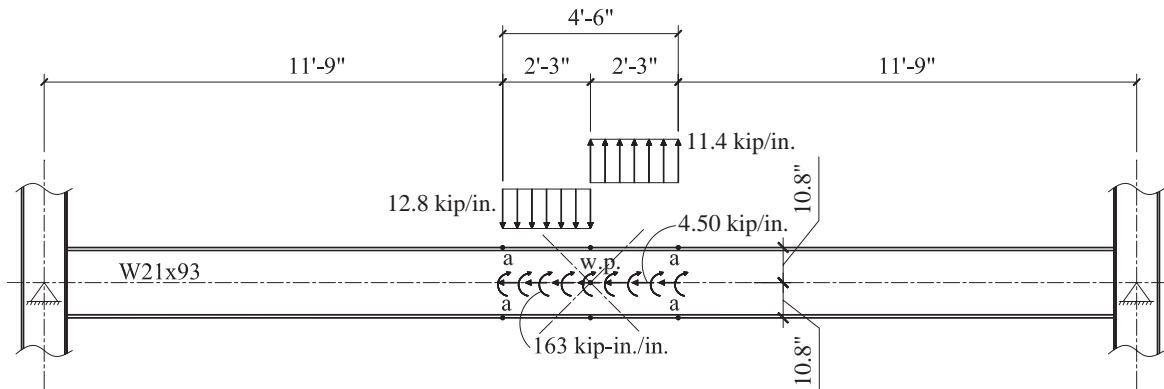
The net uniformly distributed moment, q , is

$$q = [238.1 \text{ kips} - (-410.5 \text{ kips})] \left(\frac{10.8 \text{ in.}}{54.0 \text{ in.}} \right)$$

$$= 130 \text{ kip-in./in.}$$



(a) Uniformly distributed beam loading



(b) Statically equivalent net beam loading

Fig. 12. Beam loading for buckling load case—sybiotic method.

Given that $R_1 = 54.8$ kips (calculated previously), and the gusset length, L_g , is 54.0 in., the equivalent gusset length, $L_{g,eq}$, is

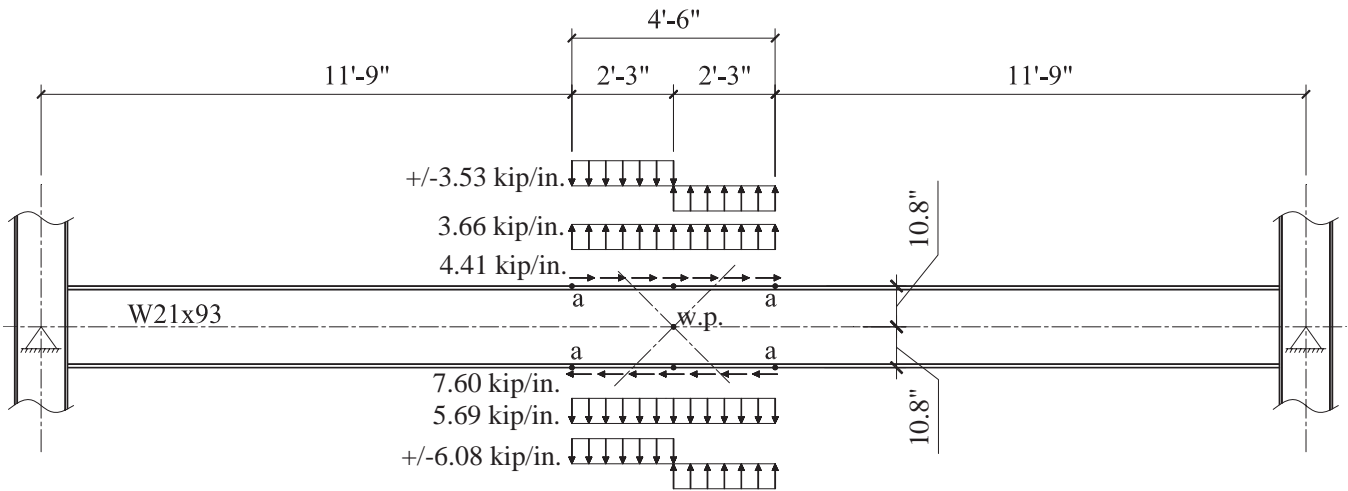
$$L_{g,eq} = \frac{7,004 \text{ kip-in.}}{-109.6 \text{ kips}} \left[\frac{0.50 - \sqrt{0.50}}{0.50 - (0.50)^2} \right]$$

$$= 52.9 \text{ in.} < L_g = 54.0 \text{ in.}$$

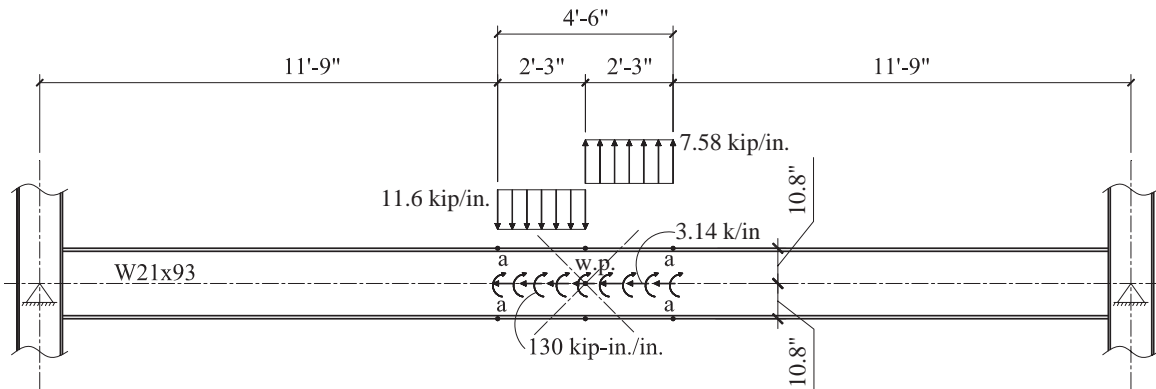
Therefore, the symbiotic method will produce a slightly smaller (very slight difference) beam moment than the current beam designer's method which neglects the local effect. Note that the beam designer used an approximate gusset length of 56.0 in.—2 in. longer than the 54.0 in. used by the connection designer. It is important however, to recognize that neglecting the local effects when determining beam shear will still produce a very unconservative estimate of beam shear. The beam loading for the buckling and post-buckling load cases are shown in Figures 12 and 13, respectively.

Beam Shear and Moment—Current Beam Designer's Method

With this method, the span of the beam and the location of the work point are considered; local effects from the connection are not considered.



(a) Uniformly distributed beam loading



(b) Statically equivalent net beam loading

Fig. 13. Beam loading for post-buckling load case—symbiotic method.

The total summation of the vertical components of the brace forces is treated as a concentrated load acting on the beam at the work point. For this example, the work point is located at mid-span of the beam, so beam shear and moment will be distributed using the following equations. In the following equations, x_1 and x_2 are measured starting from the left beam end and the location of the work point, respectively:

$$R_1 = R_2 = \frac{-(\sum V)_T}{2}$$

$$V(x_1) = R_1$$

$$V(x_2) = -R_2$$

$$M(x_1) = R_1 x_1$$

$$M(x_2) = R_1 a - R_2 x_2$$

Beam Shear and Moment—Current Connection Designer’s Method

With this method, the span of the beam and the location of the work point are not considered; local effects from the connection are considered. Regardless of the unbalanced vertical load, this method assumes that beam shear and moment outside of the connection region are zero.

The beam shear and moment distribution will be as shown in Figure 3b; constant shear with linearly distributed moment acting on the along the middle half of the gusset.

Buckling load case:

$$\begin{aligned} V &= \frac{2[(M_{a-a})_t + (M_{a-a})_b]}{L_g} \\ &= \frac{2(3,078 \text{ kip-in.} + 5,735 \text{ kip-in.})}{54.0 \text{ in.}} \\ &= 326 \text{ kips} \end{aligned}$$

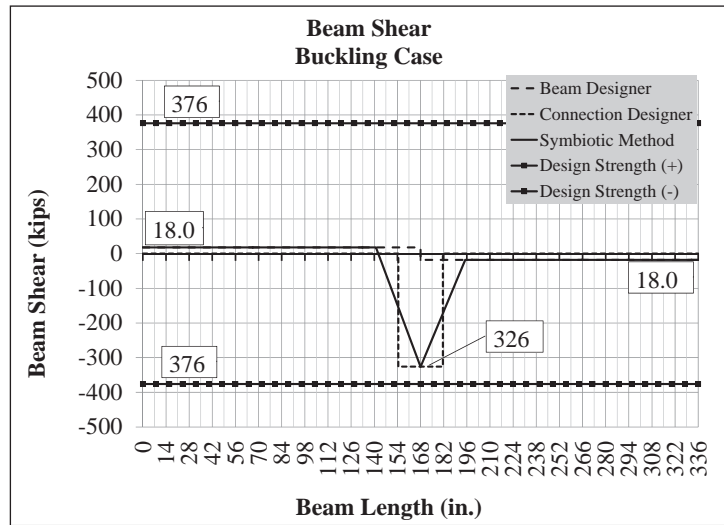
$$\begin{aligned} M &= \frac{(M_{a-a})_t + (M_{a-a})_b}{2} \\ &= \frac{3,078 \text{ kip-in.} + 5,735 \text{ kip-in.}}{2} \\ &= 4,407 \text{ kip-in.} \end{aligned}$$

Post-buckling load case:

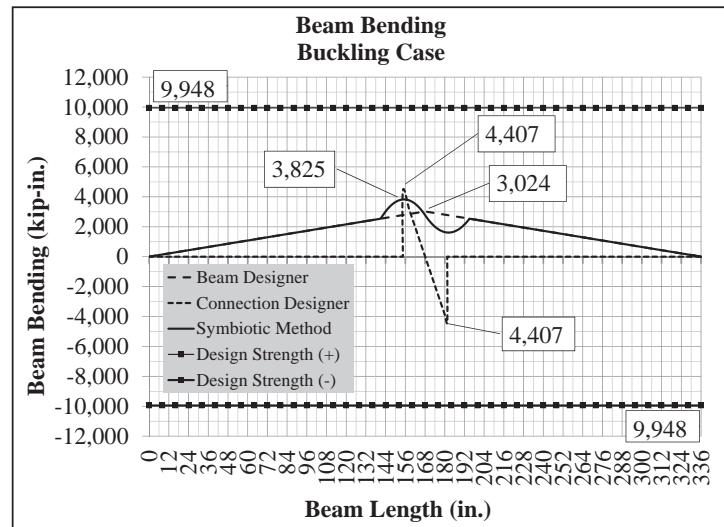
$$\begin{aligned} V &= \frac{2[(M_{a-a})_t + (M_{a-a})_b]}{L_g} \\ &= \frac{2(2,571 \text{ kip-in.} + 4,433 \text{ kip-in.})}{54.0 \text{ in.}} \\ &= 260 \text{ kips} \end{aligned}$$

$$\begin{aligned} M &= \frac{(M_{a-a})_t + (M_{a-a})_b}{2} \\ &= \frac{2,571 \text{ kip-in.} + 4,433 \text{ kip-in.}}{2} \\ &= 3,502 \text{ kip-in.} \end{aligned}$$

The beam shear and moment diagrams for the three methods considered in this example problem are shown in Figures 14 and 15 for the buckling and post-buckling loads cases, respectively.

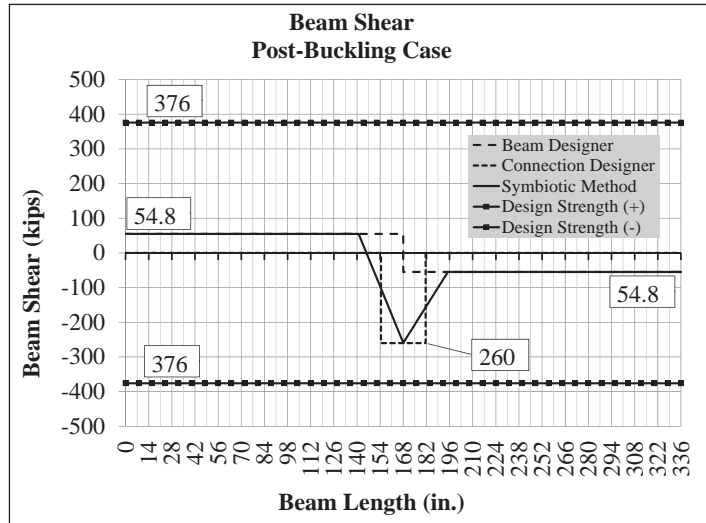


(a) Beam shear

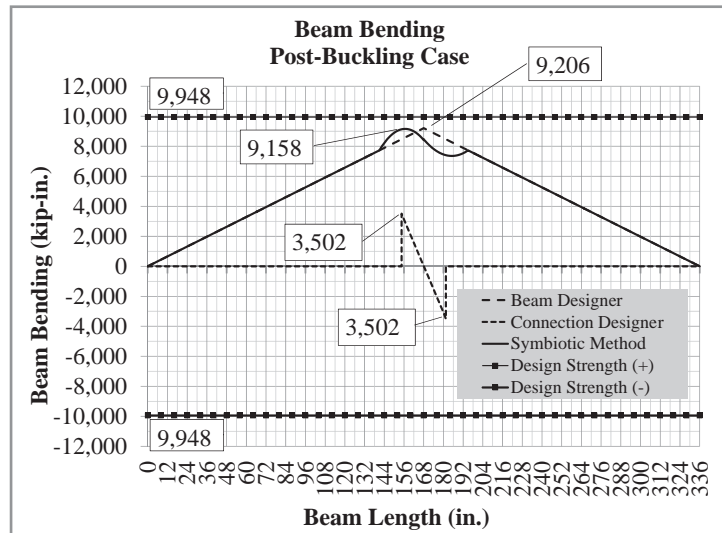


(b) Beam moment

Fig. 14. Beam shear and moment for buckling load case.



(a) Beam shear



(b) Beam moment

Fig. 15. Beam shear and moment for post-buckling load case.

EXAMPLE PROBLEM 2

Figures 14b and 15b show the moment diagrams for Example Problem 1, Part 2, based on the actual connection geometry as shown in Figure 11. Based on the geometry and loading, calculate the equivalent summation of vertical forces, $(\Sigma V)_{T,eq}$, for the buckling and post-buckling cases given in Example Problem 1 (see Figures 11, 12 and 13).

Solution

As can be seen in Figure 11, the eccentricity term, Δ , is zero. Therefore, Equation 53 is used to compute the equivalent unbalanced vertical force, $(\Sigma V)_{T,eq}$. As can be seen in Figures 12 and 13, the work point is located at mid-span of the beam, therefore, the position ratio, b/L , is equal to 0.50. Figures 12 and 13 also give the values for the net uniformly distributed moments, q .

For the buckling case, $q = 163$ kip-in./in. and $(\Sigma V)_T = -36.0$ kips. Therefore, Equation 53 gives

$$\begin{aligned}
 (\Sigma V)_{T,eq} &= q \left[\frac{\frac{b}{L} - \sqrt{\frac{b}{L}}}{\frac{b}{L} - \left(\frac{b}{L}\right)^2} \right] \\
 &= 163 \text{ kip-in./in.} \left[\frac{0.50 - \sqrt{0.50}}{0.50 - (0.50)^2} \right] \\
 &= -135 \text{ kips}
 \end{aligned} \tag{53}$$

The absolute value of $(\Sigma V)_T = 36.0$ kips is smaller than the absolute value of $(\Sigma V)_{T,eq} = 135$ kips. Therefore, the chevron effect will dominate the moment demand on the beam. The moment diagrams shown in Figure 14b support this conclusion.

For the post-buckling case, $q = 130$ kip-in./in. and $(\Sigma V)_T = -109.6$ kips. Therefore, Equation 53 gives

$$\begin{aligned}
 (\Sigma V)_{T,eq} &= 130 \text{ kip-in./in.} \left[\frac{0.50 - \sqrt{0.50}}{0.50 - (0.50)^2} \right] \\
 &= -108 \text{ kips}
 \end{aligned}$$

The absolute value of $(\Sigma V)_T = 109.6$ kips is larger than the absolute value of $(\Sigma V)_{T,eq} = 108$ kips. Therefore, the chevron effect analysis will produce a beam moment smaller than what would be calculated using the classic Pab/L analysis. However, the two values are very close, therefore the moment calculated using the symbiotic method should be only slightly smaller than that computed using the beam designer's method (Pab/L). The moment diagrams shown in Figure 15b support this conclusion; the symbiotic moment is 9,158 kip-in. as compared to the Pab/L moment equal to 9,206 kip-in.

EXAMPLE PROBLEM 3

Figures 16 and 17 show a braced frame elevation and corresponding gusset-to-beam interface forces. The total unbalanced load, $(\Sigma V)_T$, is -112 kips. The total moment, M_T , is 10,203 kip-in. Referring to Figure 16, it can be seen that Δ is nonzero and that the work point is not located at mid-span of the beam. Figure 18 shows the beam moment diagram. Using the information given in Figures 16, 17 and 18:

1. Use Equation 52 to determine if the chevron effect will dominate the maximum beam moment. That is, compare the calculated $(\Sigma V)_{T,eq}$ from Equation 52 to the actual $(\Sigma V)_T$.
2. Use Equation 47 to determine if the chevron effect will dominate the maximum beam moment. That is, compare the calculated $L_{g,eq}$ from Equation 47 to the actual L_g .
3. Calculate the maximum beam moments, $M(x_1)_{max}$ and $M(x_2)_{max}$, evaluate the second derivatives for each region, and compare to the beam moment diagram shown in Figure 18.

Solution

Part 1

Equation 52 is a function of the b/L and Δ/L_g ratios. Those ratios are

$$\frac{b}{L} = \frac{204 \text{ in.}}{336 \text{ in.}} = 0.6071$$

$$\left(\frac{b}{L}\right)^2 = (0.6071)^2 = 0.3686$$

$$\frac{\Delta}{L_g} = \frac{-4.50 \text{ in.}}{57.0 \text{ in.}} = -0.07894$$

$$\left(\frac{\Delta}{L_g}\right)^2 = (-0.07894)^2 = 0.006233$$

To simplify the number crunching required in Equation 52, the following terms within Equation 52 will be calculated and then substituted into the equation:

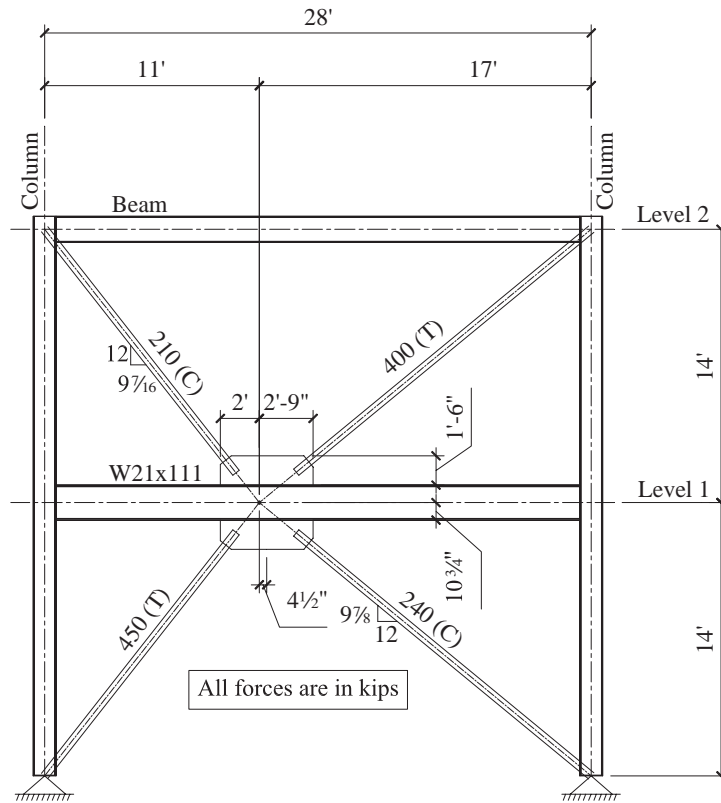


Fig. 16. Frame elevation, loading and connection geometry.

$$\frac{b}{L} + \frac{4\Delta}{L_g} \left(\frac{b}{L} \right) = 0.6071 + (4)(-0.07894)(0.6071)$$

$$= 0.4154$$

$$\left(\frac{b}{L} \right)^2 \left(\frac{8\Delta}{L_g} + \frac{16\Delta^2}{L_g^2} \right) = (0.3686)[(8)(-0.07894) + (16)(0.006233)]$$

$$= -0.1960$$

$$\frac{b}{L} \left(1 - \frac{2\Delta}{L_g} - \frac{8\Delta^2}{L_g^2} \right) = (0.6071)[1 - (2)(-0.07894) - (8)(0.006233)]$$

$$= 0.6727$$

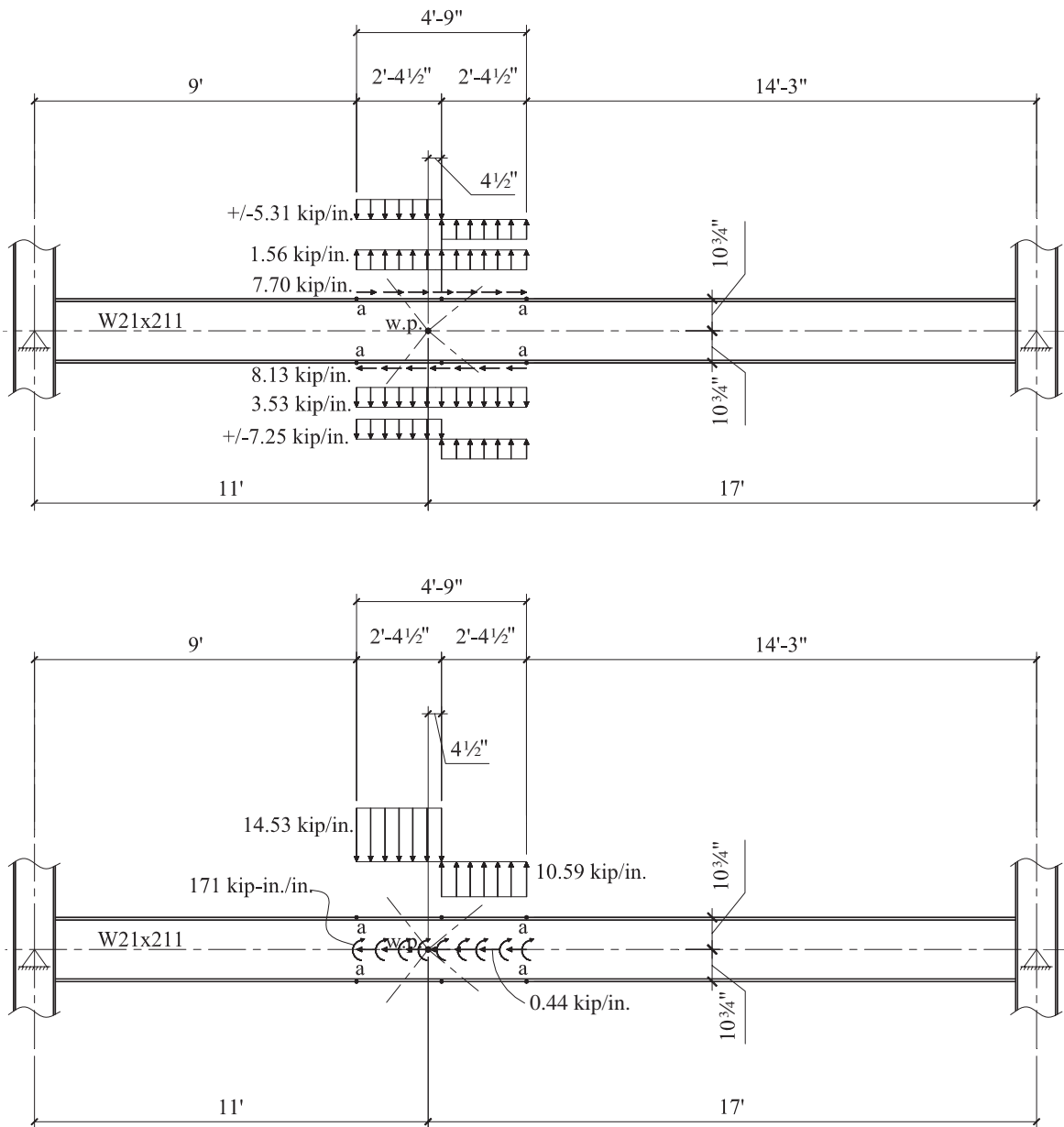


Fig. 17. Beam loading.

Equation 52 gives the following:

$$\begin{aligned}
 (\Sigma V)_{T,eq} &= \frac{q \left[\frac{b}{L} + \frac{4\Delta}{L_g} \left(\frac{b}{L} \right) \right] - q \sqrt{\left[\left(\frac{b}{L} \right)^2 \left(\frac{8\Delta}{L_g} + \frac{16\Delta^2}{L_g^2} \right) + \left(\frac{b}{L} \right) \left(1 - \frac{2\Delta}{L_g} - \frac{8\Delta^2}{L_g^2} \right) \right]}{\left(\frac{b}{L} \right) \left(1 - \frac{2\Delta}{L_g} - \frac{8\Delta^2}{L_g^2} \right) - \left(\frac{b}{L} \right)^2} \\
 &= \frac{(171 \text{ kip-in./in.})(0.4154) - (171 \text{ kip-in./in.})\sqrt{-0.1960 + 0.6727}}{0.6727 - 0.3686} \\
 &= -154 \text{ kips}
 \end{aligned}
 \tag{52}$$

The magnitude of the total unbalanced force, $(\Sigma V)_T$, for this problem is 112 kips. Comparing this magnitude of load to the magnitude of the equivalent unbalanced force, $(\Sigma V)_{T,eq}$ gives

$$|(\Sigma V)_{T,eq}| = 154 \text{ kips} > |(\Sigma V)_T| = 112 \text{ kips}$$

Therefore, the chevron effect will dominate the beam moment. Referring to Figure 18, it can be seen that Equation 51 accurately predicts this.

Part 2

Equation 47 is a function of b/L ratios as well as M_T and $(\Sigma V)_T$. The (b/L) , $(b/L)^2$ and $(b/L)^3$ ratios are 0.607, 0.369 and 0.224, respectively. The variables M_T and $(\Sigma V)_T$ were given as 10,203 kip-in and -112 kips, respectively. The square root of the discriminant, η , is

$$\begin{aligned}
 \eta &= \sqrt{(\Sigma V)_T^2 \Delta^2 \left[\frac{b}{L} - \left(\frac{b}{L} \right)^2 \right] + (\Sigma V)_T M_T \Delta \left[-8 \left(\frac{b}{L} \right)^3 + 10 \left(\frac{b}{L} \right)^2 - 2 \left(\frac{b}{L} \right) \right] + M_T^2 \left(\frac{b}{L} \right)} \\
 &= \sqrt{(-112 \text{ kips})^2 (-4.50 \text{ in.})^2 [0.607 - 0.369] + (-112 \text{ kips})(10,203 \text{ kip-in.})(-4.50 \text{ in.}) [-8(0.224) + 10(0.369) - 2(0.607)] + (10,203 \text{ kip-in.})^2 (0.607)} \\
 &= 8,171 \text{ kip}^2\text{-in.}^2
 \end{aligned}
 \tag{47b}$$

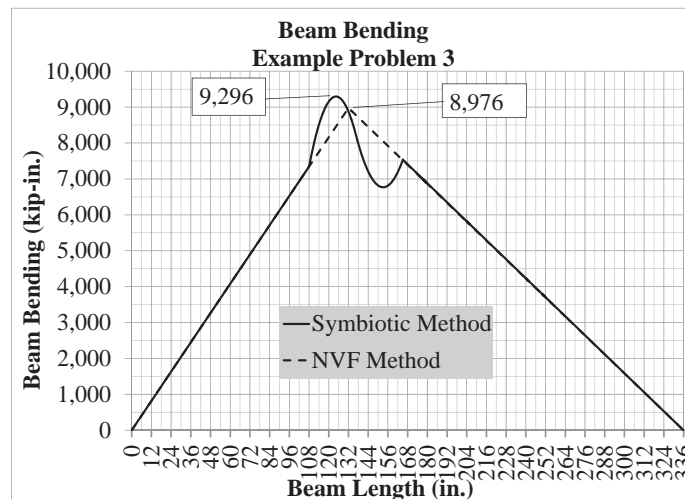


Fig. 18. Beam moment diagram for Example Problem 3.

$$\begin{aligned}
L_{g,eq} &= \frac{M_T \left(\frac{b}{L} \right) - \eta}{(\Sigma V)_T \left[\frac{b}{L} - \left(\frac{b}{L} \right)^2 \right]} & (47a) \\
&= \frac{(10,203 \text{ kip-in.})(0.607) - 8,171 \text{ kip}^2\text{-in.}^2}{(-112 \text{ kips})(0.607 - 0.369)} \\
&= 74.2 \text{ in.} > L_g = 57.0 \text{ in.}
\end{aligned}$$

Therefore, the chevron effect will dominate the beam moment relative to the Pab/L moment. The moment diagrams shown in Figure 18 support this result.

Part 3

As can be seen in Figure 16, the w_l and w_r terms are negative and positive, respectively. Additionally, the moments are in the positive region. Therefore, the second derivative of the $M(x_1)$ equation gives a maximum moment, and the second derivative of the $M(x_2)$ equation gives a minimum. The moment diagram shown in Figure 17 supports this conclusion.

FURTHER DISCUSSION

The procedures presented in this paper provide a general solution that both beam designers and connection designers can use in a consistent manner to evaluate beam shear and moment in beams of V-type and inverted V-type braced frames. Beyond the general need to have a consistent analysis procedure, the proposed procedure also has the advantage that the beam designer can account for brace connection geometry at the time the beam is sized in a manner that will ensure that beam web and flange reinforcement is not found to be required during the connection design phase.

The example problem used to illustrate the application of the proposed procedure is illustrated in the context of a seismic system using the mechanistic analysis required in the AISC *Seismic Provisions* (2016) for special concentrically braced frames. It is important to recognize that the chevron effect has an impact on beams in systems designed for low seismic and wind requirements. Posted brace forces that are used for design in low seismic and wind applications often result in an unbalanced vertical force—usually relatively small unbalanced vertical loads. As has been shown in this paper, if a beam is sized for beam shear and moment strength for relatively small unbalanced vertical loads using the current beam and connection designer’s methods, the beam shear and moment arising from the chevron effect in the connection region can be significantly underestimated, leading to expensive beam web and flange reinforcement. The proposed symbiotic method will minimize, if not eliminate, the need for such reinforcement.

Several assumptions (see the “Symbiotic Analysis Model” section) are made in regard to connection geometry, as

discussed at the beginning of this paper. It is also important to recognize that beam shear and moment can be very sensitive to beam span, location of work point, brace bevel, and brace loading. The proposed procedures are based on these assumptions and several checks are provided to ensure that the equations that have been derived apply to the problem being considered. When these assumptions are not valid, designers must take care to return to engineering fundamentals and first principles to solve that particular problem.

CONCLUSIONS

The methods used by beam designers and connection designers to evaluate beams in V-type or inverted V-type frames are not consistent. Beam designers consider beam span and work point location but ignore the effects of the connection geometry (chevron effect), while connection designers consider the effect of the moment acting on the gusset–beam interface(s) but neglect the unbalanced vertical load as well as the beam span and work point location. The symbiotic method proposed in this paper provides a consistent analysis model that can be used by beam and connection designers alike.

This paper provides beam and connection designers with methods for evaluating whether the chevron effect will dominate the moment demand on the beam and also to determine whether the current methods being used are conservative. Equation 47 can be used to evaluate a beam for a given set of brace forces and frame geometry to determine a gusset length interface that will reduce the chevron effect relative to the Pab/L moment, which is more likely useful

to a connection designer for a specific case. Equations 50 and 51 can be used to evaluate a beam for a given beam span and work point location, combined with approximated gusset lengths, $L_{g,app}$, and half-beam depths, $e_{b,app}$ (see Equations 42 and 43), to determine at what level of unbalanced vertical force the chevron effect will dominate beam demand relative to a Pab/L moment, which is more likely useful to a beam designer to use in a more general sense when evaluating multiple joints in a frame.

When the chevron effect dominates, the current analysis procedure used by beam designers and connection designers can significantly underestimate beam shear and moment in the balanced case and when a relatively small unbalanced vertical load is present. In this case, the beam can be significantly undersized for the demands imposed on the beam by the chevron effect. When the unbalanced vertical load is relatively large, the symbiotic method potentially provides a smaller beam moment demand, which may lead to a lighter beam relative to one required using the methods currently used by beam and connection designers.

ACKNOWLEDGMENTS

The authors would like to thank Mr. Joshua R. Buckholt, P.E., S.E., for his comments during the review process of this paper.

SYMBOLS

H_1	Horizontal component of force in brace 1, kips	$M_{max,local}$	Maximum beam moment when local effects are considered, kip-in.
H_2	Horizontal component of force in brace 2, kips	$M_{max,unbal}$	Maximum beam moment when local effects are not considered, kip-in.
H_{a-a}	Horizontal (shear) force acting at the gusset-to-beam interface, kips	M_T	Sum of moments at top and bottom gusset interfaces, $(M_{a-a})_t$ and $(M_{a-a})_b$, kip-in.
H_{bi}	Horizontal (normal) force acting on the critical vertical section of the gusset, kips	$M_{u,max}$	Maximum required (design) flexural strength, kip-in.
L_1	Horizontal distance from the left edge of the gusset to the work point, in.	$M(x_1)$	Beam moment as a function of x_1 , kip-in.
L_2	Horizontal distance from the right edge of the gusset to the work point, in.	$M(x_2)$	Beam moment as a function of x_2 , kip-in.
L	Span of frame beam, in.	N_{eq}	Couple of the moment, M_{a-a} , kip-in.
L_g	Contact length of the gusset-to-beam interface, in.	$P_i(T)$	Tension brace force, kips
$L_{g,app}$	Approximation of length of gusset, L_g , in.	$P_i(C)$	Compression brace force, kips
$L_{g,eq}$	Minimum gusset length required such that the chevron effect does not dominate, in.	P_1	Axial force in brace 1, kips
M_{a-a}	Moment acting at the gusset-to-beam interface, kip-in.	P_2	Axial force in brace 2, kips
M_{max}	Maximum required beam moment, kip-in.	R_1	Left beam end reaction, kips
		$R_{1,eq}$	Left beam end reaction that identifies the magnitude of an unbalanced force at which local effects dominate beam moment demands, kips
		V_1	Vertical component of the force in brace 1, kips
		V_2	Vertical component of the force in brace 2, kips
		V_{a-a}	Vertical (normal) force acting at the gusset-to-beam interface, kips
		V_{max}	Maximum required beam shear, kips
		$V_{u,max}$	Maximum required (design) shear strength, kips
		$V(x_1)$	Beam shear as a function of x_1 , kips
		$V(x_2)$	Beam shear as a function of x_2 , kips
		Z	Plastic section modulus, in. ³
		a	Distance from left beam support to location of work point, in.
		a'	Distance from left beam support to left edge of gusset, in.
		b	Distance from work point to right beam support, in.
		d	Depth of frame beam, in.
		e_b	Perpendicular distance from the gusset interface to the gravity axis of the frame beam, in.
		$e_{b,app}$	Approximation of length of half-depth of the frame beam, in.
		h	Vertical dimension of the gusset, in.

q	Net uniformly distributed moment, kip-in.
w_l	Net uniformly distributed transverse load on left half of gusset, kip/in.
w_r	Net uniformly distributed transverse load on right half of gusset, kip/in.
w.p.	Brace work point
Δ	Horizontal misalignment between the work point and the centroid of the gusset-to-beam interface, in.
ΔM_{local}	Change in beam moment from the left edge of the gusset to location of maximum moment when local effects are considered, kip-in.
ΔM_{unbal}	Change in beam moment from the left edge of the gusset to location of maximum moment when local effects are not considered, kip-in.
ΣV_i	Summation of vertical brace force components (unbalanced vertical force), kips

REFERENCES

- AISC (2016), *Seismic Provisions for Structural Steel Buildings*, ANSI/AISC 341-16, American Institute of Steel Construction, Chicago, IL.
- AISC (2017), *Steel Construction Manual*, 15th Ed., American Institute of Steel Construction, Chicago, IL.
- Fortney, P.J. and Thornton, W.A. (2015), "The CHEVRON EFFECT—Not an Isolated Problem," *Engineering Journal*, AISC, Vol. 52, No. 2, pp. 125–163.

Strongback Steel-Braced Frames for Improved Seismic Behavior in Buildings

JUDY LIU

INTRODUCTION

Ongoing work on the strongback braced frame is highlighted. The research is led by Dr. Stephen Mahin, professor at the University of California–Berkeley, and Byron L. and Elvira E. Nishkian, professors of structural engineering. Dr. Mahin currently leads the SimCenter as part of the Natural Hazards Engineering Research Infrastructure (NHERI) and was recently awarded an AISC grant to research and develop a possible design method for the strongback system.

There have been a number of investigations and examples of implementation of the strongback system in recent years. Dr. Jiun-Wei Lai, an engineer at Degenkolb Engineers in California, compared the behavior of strongback systems with conventional braced-frame systems through monotonic, cyclic, and nonlinear dynamic time-history analyses as a doctoral student at the University of California–Berkeley (Lai and Mahin, 2015). Barbara Simpson, a doctoral candidate at U.C. Berkeley, conducted the first experimental test of a strongback system (Simpson and Mahin, 2016) and is currently focused on developing the strongback system. In tandem, a strongback buckling restrained braced frame (BRBF) was constructed by Tipping Structural Engineers in Berkeley, California, and tested under quasi-static cyclic loading at U.C. Berkeley (Panian et al., 2015). Modified versions of the strongback have also been employed by Gregory P. Luth & Associates for several buildings on the West Coast as well as throughout the Central United States over the past 6 years (Luth, 2017). Pollino et al. (2017) have more recently studied and conducted hybrid testing (Slovenec et al., 2017) on the Stiff Rocking Core (SRC), a rehabilitation scheme utilizing conventional buckling and yielding brace behavior. Related work on rocking and self-centering braced frames has been conducted by Eatherton et al. (2014), Sause et al. (2014), and others.

Similar resisting systems have been studied internationally. In Canada, a dual system utilizing a pinned-base

vertical elastic truss has been investigated by Tremblay et al. (1997) to mitigate soft-story response in tension-only braced frames and, later, buckling restrained brace (BRB) frames (Tremblay, 2003; Tremblay and Merzouq, 2004; Tremblay and Poncet, 2004; Merzouq and Tremblay, 2006). In the 1990s, Japanese researchers also studied spine systems with elastic trussed stems coupled with BRBFs to mitigate damage concentration, and the concept was applied in a 24-story building in Tokyo (Aoki et al., 1998; Taga et al., 2004). The contribution of a vertical elastic spine has similitudes with the role played by an ancient Japanese pagoda's central column (shinbashira) in controlling floor sways to prevent seismic collapse (Nakahara et al., 2000). In Japan, researchers have also proposed an elastic truss system with BRB fuses (Takeuchi and Suzuki, 2003; Takeuchi et al., 2015), a concept also studied by Tremblay et al. (2004) and Wu and Lu (2015) in China. Retrofit of seismically deficient structures with stiff rocking walls was initially proposed and implemented in Japan (Wada et al., 2009; Qu et al., 2012). A continuous column concept with gravity columns distributing demands from weak or soft stories at adjacent stories was studied in Canada (Tremblay and Stiemer, 1994; Tremblay, 2000), New Zealand (MacRae et al., 2004; MacRae, 2011), and Japan (Ji et al., 2009). In Canada, minimum column continuity requirements have been implemented for seismic design of multistory steel-braced frames (CSA, 2001). For eccentrically braced steel frames (EBFs), Martini et al. (1990) proposed to vertically tie the links to achieve more inelastic demand in links. The resulting tied-EBF consisted of two elastic trussed masts pinned at their bases and interconnected by a series of ductile links. The structural system was further examined by researchers from Italy (Ghersi et al., 2000, 2003; Rossi, 2007). Researchers in Canada proposed to divide the tied-EBF masts in pin-connected modules to reduce the force demands on the truss members while preserving the beneficial drift concentration mitigating effect (Chen et al., 2012; Tremblay et al., 2014).

STRONGBACK CONCEPT

While current AISC provisions have greatly improved the seismic behavior of conventional braced frame systems, they still have a tendency to form weak stories (e.g., Uriz

Judy Liu, Ph.D., Research Editor of the AISC *Engineering Journal*, Professor, Oregon State University, School of Civil and Construction Engineering, Corvallis, OR. Email: judy.liu@oregonstate.edu

and Mahin, 2008; Khatib et al., 1988; Tremblay and Poncet, 2004) (Figure 1a). The strongback system was developed as a method of delaying or preventing weak-story behavior. Conceptually, the inclusion of an “essentially elastic” backbone, or strongback, enforces a nearly uniform drift distribution, thereby engaging adjacent stories upon the initiation of inelastic behavior in the opposite braces (Figure 1b). In this sense, the bay of a conventional braced frame is designed to be asymmetric with both an inelastic, energy dissipation portion and an essentially elastic, distributed deformation demand portion.

A variety of different strongback or elastic truss configurations can be utilized. Options based on Simpson and Mahin (in press), Slovenec et al. (2017), and Merzouq and Tremblay (2006) are shown in Figure 2. The elastic portion of the frame could be a truss or, alternatively, a concrete or steel plate shear wall. The elastic portion is often pinned at its base and is not intended to increase lateral strength but, instead, to supply a means of transferring demands vertically between stories. Vertical ties or connecting elements are required to transfer forces. The inelastic portion of the frame could be buckling restrained braces (BRBs) or conventional yielding and buckling brace members.

The strongback provides an economical means of engaging both the strength and energy absorption capacity of an entire system and averaging damage over the height of the building. Peak inelastic demands and damage are reduced. Further, the ability of the strongback to bridge across and distribute forces over multiple stories allows for removal of

braces at some stories, as shown in Figure 2a. As noted by Panian et al. (2015), the backbone may require extra strength to remain elastic, but cost savings can be found in use of “ordinary details in the elastic truss, the utilization of the same brace cross section and connection details at every story, and a reduction of the strength or number of braced frames if a reduced redundancy factor could be justified” (Simpson and Mahin, 2016).

RESEARCH AND PRACTICE

The strongback has been utilized in both research and practice. Previous numerical investigations of strongback behavior have focused on nonlinear time-history analyses. A strongback retrofit was also tested experimentally as an extension of research on older concentrically braced frames. This preliminary work has shown that the strongback method could be a viable method of resisting a weak-story response. The design and construction of several buildings with strongback frames has shown that this system also has the potential of being integrated into current design practice.

Past Numerical Studies

Numerical investigations into strongback and similar systems include work by Lai and Mahin (2015) and Merzouq and Tremblay (2006). Both studies compared conventional systems and strongback or elastic truss systems.

Merzouq and Tremblay (2006) compared the performance of five prototype office buildings ranging from 8 to 24 stories and located in Victoria, British Columbia. Three different configurations were studied for each prototype building: chevron bracing with BRB members, chevron bracing with BRBs and elastic trusses split between two exterior bays, and a two-story X-bracing configuration with a central elastic truss (Figure 2c). Nonlinear, dynamic time-history analyses were conducted for two suites of ground-motion records. One suite included four simulated and six historical ground-motion time histories typical of the Victoria region at magnitude 6.5 and magnitude 7.2. The second suite was comprised of four ground-motion time histories simulated for magnitude 8.5 rupture scenarios along the Cascadia subduction fault plane. “The ground motion amplitude was adjusted to match, on average, the 2% in 50 year probability of exceedance spectrum over the applicable period range” (Merzouq and Tremblay, 2006).

The analysis results highlighted the potential of the elastic truss, or “dual BRB,” system and the shortcomings of the conventional chevron configuration with BRBs. Despite the stable hysteretic response of the BRBs, failure of the conventional BRB frames occurred for some of the Victoria ground motions and for all of the Cascadia ground motions. “These structures experienced large story drifts and several occurrences of dynamic instability were observed, indicating that

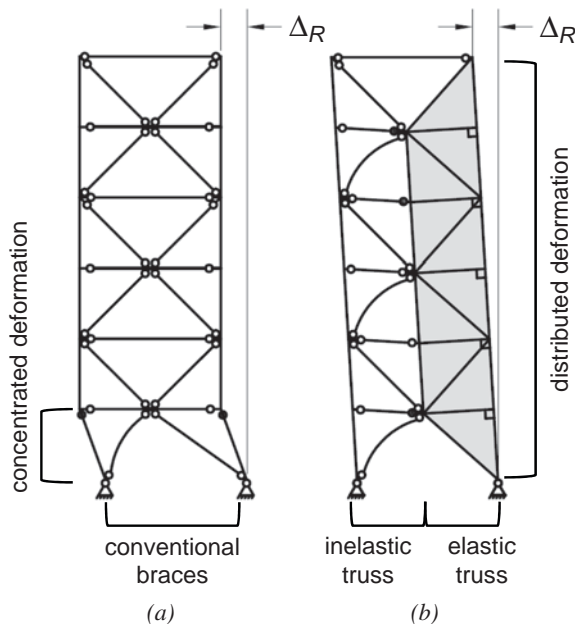


Fig. 1. Comparison of (a) conventional and (b) strongback braced frames (courtesy of Barbara Simpson).

the frames did not possess sufficient capacity to redistribute the inelastic demand over their height” (Merzouq and Tremblay, 2006). By contrast, collapse of the dual BRB system occurred only for the 12-story prototype for one of Cascadia ground motions. “However, even in that case, all members of the elastic truss remained elastic, as was also the case under all other ground motions, confirming the adequacy of the proposed empirical design rules” (Merzouq and Tremblay, 2006). The empirical design rules included first designing the BRBs for the code-specified forces, conducting capacity design for all other members, and determining forces in the elastic truss according to stiffness of the elastic truss and

expected variation between floors for the expected BRB plastic deformations. Further investigation of the empirical design approach is needed to confirm efficacy with respect to performance objectives, other building heights, and other frame geometries.

Lai and Mahin (2015) investigated six different configurations, including a typical chevron brace configuration, a typical two-story X-bracing configuration (model X6; Figure 3a), and an offset two-story X-bracing configuration with the intersection of the braces at a third point of the beam (model X6-3; Figure 3b). They also studied an offset two-story X-bracing configuration with conventional braces

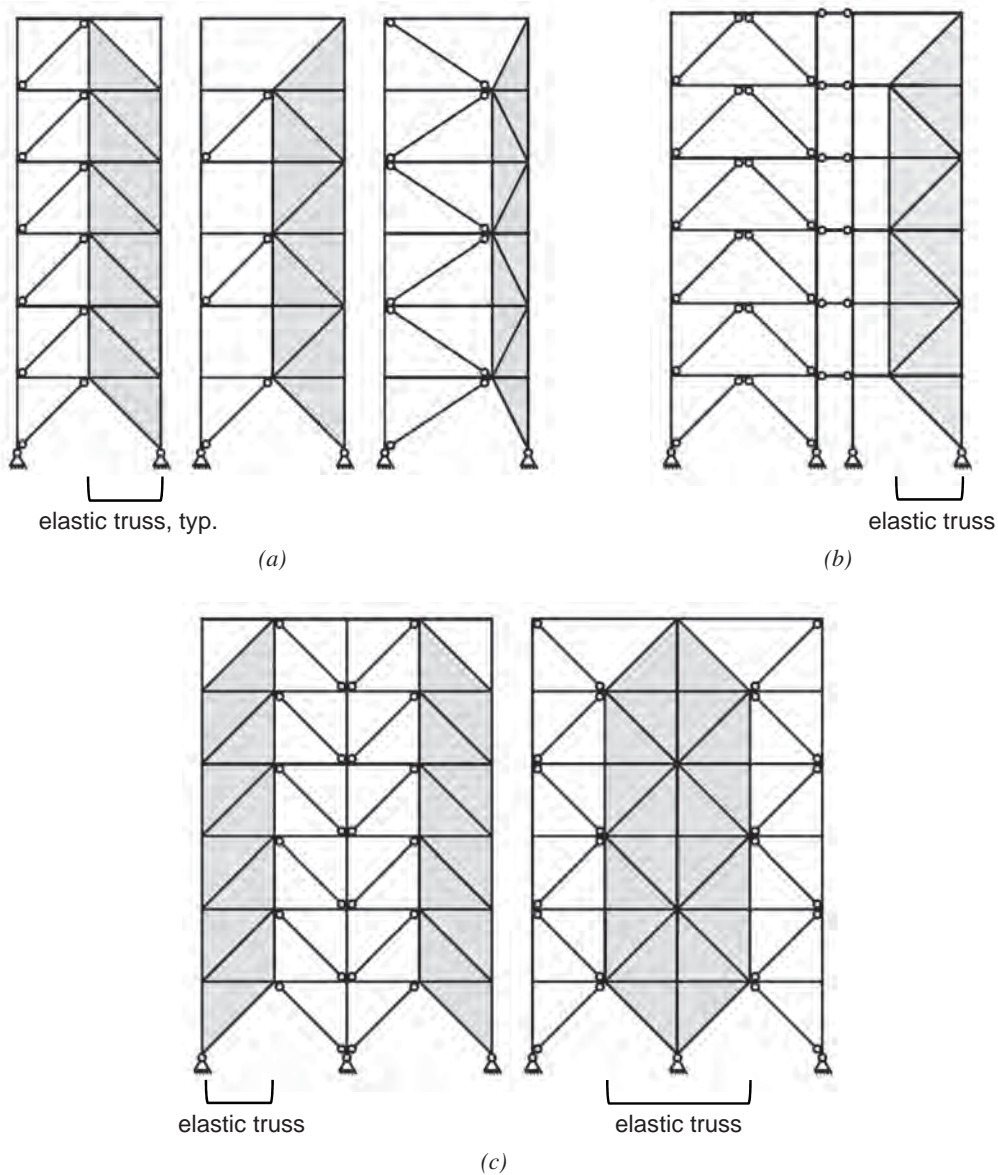


Fig. 2. Possible strongback or elastic truss system configurations based on (a) Simpson and Mahin (in press), (b) Slovenec et al. (2017), and (c) Merzouq and Tremblay (2006) (courtesy of Barbara Simpson).

and vertical strongback “spines” (model SB6-3; Figure 3c). Additional variations included the use of BRB braces with standard and low-yield steel in the cores. A pair of braced bays was located on each side of the five-by-five bay, six-story office prototype building.

Highlighted here are models X6, X6-3 and SB6-3 (Figure 3). Lai and Mahin (2015) utilized an overstrength factor approach for design of the strongback spines, conducted nonlinear time histories on the prototype buildings, and compared the performance of the conventional and strongback braced frames. Model X6 exhibited somewhat fewer concentrated deformations compared to the chevron frame, with higher story drift ratios observed in two-story panel mechanisms. The concentration of deformation was reduced further with model X6-3. However, it was model SB6-3 that successfully prevented localized concentration of story deformation. The behavior of model X6-3 was as expected; most of the strongback spine braces remained elastic, and braces outside of the spines buckled. Lai and Mahin (2015) noted that the “design optimization of this simple strategy should be studied further”; the use of the overstrength factor did not fully account for physical behavior, force redistributions, and resulting demands on the strongback spines.

Large-Scale Experimental Study

Building upon the computational studies to date, a large-scale experimental investigation explored the viability of the strongback system under cyclic loading and its ability to mitigate weak-story behavior (Simpson and Mahin, 2016; Simpson et al., in press). The two-story, one-bay specimen was a nearly full-scale frame and included a BRB and a strongback with conventional HSS braces (Figure 4). This specimen represented a possible retrofit scheme for a conventional chevron braced frame, two of which were also tested in the experimental program. The original chevron braced frame (NCBF-B-1) was designed to older code standards, did not satisfy current seismic provisions, and formed a weak story after severe brace local buckling and fracture. A second chevron braced frame (NCBF-B-2) had braces filled with low-strength concrete to delay local buckling, but

it also experienced brace local buckling and fracture, yielding in the first story beam, and a weak story. For the retrofit, new braces and gusset plates were oriented in a strongback configuration (NCBF-B-3SB). The original beam and column sizes were kept the same as the older braced frame tests. The column, HSS braces, and right half of the beam formed the elastic strongback. The BRB on the left side of the frame was intended as the primary energy-dissipating element, and the strongback brace members were sized based on the maximum forces that the BRB could deliver to the rest of the frame. Plastic hinging was expected at both column bases; the right (strongback) column base was oriented for bending about the weak axis to better simulate a “pinned” base. Inelastic behavior was also expected in the left half of the first-story beam, acting as a sort of shear link; the web of the original beam was reinforced with doubler plates at the gusset plate connection. No inelastic brace was required in the second story because the strongback was able to engage the entire system.

The test specimen was subjected to quasi-static loading, following a testing protocol similar to cyclic qualification procedures for BRBs (AISC, 2016). Displacement was applied at the roof beam; a force equal to half of the load at the roof was applied at the first-story beam. The strongback successfully mitigated weak-story formation and was able to maintain nearly uniform drift over both stories for the entire loading history. The uniform drift for NCBF-B-3SB is demonstrated in Figure 5. In this figure, the ratio of first-story drift (Δ_1) to total drift ($\Delta_1 + \Delta_2$) remains at approximately 50% for the duration of the test. This is contrast to specimens NCBF-B-1 and NCBF-B-2, which deviate from 50% with the onset of local buckling (LB) of the braces, indicating weak-story formation.

The strongback specimen did experience a reduction in strength and stiffness after local buckling of the BRB casing in a cycle to a roof drift of 2.5%, but it continued to exhibit stable hysteresis loops (Figure 6) and to resist forces in compression after rupture (noted as F_r in Figure 5). The BRB did satisfy current cyclic testing requirements for BRBs (AISC, 2016) prior to rupture. As expected, plastic hinges did form

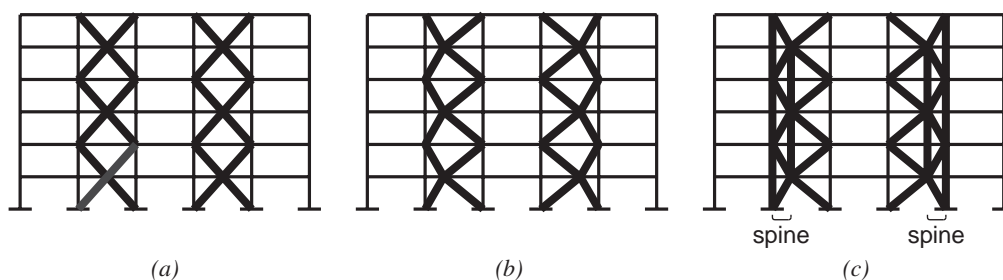
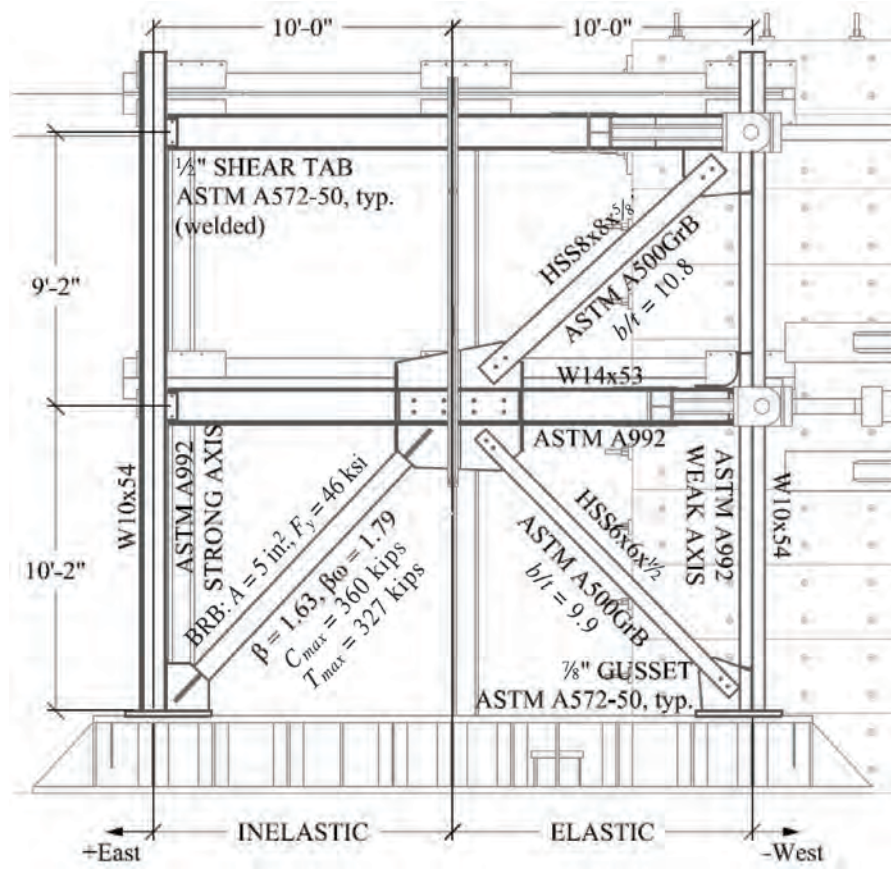


Fig. 3. (a) Conventional two-story X-bracing frame, (b) offset two-story X-bracing frame, and (c) offset two-story X-bracing with vertical strongback spines (based on Lai and Mahin, 2015).



(a)



(b)

Fig. 4. (a) Schematic and (b) photo of strongback test specimen (courtesy of Barbara Simpson).

at the column bases and in the first-story beam to the left of the gusset plate. Residual drift was similar in both stories. The inelastic demands were significant in some cases; current research is investigating an offset bracing scheme designed to decrease these inelastic demands while limiting the demands developed in the strongback. The strongback braces, meanwhile, remained essentially elastic. Figure 6 shows predictable behavior through comparisons of numerical simulations and NCBF-B-3SB experimental results for base shear versus roof drift ratio and BRB axial force versus deformation. In the numerical model, the braces were able to buckle out of plane, and the BRB element included a low-cycle fatigue material model (Uriz and Mahin, 2008).

Implementation in Practice

Strongback frames have been used for the seismic-force-resisting systems in a number of buildings in recent years. Different versions of the strongback have been explored, including a buckling restrained braced mast (BRBM) frame, a rocking frame, and a pivoting frame.

Tipping Structural Engineers designed a buckling restrained braced mast (BRBM) frame for the four-story Heinz Avenue Building in Berkeley, California (Panian et al., 2015). The BRBM for this laboratory building utilized wide-flange shapes in a vertical truss, or mast, and BRBs for the yielding elements (Figure 7). The same BRB size could

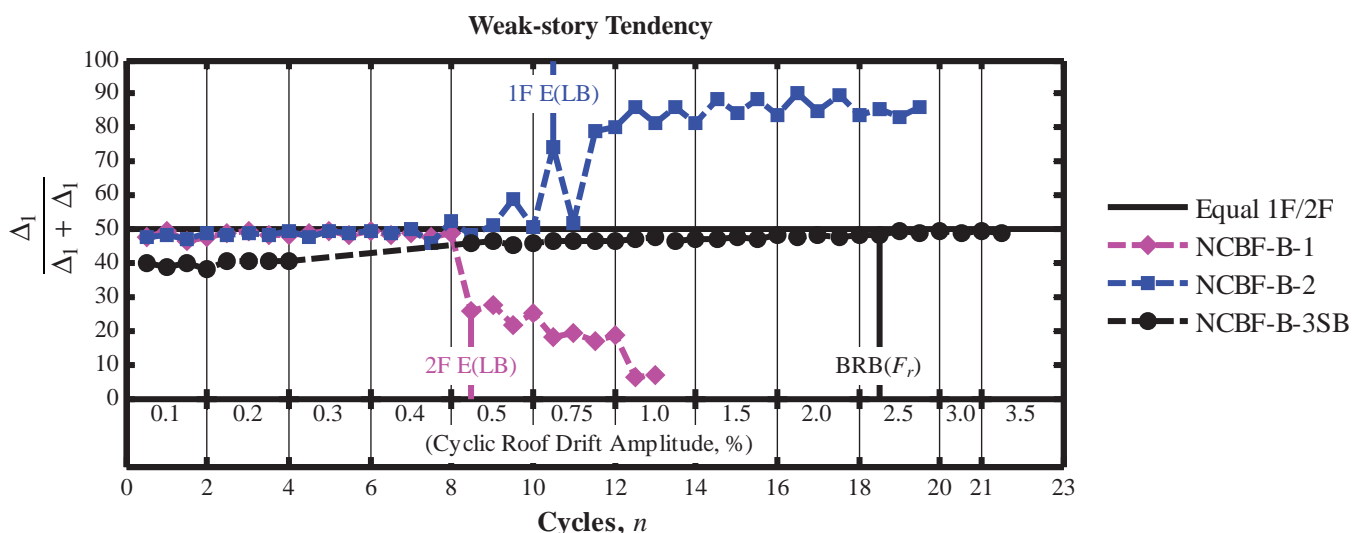


Fig. 5. Weak-story tendencies in braced frame tests (courtesy of Barbara Simpson).

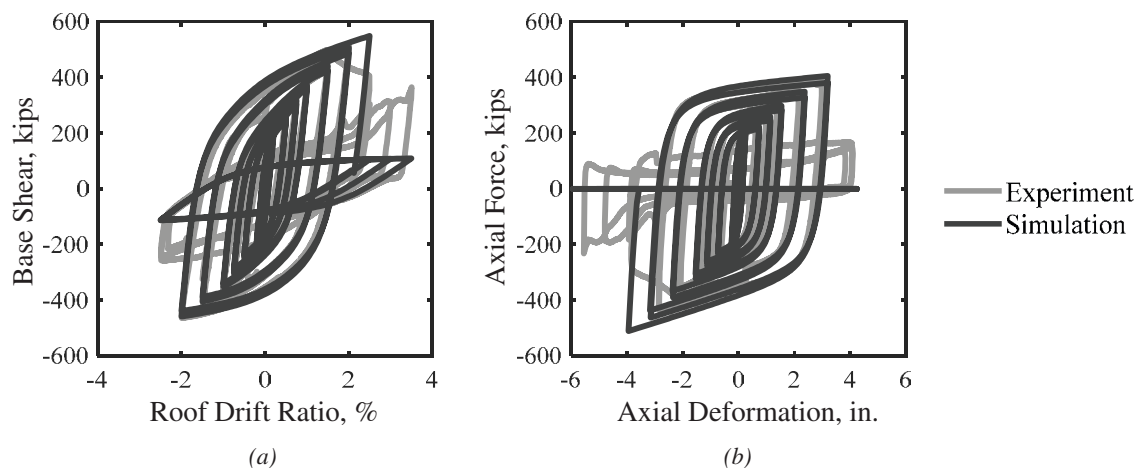
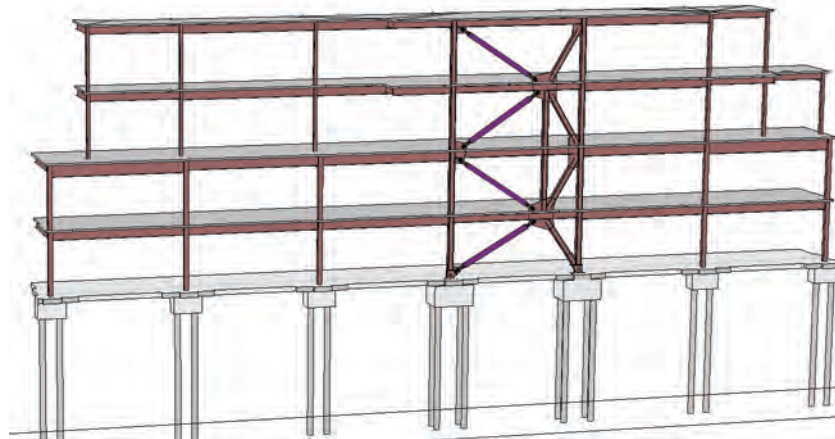


Fig. 6. Comparisons of experimental versus numerical simulation results for strongback frame: (a) base shear versus roof drift ratio; (b) BRB axial force versus deformation (courtesy of Barbara Simpson).



(a)



(b)

Fig. 7. (a) Elevation drawing and (b) photograph of BRBM frame in the Heinz Avenue building under construction (images courtesy of Tipping Structural Engineers).

be used at all stories because of the mast's ability to engage all stories to resist any additional-story shear, thus preventing a soft-story mechanism. Pinned column bases were used to reduce local bending and foundation loads. The BRBM utilized an offset geometry, as shown by Lai and Mahin (2015), to help to reduce inelastic demands.

The mast in the BRBM was designed to remain elastic for the design basis earthquake. Nonlinear time-history analysis, capacity design principles, and an overstrength factor of 2.0 were used. The overstrength factor was validated against forces obtained through a redundancy analysis; removal of a brace at any level did not result in more than a 33% reduction in story shear capacity or extreme torsional irregularity. The redundant BRBM used less than a third of the BRBs and approximately half of the number of frames as a conventional BRB frame.

Gregory P. Luth & Associates designed a number of modified rocking frames with essentially elastic strongbacks over the past 6 years. Their frames utilize either a "rocking" system, with columns lifting up in a rocking motion, or a "pivoting" frame that rotates around a pin at its base. Says Luth, "the latter may result in less non-structural damage as it does not involve differential movement at the floors." In 2011, post-tensioned shop-fabricated frames created a self-centering rocking frame system for a casino in Cape Girardeau, Missouri, at a site with ground motions comparable to those of San Francisco. "Krawinkler fuses" (Figure 8c) provided connections between the rocking frames and 10-ft-deep shop-fabricated trusses to dissipate energy. In 2014, a pivoting frame with a buckling restrained column (BRC) on one side and true pin on the other side was used in a casino in Jamul, California. After yielding of the BRC, "additional overturning resistance is provided by a full-story vierendeel frame at the top floor with Krawinkler fuses as the shear connection at the center of the vertical members of the vierendeel" (Luth, 2017).

In 2016, the Tesla Gigafactory in Reno, Nevada, presented a challenge with a fast-paced design for "potential equipment loads of up to 250 psf and 350 psf on the 2nd and 3rd floors respectively although actual loading was not defined until after steel fabrication had started (i.e. vertical mass distribution was undefined at the structural design phase)" (Luth, 2017). To economically accommodate significant variations in vertical mass distribution, Luth, working with nonlinear time histories and pushover analyses by Exponent, developed a pivoting strongback system. A pair of pinned-base, shop-fabricated frames flanking and connected to gravity columns with Krawinkler fuses (Figure 8) provide approximately 20% of the seismic resistance; the rest is provided by buckling restrained braces. Luth notes that the BRBs and the Krawinkler fuses "are forced to yield more or less uniformly by the strongback which remains elastic. Because of the redistribution function of the strongbacks, we are able to

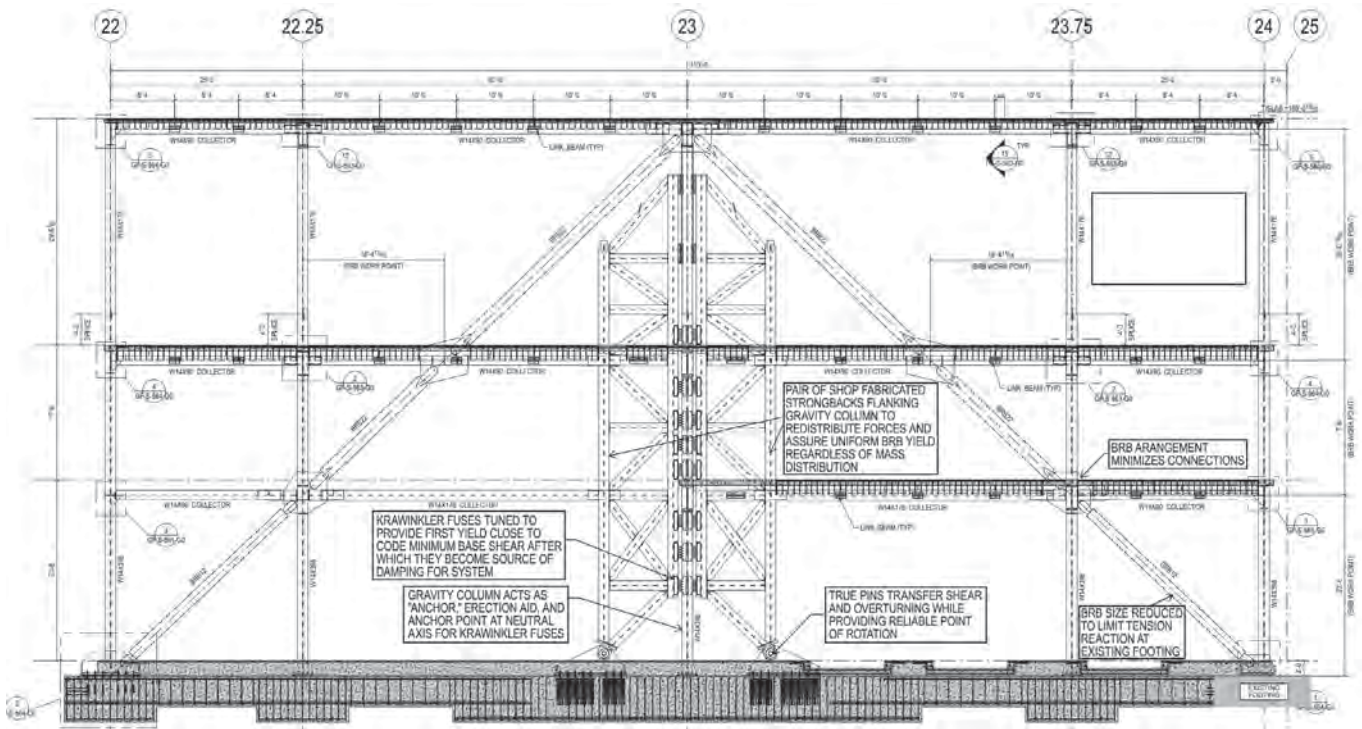
'tune' the brace areas for things other than strength. We can distribute the overturning moment across multiple columns by manipulating the brace area. The braces are effective no matter where you put them as long as you provide collectors to transfer the required forces. Conceptually, you could [place] all the braces at the top floor, the middle floor, or the bottom floor and there would be a complete load path. Of course the demands on the strongback change dramatically with these three basic arrangements. We found that the most efficient strategy was to use heavier BRB's in the middle story rather than the top or bottom. The most efficient arrangement ended up being a single full height chevron which creates a 'guyed' strongback arrangement" (Luth, 2017).

BEHAVIOR AND DESIGN OF STRONGBACK SYSTEMS

While there has been a variety of work on the strongback system in both research and practice, these analyses and design methods have depended largely on the use of iterative, nonlinear time-history analyses. These investigations have not indicated that a simple and reasonable design methodology exists that can robustly be extended to any generalized building system. Thus, research has focused on the development of a design methodology that can be simply and easily applied in practice. The current objectives of this research include:

1. Clarify which parameters influence the behavior of the strongback.
2. Develop a simple and coherent design methodology for the strongback system.
3. Validate the effectiveness of potential design, proportioning and detailing guidelines.
4. Present refined design methods to address enhanced performance objectives.

Requirements for the relative strength of the essentially elastic strongback to the strength of the inelastic bracing elements and the use of a redundancy factor is currently being studied. Parametric studies will be used to determine effects of various story heights and number of stories. Future work also includes investigation of alternative bracing configurations, types of inelastic braces (e.g., buckling restrained braces versus conventional brace members with buckling and yielding), and the effects of vertical or mass irregularities. Detailing of critical regions, such as the column base and of the strongback to inelastic frame connections, is also warranted. Finally, a cost-benefit analysis and performance evaluation is necessary to quantify the strongback's repair time and repair cost compared to conventional bracing



(a)



(b)



(c)

Fig. 8. (a) Elevation drawing and (b) photograph of strongback frame for the Tesla facility; (c) Krawinkler fuses (images courtesy of Gregory P. Luth & Associates).

systems. Validation through future experimental testing utilizing a strongback would confirm the effectiveness of the developed design method.

SUMMARY

The viability of the strongback braced frame has been demonstrated through computational parametric studies and experimental investigations. The strongback frame is able to engage multiple stories and eliminate weak-story behavior, resulting in improved seismic performance. Variations—from a buckling restrained braced mast (BRBM) to a pivoting, guyed strongback frame—have been implemented in buildings in high seismic regions, typically at a cost savings compared to conventional BRB frames. To date, each study or implementation has utilized its own combination of nonlinear time-history analyses and capacity design principles. Ongoing research is focused on developing a simple and coherent design methodology for the strongback braced frames.

ACKNOWLEDGMENTS

Special thanks to Barbara Simpson (U.C. Berkeley) for her many contributions to this article. Her research is supported by the American Institute of Steel Construction (AISC). Additional thanks go to Greg Luth (Gregory P. Luth & Associates Inc.), John Osteraas (Exponent), Leo Panian (Tipping Structural Engineers), and Dr. Robert Tremblay (École Polytechnique de Montréal) for images and suggestions for this article.

REFERENCES

AISC (2016), “Seismic Provisions for Structural Steel Buildings,” ANSI/AISC-341-16, American Institute of Steel Construction, Chicago, IL.

Aoki, K., Fukuyama, K., Okumoto, H., Ukai, K. and Taga, K. (1998), “Design of a High-Rise Building Using Unbonded Braces with Varying Cross Section,” *Journal of Construction Steel*, Vol. 6, pp. 139–144 (in Japanese).

Chen, L., Tremblay, R. and Tirca, L. (2012), “Seismic Performance of Modular Braced Frames for Multi-Storey Building Application,” 15th World Conference on Earthquake Engineering, Lisbon, Portugal, Paper No. 5458.

CSA (2001), “CSA/CAN-S16-01, Limit States Design of Steel Structures,” Canadian Standards Association, Toronto, ON.

Eatherton, M., Ma, X., Krawinkler, H., Mar, D., Billington, S., Hajjar, J. and Deierlein, G. (2014), “Design Concepts for Controlled Rocking of Self-Centering Steel-Braced Frames,” *Journal of Structural Engineering*, ASCE, Vol. 140, No. 11.

Ghersi, A., Neri, F., Rossi, P.P. and Perretti, A. (2000), “Seismic Response of Tied and Trussed Eccentrically Braced Frames,” *Proceedings of the STESSA 2000 Conference*, Montreal, Canada, pp. 495–502.

Ghersi, A., Pantano, S. and Rossi, P.P. (2003), “On the Design of Tied Braced Frames,” *Proceedings of the STESSA 2003 Conference*, pp. 413–429.

Ji, X., Kato, M., Wang, T., Hitaka, T. and Nakashima, M. (2009), “Effect of Gravity Columns on Mitigation of Drift Concentration for Braced Frames,” *Journal of Construction Steel Research*, Vol. 65, No. 12, pp. 2148–2156.

Khatib, I.F., Mahin, S.A. and Pister, K.S. (1988), “Seismic Behavior of Concentrically Braced Frames,” Report UCB/EERC-88/01, Earthquake Engineering Research Center, University of California, Berkeley, CA.

Lai, J. and Mahin, S.A. (2015), “Strongback System: A Way to Reduce Damage Concentration in Steel-Braced Frames,” *Journal of Structural Engineering*, ASCE, Vol. 141, No. 9.

Luth, G. (2017, June 13), Email with J. Liu.

MacRae, G.A. (2011), “The Continuous Column Concept—Development and Use,” *Proceedings of the 9th Pacific Conference on Earthquake Engineering*, Auckland, New Zealand, Paper No. 83.

MacRae, G., Kimura, Y. and Roeder, C. (2004), “Effect of Column Stiffness on Braced Frame Seismic Behavior,” *Journal of Structural Engineering*, ASCE, Vol. 130, No. 3, pp. 381–391.

Martini, K., Amin, N., Lee, P.L. and Bonowitz, D. (1990), “The Potential Role of Non-Linear Analysis in the Seismic Design of Building Structures,” *Proceedings of the 4th U.S. National Conference on Earthquake Engineering*, pp. 67–76.

Merzouq, S. and Tremblay, R. (2006), “Seismic Design of Dual Concentrically Braced Steel Frames for Stable Seismic Performance for Multi-Story Buildings,” *Proceedings of the 8th U.S. National Conference on Earthquake Engineering*, San Francisco, CA.

Nakahara, K., Hisatoku, T., Nagase, T. and Takahashi, Y. (2000), “Earthquake Response of Ancient Five-Story Pagoda Structure of Horyu-Ji Temple in Japan,” *Proceedings of the 2000 WCEE*, Paper No. 1,229.

Panian, L., Bucci, N. and Janhunen, B. (2015), “BRBM Frames: An Improved Approach to Seismic-Resistant Design Using Buckling-Restrained Braces,” *Second ATC & SEI Conference on Improving the Seismic Performance of Existing Buildings and Other Structures*, December 10-12, ASCE, San Francisco, CA, pp. 632–643.

- Pollino, M., Slovenec, D., Qu, B. and Mosqueda, G. (2017), "Seismic Rehabilitation of Concentrically Braced Frames Using Stiff Rocking Cores," *Journal of Structural Engineering*, ASCE, Vol. 14, No. 9.
- Rossi, P.P. (2007), "A Design Procedure for Tied Braced Frames," *Earthquake Engineering and Structural Dynamics*, Vol. 36, pp. 2,227–2,248.
- Qu, Z., Wada, A., Motoyui, S., Sakata, H. and Kishiki, S. (2012), "Pin-Supported Walls for Enhancing the Seismic Performance of Building Structures," *Earthquake Engineering and Structural Dynamics*, Vol. 41, No. 14, pp. 2,075–2,091.
- Sause, R., Ricles, J.M., Chancellor, N.B. and Roke, D.A. (2014), "Hybrid Simulations of Self-Centering Concentrically-Braced Frames Subject to Extreme Ground Motions," *Proceedings of the 10th US National Conference on Earthquake Engineering*, July, Anchorage, AK, EERI.
- Simpson, B.G. and Mahin, S.A. (2016), "Reducing Concentrations of Inelastic Demand with a Strongback," 2016 EERI Graduate Student Paper Competition winner, 12 pages.
- Simpson, B. and Mahin, S. (in press), "Experimental and Numerical Study of a Strongback System to Mitigate Weak Story Behavior in Steel Braced Frames," *Journal of Structural Engineering*.
- Simpson, B.G., Mahin, S.A. and Lai, J.W. (in press), "Cyclic Testing of Older Steel Braced Frames." Report PEER-2017/XX, Pacific Earthquake Engineering Research Center, Berkeley, CA.
- Slovenec, D., Sarebanha, A., Pollino, M., Mosqueda, G. and Qu, B. (2017), "Hybrid Testing of the Stiff Rocking Core Seismic Rehabilitation Technique," *Journal of Structural Engineering*, ASCE, Vol. 143, No. 9.
- Taga, K., Kato, M., Tokuda, Y., Tsuruta, J. and Wada, A. (2004), "Hints on How to Design Passive Control Structure Whose Damper Efficiency Is Enhanced, and Practicality of This Structure," *Proceedings of the Passive Control Symposium*, Tokyo Institute of Technology, Yokohama, Japan, pp. 105–112.
- Takeuchi, T., Chen, X. and Matsui, R. (2015), "Seismic Performance of Controlled Spine Frames with Energy-Dissipating Members," *Journal of Constructional Steel Research*, Vol. 114, pp. 51–65.
- Takeuchi, T. and Suzuki, K. (2003), "Performance-Based Design for Truss-Frame Structures Using Energy Dissipating Devices," *Proceedings of the STESSA 2003 Conference*, Naples, Italy, pp. 55–61.
- Tremblay, R. (2000), "Influence of Brace Slenderness on the Seismic Response of Concentrically Braced Steel Frames," *Proceedings of the STESSA Conference*, Montreal, Canada, pp. 527–534.
- Tremblay, R. (2003), "Achieving a Stable Inelastic Seismic Response for Concentrically Braced Steel Frames," *Engineering Journal*, AISC, Vol. 40, No. 2, pp. 111–129.
- Tremblay, R., Ben Ftima, M. and Sabelli, R. (2004), "An Innovative Bracing Configuration for Improved Seismic Response," *Proceedings of Recent Advances and New Trends in Structural Design International Colloquium*, Timisoara, Romania, pp. 419–430.
- Tremblay, R., Chen, L. and Tirca, L. (2014), "Enhancing the Seismic Performance of Multi-Storey Buildings with a Modular Tied Braced Frame System with Added Energy Dissipating Devices," *International Journal of High-Rise Buildings*, Vol. 3, No. 1, pp. 21–33.
- Tremblay, R. and Merzouq, S. (2004), "Dual Buckling Restrained Braced Steel Frames for Enhanced Seismic Response," *Proceedings of the Passive Control Symposium*, Tokyo Institute of Technology, Yokohama, Japan, pp. 89–104.
- Tremblay, R. and Poncet, L. (2004), "Improving the Seismic Stability of Concentrically Braced Steel Frames," *Proceedings of the 2004 SSRC Annual Technical Session & Meeting*, Long Beach, CA, pp. 19–38.
- Tremblay, R., Robert, N. and Filiatrault, A. (1997), "Tension-Only Bracing: A Viable Earthquake-Resistant System for Low-Rise Steel Buildings?" *Proceedings of the SDSS '97 Fifth International Colloquium on Stability and Ductility of Steel Structures*, Nagoya, Japan, 2, pp. 1,163–1,170.
- Tremblay, R. and Stiemer, S.F. (1994), "Back-up Stiffness for Improving the Stability of Multi-Story Braced Frames under Seismic Loading," *Proceedings of the SSRC Annual Task Group Technical Session*, Bethlehem, PA, pp. 311–325.
- Uriz, P. and Mahin, S.A. (2008), "Toward Earthquake Resistant Design of Concentrically Braced Steel-Frame Structures," Report PEER-2008/08, Pacific Earthquake Engineering Research Center, University of California, Berkeley, CA.
- Wada, A., Qu, Z., Ito, H., Motoyui, S., Sakata, H. and Kasai, K. (2009), "Seismic Retrofit Using Rocking Walls and Steel Dampers," *ATC/SEI Conference on Improving the Seismic Performance of Existing Buildings and Other Structures*, ASCE, San Francisco, CA.
- Wu, D. and Lu, X.L. (2015), "Structural Performance Evaluation of a New Energy-Dissipation and Light-Weight Rocking Frame by Numerical Analysis and Experiment," *Proceedings of the 10th Pacific Conference on Earthquake Engineering*, Sydney, Australia, Paper No. 191.

Guide for Authors

- Scope** *Engineering Journal* is dedicated to the improvement and advancement of structural steel construction. Its pages are open to all who wish to report on new developments or techniques in structural steel design, research, construction, steel fabrication methods, or new products of significance to the use of structural steel in construction. Only original papers may be submitted. Determining the appropriateness of submissions for the review process is the purview of the editors.
- General** Papers intended for publication should be submitted by email Margaret Matthew, Editor, at matthew@aisc.org.
- The articles published in the *Engineering Journal* undergo peer review before publication for (1) originality of contribution; (2) technical value to the steel construction community; (3) proper credit to others working in the same area; (4) prior publication of the material; and (5) justification of the conclusion based on the report.
- All papers within the scope outlined above will be reviewed by engineers selected from among AISC staff, industry, design firms, and universities. The standard review process includes outside review by an average of three reviewers, who are experts in their respective technical area, and volunteers in the program. Papers not accepted will not be returned to the author. Published papers become the property of the American Institute of Steel Construction and are protected by appropriate copyrights. No proofs will be sent to authors. Each author receives three complimentary copies of the issue in which his contribution appears.
- Manuscripts** Manuscripts must be provided in Microsoft Word format. Include a PDF version of your submission so we may verify fonts, equations and figures. View our complete author guidelines at www.aisc.org/ej.



There's always a solution in steel.

Engineering Journal

American Institute of Steel Construction
130 E. Randolph Street, Suite 2000
Chicago, IL 60601

312.670.2400

www.aisc.org